

INFLUENCE OF APPLIED POTENTIAL, FLUID VELOCITY,
pH AND TEMPERATURE ON FORMATION OF CALCAREOUS DEPOSITS
UNDER IMPRESSED CURRENT CATHODIC PROTECTION

BY

RUPERT UTAK LEE

A DISSERTATION PRESENTED TO THE GRADUATE SCHOOL
OF THE UNIVERSITY OF FLORIDA IN
PARTIAL FULFILLMENT OF THE REQUIREMENTS
FOR THE DEGREE OF DOCTOR OF PHILOSOPHY

UNIVERSITY OF FLORIDA

1984

UNIVERSITY OF FLORIDA



3 1262 08552 3404

To God,
who has guided me
through my life

ACKNOWLEDGMENTS

I am grateful to

Dr. John R. Ambrose for his guidance through my graduate work as well as this research;

to Drs. Ellis D. Verink, Jr., Paul H. Holloway, E. Dow Whitney, and Gerhard M. Schmid for serving as members of my supervisory committee;

to Mr. Suribabu Jayanti for his suggestions and discussion;

and to Messrs. E.J. Jenkins and Guy P. La Torre and Dr. Michael A. Kosinski for their assistance in chemical analysis.

This work was supported by the National Program on Marine Corrosion Grant No. NA 81AA-D00011.

Special thanks are extended to my wife, Clara, and my parents for their support and encouragement.

TABLE OF CONTENTS

	Page
ACKNOWLEDGMENTS.....	iii
LIST OF TABLES.....	vi
LIST OF FIGURES.....	vii
ABSTRACT.....	ix
 CHAPTER	
1 INTRODUCTION.....	1
2 REVIEW OF LITERATURE.....	5
2.1 Mechanism of Deposit Formation.....	5
2.2 Properties of Calcareous Deposits.....	19
3 EXPERIMENTAL.....	36
3.1 Materials.....	36
3.2 Surface Preparation.....	38
3.3 Equipment.....	38
3.4 Current Measurements.....	39
3.5 Morphology and Chemical Analysis.....	41
4 RESULTS.....	42
5 DISCUSSION.....	66
5.1 Discussion of Background.....	66
5.1.1 Rotating Disc Electrode.....	66
5.1.2 Effects of Parameters.....	68
5.1.3 Ratio of Currents at Two Different Rotation Speeds.....	69
5.2 Discussion of Influence of Parameters on Deposit Formation.....	74
5.2.1 pH.....	74
5.2.2 Temperature.....	81
5.2.3 Potential.....	89
5.2.4 Fluid Velocity.....	99
5.2.5 Deposit Morphology.....	103
5.2.6 Chemical Analysis.....	105
5.2.7 Interaction Effects.....	111

5.3	Surface pH Model.....	113
6	CONCLUSIONS.....	124
7	RECOMMENDATIONS FOR FURTHER RESEARCH.....	126
APPENDIX		
1	CATHODIC PROTECTION.....	128
2	2 ⁴ FACTORIAL DESIGN.....	132
3	COMPOSITION OF IRON USED FOR ELECTRODES.....	137
BIBLIOGRAPHY.....		138
BIOGRAPHICAL SKETCH.....		144

LIST OF TABLES

Table	Page
1	Solubility product of various compounds in seawater.....7
2	Degree of supersaturation at various pH values.....12
3	Ionic composition of ASTM D-1141-75 artificial seawater.....13
4	Variation of solubility with temperature.....35
5	Parameters and their levels.....40
6	Current measurements under various conditions....43
7	Main and interaction effects.....44
8	Effective surface coverage.....46
9	Combination of different experimental conditions.....47
10	Relative viscosity of seawater.....85
11	Values of k.....108
12	Limiting equivalent ionic conductivities in aqueous solutions at 25°C and calculated diffusion coefficients.....120
13	Arrangement of 2 ⁴ factorial design experiment, duplicated.....134
14	Signs for calculating effects of 2 ⁴ factorial design.....136

LIST OF FIGURES

Figure		Page
1	Decrease in the Ratio of i_{1000}/i_{500} With Time....	48
2	Variation of Hydrogen Current ($i_{-1.0} - i_{-0.8}$) and Its Percentage With Time.....	51
3	Variation of $i_{-1.0} - i_{-0.8}$ With Time.....	52
4	SEM Micrograph of Deposit Formed at (0100); -0.8V, 1000 rpm, pH=8.3, 23°C.....	53
5	SEM Micrograph of Deposit Formed at (0000); -0.8V, 500 rpm, pH=8.3, 23°C.....	53
6	SEM Micrograph of Deposit Formed at (1000); -1.0V, 500 rpm, pH=8.3, 23°C.....	54
7	SEM Micrograph of Deposit Formed at (0001); -0.8V, 500 rpm, pH=8.3, 16°C.....	54
8	SEM Micrograph of Deposit Formed at (0010); -0.8V, 500 rpm, pH=7.9, 23°C.....	55
9	Electrode Surface After Deposit Was Removed With a Kimwipe Paper. Specimen Was Stored in a Desiccator for Five Days.....	55
10	Energy Dispersive X-ray Spectra of Globular Particle.....	57
11	Energy Dispersive X-ray Spectra of Globular Particles.....	58
12	Energy Dispersive X-ray Spectra of Background Layer.....	59
13	ESCA Survey Scan of Deposit Formed at (0000)....	60
14	ESCA Mg Scan of Deposit Formed at (0000).....	61
15	ESCA Fe Scan of Deposit Formed at (0000).....	62
16	ESCA Ca Scan (Low Resolution) of Deposit Formed at (0000).....	63

17	ESCA Ca Scan (Medium Resolution) of Deposit Formed at (0000).....	64
18	FTIR Spectra of Deposit Formed at (0000) for 2 (right scale) and 6 (left scale) hours.....	65
19	Three-Dimensional Flow of Liquid Near Rotating Disc Electrode.....	67
20	Cathodic Current vs. (Electrode Rotation Speed) ¹ / ₂	71
21	Cathodic Polarization Curves. The Top Curve Was Obtained After Deposit Was Formed for 4 ¹ / ₂ Hours and the Bottom Two Curves Were Obtained in Deposit-Free Solution. Electrode Rotation Speed Was 500 rpm.....	73
22	Schematic Presentation of the pH Effects.....	75
23	Cathodic Polarization Curve.....	78
24	Schematic Presentation of the T Effects.....	82
25	Schematic Presentation of the E Effects.....	90
26	Schematic Presentation of the RPM Effects.....	100
27	Schematic Layouts of Cathodic Protection System: Sacrificial Anode Method and Impressed Current Method.....	129
28	Diagram of Relative Energy Levels of Fe and Fe ⁺⁺ (or Fe ⁺⁺⁺) Before and After Cathodic Protection.....	130

Abstract of Dissertation Presented to the Graduate School
of the University of Florida in Partial Fulfillment of the
Requirements for the Degree of Doctor of Philosophy

INFLUENCE OF APPLIED POTENTIAL, FLUID VELOCITY,
pH, AND TEMPERATURE ON FORMATION OF CALCAREOUS DEPOSITS
UNDER IMPRESSED CURRENT CATHODIC PROTECTION

BY

RUPERT UTAK LEE

December, 1984

Chairman: Dr. John R. Ambrose

Major Department: Materials Science and Engineering

Formation of calcareous deposits is one of the characteristic features associated with cathodic protection in seawater environments. The deposits have two beneficial aspects in cathodic protection: they decrease cathodic current requirements and mitigate corrosion reactions.

The objective of this research was to characterize the effects of cathodic protection parameters on formation of calcareous deposits. Four parameters were selected: cathodic potential, fluid velocity, pH, and temperature. A factorial design technique was employed to investigate the influence of each parameter and also to assess the order of importance among the parameters. Within the experimental conditions studied, the largest influence on deposit formation was found to be associated with pH, with

temperature, potential, and flow velocity, decreasing in this order.

Morphological studies showed that the size of deposit particles increases with increase in deposition rate, which is a function of surface pH and degree of supersaturation. These findings could be explained by a heterogeneous nucleation and growth mechanism.

Chemical analysis did not show any trend in the variation of chemical composition with the variation of parameters.

Qualitatively, the influence of the four parameters could be explained in terms of surface pH and degree of supersaturation. For quantification of the influence, a surface pH model was proposed. It was found that the quantification cannot be fully completed until the kinetics of $\text{Mg}(\text{OH})_2$ formation is fully described.

CHAPTER 1 INTRODUCTION

Corrosion is the destructive attack on a metal by its electrochemical reactions with its environment. Recent technical innovations have enabled man to carry out more activities in seawater environments, thereby increasing the demand for performance from materials. Metals are particularly susceptible to high chloride concentration, high electrical conductivity, and biological activities of seawater.

One of the successful ways to cope with seawater corrosion is to apply cathodic protection (Appendix 1) by impressed current or by sacrificial anode methods. One of the characteristic features associated with cathodic protection in marine environments is formation of a white scale mainly comprised of calcium and magnesium compounds on metal surfaces. These deposits, called calcareous deposits, can not only reduce cathodic current requirements by physically forming a resistive barrier between metal and seawater but also mitigate corrosion reactions when cathodic protection current is removed by accident or for maintenance. Although these aspects of calcareous deposits have been well known for decades, little effort has been expended to take better advantage of the deposits. Consequently, the

formation of these deposits has not been introduced into the engineering of cathodic protection systems as a design parameter. In this respect, it is important to know the nature of deposit formation. This research has been directed toward providing practical information applicable to cathodic protection design, especially with respect to the following questions:

- What is the most important parameter in determining the rate of calcareous deposit formation?
- What is the relative degree of influence of parameters, e.g., temperature and flow velocity, on formation of deposits?
- What is the optimum condition for deposit formation? Can a better utilization of the protective nature of calcareous deposits be achieved when cathodic potential (or current density), practically speaking, the only controllable parameter, is properly adjusted?

Four parameters were selected: cathodic potential, solution flow velocity, pH, and temperature. Instead of circulating solution at different flow rates, the specimen electrode was rotated. In addition to the capability to simulate various flow velocities, the rotating electrode has the advantage of controlling mass transport. By means of a 2^4 factorial design method (Appendix 2), influence of the four parameters on cathodic current requirements and on formation of calcareous deposits were investigated. The same experiments were also performed in solutions which did not have deposit forming elements such as Ca^{++} , Mg^{++} and Sr^{++} in order to find influence of the four parameters on

rate of cathodic reactions, uninfluenced by occurrence of surface deposits.

Degree of coverage of the metal surface with deposit was studied from two different points of view. First, effective surface coverage which was defined as $(\text{cathodic current requirement without deposit} - \text{that with deposit formed on surface}) / (\text{cathodic current requirement without deposit})$ was studied. Because the numerator is the decrease in cathodic current caused by formation of deposit and the denominator is the cathodic current in the absence of deposit, the ratio multiplied by 100 is actually the percentage decrease in cathodic current contributed by calcareous deposit. Therefore, variation of effective surface coverage can be related to the influence of any parameter on formation of calcareous deposits. Secondly, electrode rotation speed was varied. At high rotation speed, i.e., at high flow velocity, reactants and products of cathodic reactions are supplied and removed at an increased rate, thus increasing cathodic current. Because the calcareous deposit functions as a barrier to the movement of these species, different types of deposit will have different barrier efficiencies, thus different cathodic currents. Two electrode rotation speeds were used, 500 and 1000 rpm. After a deposit was formed at one of the two rotation speeds, rotation speed was changed to the other. Current was measured before and after the rotation speed change. $(\text{Current at 1000 rpm}) / (\text{current at 500 rpm})$ was

plotted against time of cathodic polarization. This was repeated until the ratio dropped to an arbitrary value of 1.05 ± 0.1 at which the deposit assumes almost full control of mass transport. By comparing decay rate of the ratio at one set of conditions with that at the other, the influence of the four parameters on deposit formation rate could be studied.

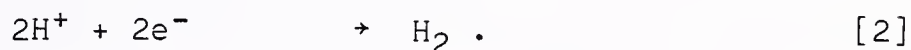
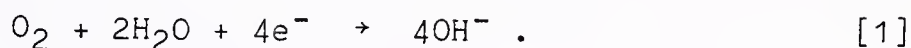
Chemical compositions of calcareous deposits were investigated with various techniques such as energy dispersive X-ray analysis, X-ray photoelectron spectroscopy and Fourier Transform infrared analysis.

The pH near cathodically protected metal surfaces has been proposed by several researchers. This surface pH is a very important parameter in controlling deposit formation rate. A mathematical model, including reactions affecting surface pH, was established.

CHAPTER 2 REVIEW OF LITERATURE

2.1 Mechanism of Deposit Formation

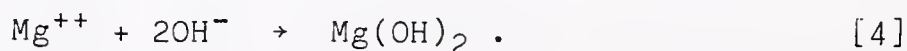
Cathodic protection systems supply negative charges to a metal to be protected from corrosion attack (See Appendix 1). At the negative potentials of cathodic protection, two cathodic reactions can take place on the metal surface in seawater environments.



Depending upon the potential, oxide film on the surface and other reducible species, if present, can also be reduced. The result of reaction [1] is exactly the same as that of reaction [2] in increasing OH^- concentration at the metal-solution interface area. Increase in OH^- concentration dissociates HCO_3^- .



As OH^- and CO_3^{--} concentrations increase beyond the solubility product limit of $\text{Mg}(\text{OH})_2$ and CaCO_3 , these two compounds precipitate on the metal surface.





The pH above which $\text{Mg}(\text{OH})_2$ is supersaturated can be calculated from

$$[\text{OH}^-]^2 = \frac{K_{s, \text{Mg}(\text{OH})_2}}{[\text{Mg}^{++}]}$$

where $K_{s, \text{Mg}(\text{OH})_2}$ = solubility product of $\text{Mg}(\text{OH})_2$.

From the solubility product of $\text{Mg}(\text{OH})_2$ in Table 1 (1-4) and from the Mg^{++} concentration in seawater of $5.46 \times 10^{-2} \text{M}$, the $[\text{OH}^-] = 2.1 \times 10^{-5} \text{M}$ or $\text{pH} = 9.3$ can be calculated above which $\text{Mg}(\text{OH})_2$ is supersaturated. Pytkowicz et al. (5) observed that $\text{Mg}(\text{OH})_2$ precipitation started in seawater between $\text{pH} = 9.8$ and 9.9 . If the precipitation process is aided by the presence of a metal surface in its nucleation and growth, it may require a lower degree of supersaturation, i.e., a lower surface pH than the above calculation for initiation.

A very high surface pH, greater than 11, under cathodic protection conditions in seawater has been suggested by several authors. On the assumption that OH^- is transported away from the metal surface by diffusion, Engell and Forchhammer (6) and Wolfson and Hartt (7) equated

$$\text{flux}_{\text{O}_2} = \frac{1}{4} \text{flux}_{\text{OH}^-}$$

and calculated such a high surface pH. The factor of $1/4$ is to account for the fact that one mole of O_2 generates four

Table 1 Solubility product of various compounds in seawater

<u>Compounds</u>	<u>log K_s</u>	<u>Temp (°C)</u>	<u>Reference</u>
CaCO ₃ (calcite)	-6.2	25	1
CaCO ₃ (aragonite)	-6.05	25	1
SrCO ₃	-4.46	25	Note
MgCO ₃	-3.52	0	2
MgCO ₃ ·H ₂ O	-3.15	-	2
Mg(OH) ₂	-10.16	25	3
CaSO ₄ ·2H ₂ O	-4.37	25	4

Note: Based upon reported solubility product (1), corrected for ionic strength at seawater (2).

moles of OH^- as in equation [1]. At a more negative cathodic potential, the hydrogen evolution reaction also takes place supplying more OH^- to the surface region, and surface pH could go even higher. When a $[\text{HCO}_3^-]$ of $2 \times 10^{-3} \text{M}$ in seawater is considered, such a high pH is unrealistic. The actual pH will be substantially lowered by the buffer capacity of HCO_3^- . The method to calculate surface pH used by Guillen and Feliu (8) is probably more accurate. Using the following mass balance equation for OH^-

$$N_f = N_d + N_p$$

where N_f = amount generated by cathodic reaction(s)

N_d = amount diffused away from surface

N_p = amount consumed by precipitation,

they suggested a surface pH of greater than 10 which varied with current density. From the weight and the chemical composition of deposit, the amounts of $\text{Mg}(\text{OH})_2$ and CaCO_3 were calculated. Subsequently, they calculated the amount of OH^- associated with $\text{Mg}(\text{OH})_2$ and necessary to produce the amount of CO_3^{--} associated with CaCO_3 . This procedure for surface pH estimation is valid only under the assumptions that all the precipitate particles are deposited on the cathode surface and that the precipitation of CaCO_3 does not need any supersaturation which is not true. However, as will be discussed later in this section, precipitation of CaCO_3 is retarded by the presence of other species in seawater. Therefore, all the generated CO_3^{--} are not coordinated with

Ca^{++} to form CaCO_3 and a certain amount of CO_3^{--} will be transported away from the surface. When this effect is taken into account, a lower surface pH will be calculated.

A brucite structure was found from the X-ray analyses of calcareous deposits (5,9,10) indicating that $\text{Mg}(\text{OH})_2$ in calcareous deposits is present in the crystalline form.

On the other hand, CaCO_3 is supersaturated in seawater. From $[\text{Ca}^{++}] = 1.04 \times 10^{-2} \text{M}$ and $[\text{CO}_3^{--}] = 1.4 \times 10^{-4} \text{M}$ at $\text{pH} = 8$, which are the $[\text{Ca}^{++}]$ and $[\text{CO}_3^{--}]$ concentrations of the solution used for this study and also represent the concentrations of the two species in seawater, the product of $[\text{Ca}^{++}] \cdot [\text{CO}_3^{--}] = 1.5 \times 10^{-5}$ can be obtained which is substantially greater than its solubility product of 6.3×10^{-7} (calcite). Once a solution is supersaturated with CaCO_3 , the rate of its deposition depends on the kinetics of the deposition reaction. There are several applicable experimental equations (11-15). However, those suggested rate equations can be generalized into

$$\begin{aligned} \text{rate} &= \frac{d[\text{CaCO}_3]}{dt} \\ &= L K_{s, \text{CaCO}_3} \left\{ \frac{[\text{Ca}^{++}]^a [\text{CO}_3^{--}]^a}{K_{s, \text{CaCO}_3}^a} - 1 \right\}^{1/a} \end{aligned}$$

where L = constant including rate constant, activity coefficient and/or surface area of seed crystals

K_{s, CaCO_3} = solubility product of CaCO_3

$[\text{Ca}^{++}]$ = concentration of Ca^{++}

$[\text{CO}_3^{--}]$ = concentration of CO_3^{--}

a = experimental constant.

From the equation, it can be concluded that the rate of CaCO_3 formation depends upon the degree of supersaturation, which is defined as

$$\frac{[\text{Ca}^{++}] \cdot [\text{CO}_3^{--}]}{K_s} .$$

Also, complex ion formation has to be considered. Studies (16-18) show that about 90% of CO_3^{--} are coordinated with Na^+ , Mg^{++} , and Ca^{++} . Therefore, the degree of supersaturation could be less than the above calculation indicates.

Also, as will be discussed later, the precipitation of CaCO_3 from naturally occurring supersaturated seawater does not occur in reasonable experimental periods (19-21) because of the effect of Mg^{++} and other species on its deposition kinetics.

At a cathodic potential less negative than the potential for the initiation of hydrogen evolution reaction, only reaction [1] takes place on a steel surface whereas at a potential more negative than that, both reactions [1] and [2] take place leading to a higher pH near the metal surface. From the pH consideration, it is conceivable that at a low surface pH (still higher than bulk pH), CaCO_3 is the predominant species of the deposits whereas at a high surface pH both CaCO_3 and $\text{Mg}(\text{OH})_2$ precipitate. Guillen and

Feliu (8) found that Ca-to-Mg ratio decreased with increase in surface pH. He calculated degree of supersaturation at various pHs for CaCO_3 and $\text{Mg}(\text{OH})_2$. As can be seen in Table 2, the degree of supersaturation of $\text{Mg}(\text{OH})_2$ increases far more rapidly than that of CaCO_3 . From the solubility data of Table 1 and concentration of ions in seawater as shown in Table 3 (22), it is very unlikely that other compounds would form as precipitate. However, MgCO_3 and SrCO_3 can form a solid solution with CaCO_3 due to the increase in activity coefficient of minor constituents in solid solution.

The incorporation of Mg^{++} in CaCO_3 can be explained from the study of the effect of Mg^{++} on CaCO_3 nucleation and growth. It has been known for decades that CaCO_3 formation is retarded in the presence of Mg^{++} . There are two hypotheses about the inhibitory effect of Mg^{++} . The first hypothesis is that Mg^{++} is a poison to CaCO_3 formation. Pytkowicz (19,23) suggested that Mg^{++} acts as a surface poison by being adsorbed as a hydrated ion, and its presence increases the nuclei size and the number of collisions between Ca^{++} and CO_3^{--} . Also, Mg^{++} adsorbed on active growth sites such as kinks inhibits the spread of monomolecular steps on the crystal surface. This hypothesis was also provided by Lippman (24) in a slightly different way. He suggested that Mg^{++} ions are adsorbed on active growth sites and congest the site due to their large sheath of hydration. Pytkowicz (19) studied the time of CaCO_3

Table 2 Degree of Supersaturation at various pH values

pH	$\frac{[\text{Ca}^{++}][\text{CO}_3^{--}]}{K_{s, \text{CaCO}_3}}$	$\frac{[\text{Mg}^{++}][\text{OH}^-]^2}{K_{s, \text{Mg(OH)}_2}}$
7.9	18.1	$2.17 \times 10^{-3.2}$
8.0	28.8	2.17×10^{-3}
8.3	53.7	$2.17 \times 10^{-2.4}$
8.5	79.0	2.17×10^{-2}
9.0	174	2.17×10^{-1}
9.5	281	2.17
10.0	349	2.17×10^1

Data used for these calculations:

$$\text{p}K_1 = 6.0, \text{p}K_2 = 9.1 \quad (2)$$

$$K_{s, \text{CaCO}_3} = 6.2 \quad (1)$$

$$K_{s, \text{Mg(OH)}_2} = 10.16 \quad (3)$$

$$[\text{Ca}^{++}] = 1.04 \times 10^{-2}, [\text{Mg}^{++}] = 5.46 \times 10^{-2}$$

Table 3 Ionic composition of ASTM D-1141-75 artificial seawater

<u>Ions</u>	<u>Concentration (mole/liter)</u>
Na ⁺	6.52x10 ⁻¹
Mg ⁺⁺	5.46x10 ⁻²
Ca ⁺⁺	1.04x10 ⁻²
K ⁺	1.02x10 ⁻²
Sr ⁺⁺	9.03x10 ⁻⁵
Cl ⁻	7.24x10 ⁻¹
SO ₄ ⁼	3.30x10 ⁻²
HCO ₃ ⁻	2.39x10 ⁻² *
Br ⁻	8.49x10 ⁻⁴
F ⁻	7.14x10 ⁻⁵
H ₃ BO ₃	4.37x10 ⁻⁴

Note: Chlorinity of this artifical seawater is 19.38 ‰ (22). Salinity is 35 ‰, calculated from salinity = 0.03+1.805 chlorinity.

* as added

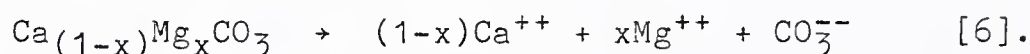
nucleation in natural seawater, Mg^{++} free artificial seawater and Mg^{++} enriched natural seawater after adding CO_3^{--} . The induction period for nucleation was determined by monitoring the time lapse before the increase in pH. From these observations, it was concluded that Mg^{++} , at its nominal seawater concentration, inhibits the formation of CaCO_3 and is the predominant factor in determining the time for the initiation of nucleation. Reddy and Wang (25) studied the growth rate of CaCO_3 on a seed CaCO_3 crystal in CaCO_3 supersaturated solutions with and without Mg^{++} . The rate of deposition was determined by monitoring the concentration of ions as a function of time. Mg^{++} , at 10^{-5}M , had almost no inhibitory effect on crystallization. In contrast 10^{-1}M nearly stopped CaCO_3 growth. However, the introduction of induction period was not observed in their seed crystal experiments, apparently due to the presence of the seed crystal. A Langmuir adsorption isotherm fitted their data well, confirming that an adsorption mechanism can explain the dependence of crystal growth rate on the adsorption of Mg^{++} on crystal growth sites. Similar observations as to the inhibitory effect of Mg^{++} on CaCO_3 nucleation and growth have been made by several authors (20,24,26).

The second hypothesis was conceived more recently. Berner (27) suggested that Mg^{++} may serve as a surface poison, but is also incorporated into the growing crystals to such an extent that the solubility of the

magnesium-containing calcite is markedly increased. This increase in solubility slows down the formation of CaCO_3 . As more studies have been carried out in natural environments, the second hypothesis is becoming the more acceptable mechanism to explain the effect of Mg^{++} on CaCO_3 deposition in seawater environments.

It has been known for decades that natural CaCO_3 sediments have some magnesium concentration. Goldsmith et al. (28) found from X-ray analysis that natural carbonate sediments contain up to 9% of MgCO_3 . From the study of natural carbonate skeletal materials of marine organisms containing up to 30% MgCO_3 , Chave et al. (29) reported that the order of solubility is calcite with large MgCO_3 , aragonite and low MgCO_3 calcite, decreasing in this order. In a study of the stability of magnesium containing calcite, i.e., magnesian calcite, Plummer and MacKenzie (30) monitored the variation of pH with magnesian calcite dissolution and, from the extrapolation of time to infinity, they found that 2 and 24 mole % of magnesian calcites are stable or at least metastable. Thorstenson and Plummer (31) emphasized the thermodynamic stability of magnesian calcite system. Based upon the thermodynamic data provided by Plummer and MacKenzie (30), they found that in two magnesian calcite ranges of 1~5 and 20~25 mole %, magnesian calcite is stable and metastable, respectively. Thorstenson and Plummer also stated that the solubility of magnesian calcite is controlled by $[\text{Ca}^{++}] \cdot [\text{Mg}^{++}]$ in seawater. This concept

that $[Ca^{++}] \cdot [Mg^{++}]$ controls magnesian calcite stability or solubility was disputed by Lafon (32), who questioned the validity of the extrapolation method used in Plummer and MacKenzie's experiments (30) (also disputed by Stumm and Morgan (1)). The relative stability of magnesian calcite and pure calcite can be studied from simple thermodynamic equilibrium equations as provided by Stumm and Morgan (1). The equation for the dissolution of magnesian calcite containing x mole fraction of $MgCO_3$ can be expressed as reaction [6].



Also, dissolution of pure calcite, expressed in the reverse direction, is



The equilibrium constants are $K_{(x)}$ and $(K_{S,CaCO_3})^{-1}$ for reaction [6] and [7], respectively. To compare the stability of magnesian calcite to that of pure calcite, reaction [6] and [7] can be added to give reaction [8].



The equilibrium constant is

$$\frac{([Mg^{++}])^x}{[Ca^{++}]}$$

which is also equal to the product of $K_{(x)}$ and $(K_{S,CaCO_3})^{-1}$.

Therefore,

$$\left(\frac{[\text{Mg}^{++}]}{[\text{Ca}^{++}]}\right)^x = K_{(x)} \cdot (K_{s, \text{CaCO}_3})^{-1}.$$

Rearranged,

$$K_{(x)} = \frac{([\text{Mg}^{++}])^x}{[\text{Ca}^{++}]} \cdot K_{s, \text{CaCO}_3}.$$

This equation states that the relative solubility of magnesian calcite containing x mole fraction of MgCO_3 is governed not only by the mole fraction (x) of MgCO_3 in calcite but also by the ionic concentration ratio between Mg^{++} and Ca^{++} in seawater. Because $[\text{Mg}^{++}]/[\text{Ca}^{++}]$ is always larger than 1 in seawater, $K_{(x)}$ becomes greater than K_{s, CaCO_3} as mole fraction (x) increases. Although effect of solid solution formation and kinetic aspects are not considered in this simple thermodynamic equilibrium, it can be said that naturally observed magnesian calcite with a high MgCO_3 mole fraction is not a stable form. This assertion is supported by the observation made by Winland (33) that high magnesian calcite underwent transformation into aragonite. In seeded crystal experiments, Berner (24) found that magnesian calcite containing 7~10 mole% of MgCO_3 grew on the pure calcite seed crystals. Recently, Morse et al. (34) observed magnesian calcite formed on calcite seed crystals in surface seawater. Auger depth profiling showed no significant variation of magnesium signal. Quantitative analysis showed about 4 mole % of MgCO_3 in calcite.

Whether the stability of magnesian calcite is controlled by kinetics or thermodynamic equilibrium is still in dispute. However, observations of low magnesian (low-magnesium) calcite formation (24,30,31,34), even though magnesian calcite is more soluble than calcite, are generally believed to be due to the inhibiting effect of Mg^{++} . Using the solubility of calcite and dolomite reported by Hsu (35), Stumm and Morgan (21) stated that dolomite, $CaMg(CO_3)_2$, is the more stable form. However, the comparison of the solubilities obtained in Florida underground water to seawater environments is not appropriate.

Crystalline $CaCO_3$ has another structure, metastable aragonite. As shown in Table 1, and also measured by Morse et al. (36), aragonite is more soluble than pure calcite. It is generally believed that calcite nucleation and growth are retarded in the presence of magnesium ions and, as a result, aragonite precipitation is kinetically favored. Formation of aragonite is reported by several authors in various environments (20,24,27,37). However, it is hard to believe that naturally occurring $CaCO_3$ is the pure form of aragonite or calcite (1,31). The formation and stability of aragonite in seawater environment can be characterized in the same way as was calcite; even though metastable aragonite formation is kinetically favoured over calcite, incorporation of Mg^{++} into calcite is the dominant factor in $CaCO_3$ deposition (10,24,27,30,31,38).

There are other species which are known to have a similar inhibitory function to that of Mg^{++} for $CaCO_3$ precipitation: organic materials (39,40), sulfate (25) and phosphate (41). These species are generally believed to behave like Mg^{++} : occupation of growth site, charge neutralization, and growth site congestion. Even though a large amount of these species retard or prevent $CaCO_3$ precipitation, the influence of these species at seawater level concentration is not well known.

2.2 Properties of Calcareous Deposits

Beneficial aspects of calcareous deposits can be viewed as bifold:

- i) reduction of surface area directly exposed to seawater, and consequent decrease in cathodic current requirements.
- ii) mitigation of corrosion attack during power interruption, either accidental or for maintenance.

These advantageous aspects of calcareous deposits have been known for decades. In the early 1940's, Cox realized the beneficial effects of the deposits and suggested applying high current density of several hundred mA/ft^2 to obtain a coating mainly comprised of $Mg(OH)_2$ and $Ca(OH)_2$, the latter eventually transforming to $CaCO_3$ in the presence dissolved CO_2 (42,43). He viewed the deposit as a mixture of calcium salts dispersed in a matrix of $Mg(OH)_2$ which is serving as a bonding agent as cement bonds gravel in concrete. The application of this deposit to offshore drilling platforms with initial high current densities functioned

successfully in lowering total cathodic current requirements and also in mitigating corrosion problems after cathodic current was stopped for several months (44).

The first empirical relationship between properties of calcareous deposits and current densities was reported by Humble (45). He analyzed the deposits formed in seawater and found the variation of Ca-to-Mg ratio with current density. He concluded that low current densities provide the conditions favorable for CaCO_3 deposition as expected from solubility limits (see also Table 2). Because the deposits are formed in almost any situation where current densities are large enough to maintain protective potentials of steel, he claimed that self-healing ability of the deposits is one of the inherent properties that can be effectively employed to protect almost any surface regardless of shape and also seal any breakdown in the deposit which may occur from time to time.

The protective property of the deposits was also observed on galvanized steel. Denison and Romanoff (46) attributed the high corrosion resistance, exhibited by most of their galvanized specimens after outer Zn coating was removed by corrosion, to a thin coating deposited cathodically by the galvanic action between the outer Zn coating and the underlying steel.

Cox's view on calcareous deposits as an analogy of cement-gravel structure was well described in La Que's discussion (47). Cox noted that calcium-rich deposits were

more porous and magnesium-rich deposits were easily spalled. By using Humble's results (45), he suggested a medium range of current density for a proper mixture of the two properties. The range of 80~300 mA/ft² was recommended for "best" coatings and 50~400 mA/ft² for "useful" coatings. Preiser and Silverstein (48) agreed with Cox's view of calcareous deposits as mixtures of calcium and magnesium compounds. They recommended 100~200 mA/ft² for the best coating in which microscopic calcium (compound) particles prevent shrinkage cracks in the magnesium (compound) matrix. This was expected to result in a relatively tough and nonporous coating. They also reported several cases in which calcareous deposits were actually applied to Navy warships. According to this report, as far as the effectiveness of the deposits is concerned, the applications were very successful in mitigating corrosion problems at the sites where painting was damaged. However, because ship hulls were repainted during the dry docking period, the presence of the deposits caused a problem in cleaning the ship hulls. Another difficulty was the control of biofoulings. It was found that fouling problems could not be handled with calcareous deposits as easily as with anti-fouling paints.

Application of calcareous deposits to a ship hull was also tried by Harvey and Streever (49). The paint on the hull was removed in three places and the surface cleaned. Initially 100 mA/ft² was applied for 80 hours and then

current was maintained over 110 days with 12 hours on and 12 hours off. They reported no perceptible corrosion on the bare steel surface at any time during the experiment. From the context, it could be found that they tried to obtain a uniform coating which would replace paint or be overcoated with paint. Such uniform coatings could not be observed. Apparently, the object of the Cox process (42,43) was to develop a deposit which would obviate the need for painting. From the corrosion standpoint, such a deposit is satisfactory. However, its application to ship hulls could not remove the problems of nonuniformity and biofouling (48,49).

Calcareous deposits were also found on aluminum under cathodic protection conditions (50,51). Kole (51) studied the relationship between the deposit weight and the total amount of charge on steel, aluminum and galvanized iron. Potential varied between -0.992 and -1.473V vs. Ag/AgCl. The weight to charge plot showed a linear relationship between them without any noticeable difference among the three different materials. This indicates that the deposit gained weight from the cathodic charge throughout the 804 hour period and that the difference in substrate material did not affect the deposit formation.

Using the IR internal reflection technique, Smith and Mattson (52) studied calcareous deposits formed on a germanium plate in seawater at -1.15V vs. SCE. The peaks of CO_3^{2-} and SO_4^{2-} were observed. Deposits had two different

morphological shapes, one a forming plate-like background layer and the other acicular particles on top of the background layer. In X-ray analysis, the plate-like background showed strong signals of magnesium and chlorine. The acicular crystals showed magnesium and calcium along with chlorine, potassium, sulfur, and germanium. From these analyses, they concluded that the deposits had carbonates, hydroxides, and sulfates of calcium and magnesium.

Pirogov et al. (53) studied calcareous scales formed in Black Sea. Three potentials of -0.85, -1.0, and -1.2V vs. Ag/AgCl electrode were employed for their 300 hour experiments. At -0.85V, a fine-grained, dense, and thin film with good adhesion to the metal was observed. A continuous film was completed after 210 hours. At -1.0V, the deposit became more porous and coarse grained. A continuous film was observed after 140 hours. At -1.2V, a 70-hour period was necessary to form a completely continuous film. The thick film was coarse-grained and friable and was easily separated from metal surface. They stated that hydrogen evolution reaction caused the easily-spalling film and provided frequent fluctuation of current as a supporting evidence. In an analogy to Ohm's law, $R = V/i$, they calculated the resistance of the deposit after the 300 hour polarization was completed.

$$R_{\text{deposit}} = \frac{V_{\text{applied}}}{i} .$$

The deposit formed at -0.85V showed $R_{\text{deposit}}=5.0 \text{ } (\Omega \cdot \text{m}^2)$, at -1.0V, $R_{\text{deposit}}=2.5$ and at -1.2V, $R_{\text{deposit}}=1.2$. It was concluded that -0.85V deposit had the highest resistance and, therefore, was the best deposit. This method of comparing one resistance to another needs careful application for two different potentials because the resistance is a function of potential. The electrochemical reactions at -0.85V are different from that at -1.0V and -1.2V in their rates. Also, the hydrogen evolution reaction is activation controlled and current increases exponentially with potential. As a result, if two imaginary deposits with exactly same properties are tested with this method, a higher cathodic potential always yields a lower resistance. To validate such resistance measurements, the same potential has to be used.

Observation of deposit formation in city water environments was made by Schwerdtfeger and Manuelle (54). Spectrochemical analysis of the coatings on specimens cathodically protected for 5 years showed strong signals of Ca, Mg and Si. The coatings were called carbonaceous or silicious deposits, apparently because of the richness in silicon.

Using artificial seawater, Grigorev and Popov (55) studied the deposits formed at different current densities

of 50, 100, 150, 200 and 250 $\mu\text{A}/\text{cm}^2$ up to 280 hours. Deposit weight was found to be proportional to deposition time and current density. Degree of protectiveness of the deposits was studied by comparing deposit weights to a "minimum protective" current density which was defined as the cathodic current density to achieve -0.58V vs. SHE ("minimum protective" potential). The 280 hour polarization time was equally divided into four divisions. At the end of each division, the cathodic current density to achieve the "minimum protective" potential was measured and plotted against deposit weight. The curves had the shape of a $y=1/x$ curve. The inflection point was at about 2 mg/dm^2 , which corresponded to approximately 70~210 hours depending upon applied current density. After the inflection point, the current leveled off and further increase in deposit weight had little effect on the "minimum protective" current. Their observation indicates that after the film develops to a certain extent, the film may break or develop cracks so that further increase in weight provides no additional resistance to the film in retarding the flow of current across the film. Also the presence of the "best" current density (150 $\mu\text{A}/\text{cm}^2$) in terms of the "minimum protective" current density indicates that properties, physical or chemical, vary with current density applied.

Since calcareous deposits started to attract interest from scientists and engineers, Ca-to-Mg ratio has been continuously discussed. The belief is, as shown in Humble's

analysis (45), that as current density increases, surface pH increases and the ratio decreases. Because CaCO_3 is already supersaturated in seawater while Mg(OH)_2 is not, richness in calcium content has been thought to indicate an enduring deposit. The variation of Ca-to-Mg ratio with current density and temperature was also reported by Rodrigo (56). The ratio increased up to 5, which was observed at $50 \mu\text{A}/\text{cm}^2$ and 60°C . Guillen and Feliu (8) also reported similar behavior of the ratio with current density and temperature. Deposits were formed in Barcelona seawater at 0, 20, 40 and 60°C by supplying cathodic currents of 10, 50, 100 and $150 \mu\text{A}/\text{cm}^2$ with each experiment duplicated in the static and in the aerated (intended for agitation) condition. For example, at 20°C and aerated, the ratio increased from 0.1 at $150 \mu\text{A}/\text{cm}^2$ to 2.4 at $50 \mu\text{A}/\text{cm}^2$. In Table 2, variation of degree of supersaturation of Mg(OH)_2 and CaCO_3 with pH is listed. From the rapid increase in Mg(OH)_2 degree of supersaturation with surface pH increase, the variation of the ratio was explained. Deposit weights were measured at different temperatures. They stated that, at high temperature, the diffusion coefficient increases whereas diffusion layer thickness decreases, according to Glasstone (57). Increase in diffusion coefficient and decrease in diffusion layer thickness accelerated the arrival rate of Ca^{++} and Mg^{++} from the solution. An accompanying phenomenon of accelerated OH^- diffusion rate from metal surface to bulk solution was not considered. Noting that the concentration

of OH^- is the primary driving force for deposit formation, it has to be considered for a complete explanation. From the context, however, it can be read that the authors believed that the positive effect (accelerated diffusion of Ca^{++} and Mg^{++}) overcomes the negative effect of accelerated diffusion of OH^- . Hartt et al. (58) suggested, as an explanation to the deposit weight-temperature relationship, that precipitation kinetics is enhanced at higher temperatures.

Recently a few papers have been published in this area. Wolfson and Hartt (7) studied the effect of potential and seawater velocity on the protective properties of the deposits. Potentials were varied among -0.78, -0.93 and -1.03 vs. SCE and velocities were varied among 8, 31 and 107 cm/sec. Current density dropped gradually and leveled off after 100 hours. Film thickness increased with increase in time and cathodic potential and decreased with increase in solution flow rate. Film thickness was larger at -1.03 than at -0.93V and final current density was lower at -1.03. However, the same relationship did not always hold. Their observations are very similar to those of Grigorev and Popov (55) in two aspects:

- 1) Wolfson and Hartt noted the presence of "better" current density or potential which yielded "better" deposit in terms of potential or current measurement
- 2) Wolfson and Hartt noted that as the deposit grew in thickness with time, current density or "minimum protective" current density leveled off and further

increase in thickness had little effect on the protective property of the deposit measured as current.

A critical review paper was published recently (58). Discussing chemical compositions of deposits, the authors stated that several weight percentages of strontium were reported in one case (59). Though the coprecipitation of SrCO_3 with CaCO_3 forming a solid solution is not unanticipated, such a concentration is too high. When two solid materials form a solid solution in equilibrium with solution, the solubility of the minor constituent is appreciably reduced by the effect of the increase in its activity in the solid solution. In the case of SrCO_3 forming a solid solution with CaCO_3 , as illustrated by Stumm and Morgan (1):

$$\frac{K_{s,\text{CaCO}_3}}{K_{s,\text{SrCO}_3}} = D = \frac{[\text{Ca}^{++}] \cdot X_{\text{SrCO}_3}}{[\text{Sr}^{++}] \cdot X_{\text{CaCO}_3}} \cdot \frac{f_{\text{SrCO}_3}}{f_{\text{CaCO}_3}}$$

$$= D_{\text{obs}} \cdot \frac{f_{\text{SrCO}_3}}{f_{\text{CaCO}_3}}$$

where K_s : solubility product
 D : distribution constant calculated from solubility data
 D_{obs} : observed distribution constant
 X : mole fraction in solid solution
 f : activity coefficient in solid solution.

It can be seen from this equation that the increase in activity coefficient of the minor constituent (SrCO_3) of the solid solution increases its mole fraction in the solid solution over the ratio that is calculated from solubility data. Using the reported values of $D=10$ and $D_{\text{obs}}=0.14$ (33), $X_{\text{SrCO}_3} \approx 0.2$ mole% can be obtained. This value is in good agreement with Humble's analysis (45) of 0.1~0.5 mole%. The cited value is far off from the expectation of equilibrium thermodynamics, probably controlled by precipitation kinetics. Wolfson and Haart reported that Hilbertz (60) found aragonite structure in calcareous deposits from X-ray analysis. On Guillen and Feliu's data about deposit weight-temperature relation (8), Wolfson and Haart stated that "consistent with this, it is generally recognized by the cathodic protection industry that calcareous deposits form more readily upon metal surface in warm water than in cold water" (4, p. 8), supporting their suggestion of thermally activated deposit formation mechanism.

Recently another study has been done by Ambrose et al. (61) concerning chemical analysis of calcareous deposits. They used rotating disc electrode to simulate the variation of seawater flow rate by rotating an electrode screwed into a spindle. In their "galvanodynamic" experiments in which current was controlled to maintain the electrode potential within the range between -0.85 and -0.90V vs. Ag/AgCl electrode in every two minute period, initial current density of $\sim 13 \text{ mA/cm}^2$ was applied for a few seconds. As

they pointed out, in galvanostatic experiments in which constant current was applied throughout experiments (most of the studies previously discussed have been done in this mode), severe corrosion occurred with iron compounds formed around small pits. Under these conditions, the contribution by deposits to decrease in cathodic current is obscured by the effect of rust because rust itself can function as a surface film.

Artificial seawater according to ASTM D-1141 (ASTM), natural seawater taken from St. Augustine Beach (SAB) and natural seawater taken from Crescent Beach (CB) were used. The "protective" current density to maintain the "protective" potential between -0.85 and -0.90V varied among the different solutions. At the electrode rotation speeds of 100, 250, 500, 1000 and 2500 rpm, the "protective" current densities after one hour, at which current density vs. time curve leveled off, were 50, 300, 480, 550 and 700 $\mu\text{A}/\text{cm}^2$ whereas 40, 120, 160, 250 and 360 $\mu\text{A}/\text{cm}^2$ were necessary to maintain the protective potential in SAB seawater. Interestingly, in CB seawater, the current densities were similar to those observed in ASTM seawater. Though the authors did not give explanation to this phenomenon, it is apparently due to the variation of seawater from place to place. Studies have found that seawater varies in temperature, dissolved matter, pH, etc. with geographical location (2,62-63). Also it is conceivable that small variation of micro-organisms can

influence the formation of calcareous deposits from their photosynthesis and respiration, changing the distribution of carbonate system among its elements (19,33).

Morphology studies showed that globular particles have grown, effectively covering electrode surface. The difference in morphology between zero and 250 rpm group and 1000 and 2500 rpm group was that the globular particles in the low rpm group were smaller (diameter $\approx 0.5 \mu\text{m}$) than those in high rpm group (diameter $\approx 1 \mu\text{m}$) under SEM.

Electron microprobe (EMP) analysis showed even distribution of the elements of Ca, Mg, Si and S on electrode surface. Energy dispersive X-ray analysis results showed a difference between the deposits formed under static condition and those formed in flowing solution condition. In the former, distinct Mg and Ca peaks were observed whereas in the latter Ca peak was not shown, indicating low Ca deposits formed under flowing solution conditions. However, in the energy dispersion X-ray spectra obtained from the deposits formed under flowing solution condition, very large Fe peaks (K_{α} and K_{β}) could be seen. This indicates that the thicknesses of the deposits were so small that strong signals were obtained from the iron substrate. As a result, a small peak from Ca, if there was any, could be obscured by the continuous spectra of Fe. Information about the difference in chemical composition between flowing condition and static condition could not be drawn. The attempt by Ambrose et al. to relate Ca-to-Mg ratio to the

conditions under which the deposits were formed did not show any consistent trend. Electron microprobe analysis was employed for the deposits and atomic absorption (AA) was used for the solution into which the deposits were dissolved. In EMP analysis, the ratio varied from 0.50 to 1.97 (natural seawater) and in AA analyses, the ratio varied from 0.16 to 23.0. No consistent trend could be found from these scattered data.

Their Auger depth profiling showed chemical variation across the deposit thickness. By using a 2KeV argon beam ion sputtering technique, Ca-to-Mg ratio (actually Mg-to-Ca ratio in their paper) was plotted against the time of sputter etching. The ratio increased up to 24 minute period and decreased again. Assuming the sputtering rate of several hundred angstroms per minute, it is hard to think that the depth profile represents the variation of Ca-to-Mg ratio across the total thickness of the deposit. Instead, it is very likely that the depth profile represents the chemical composition across a few globular particles.

Back in 1958, Klas (9) studied calcareous deposits formed in artificial seawater which had 0.1 g/l of CO_3^{2-} . Natural seawater has about 0.15 g/l of HCO_3^- and about 0.1 mg/l of CO_3^{2-} . In the high $[\text{CO}_3^{2-}]$ solution, they obtained deposits containing more than 80 weight % of CaCO_3 . They also found that both aragonite and calcite were formed as well as brucite ($\text{Mg}(\text{OH})_2$). Small well-defined particles were deposited at -0.780V vs. SCE and, as the cathodic

potential increased (more negative) up to -1.080V , the particles became larger and more blurry. This behaviour was attributed to the increase in $\text{Mg}(\text{OH})_2$ concentration in the deposit as potential became more negative.

Culberson (64) studied the effect of several parameters on cathodic current requirement and deposit formation. By comparing the cathodic current density in seawater and that in Mg^{++} free artificial seawater, he found that the presence of Mg^{++} markedly increased current requirements. This was attributed to the inhibitory effect of Mg^{++} on CaCO_3 precipitation. By controlling the partial pressure of N_2 , O_2 and CO_2 gas mixture bubbled into solution, he found that an increase in dissolved O_2 amount up to the air saturation level increased the cathodic current requirement and then further increase in O_2 amount did not increase current. pH was varied between 8.2 and 8.65 by controlling partial pressure of CO_2 of the gas mixture. Current was found to decrease as pH increases. At high pH, carbonate system has more CO_3^{--} concentration increasing the degree of CaCO_3 supersaturation. Investigation of current requirements at various CO_3^{--} concentrations showed a linear relationship and verified that the rate of CaCO_3 precipitation is controlled by its degree of supersaturation.

Research efforts have also been done in the desalination area (10,65-75). However, most of the work was done at high temperatures at which the desalination process is carried out. The deposits were very rich in CaCO_3 and

differently hydrated CaSO_4 compounds because these species have reduced solubilities at high temperatures as shown in Table 4 (76,77). Nair and Misra (10,65) studied deposits formed at 30°C in seawater with 3 mA/cm^2 current density. After 6 hours, deposits were analyzed. By assigning magnesium to Mg(OH)_2 and Ca to CaCO_3 and CaSO_4 , 76.7% of Mg(OH)_2 , 19.6% of CaCO_3 and 2.6% of CaSO_4 could be obtained. X-ray diffraction pattern showed mostly calcite and brucite structures. Scale weight increased with time with diminishing rate because the concentrations of the deposit forming elements were gradually depleted from solution.

Table 4 Variation of the solubilities of CaCO_3 (calcite), Mg(OH)_2 and CaSO_4 compounds with temperature in water

Temp ($^{\circ}\text{C}$)	CaCO_3^{a}	$\text{Mg(OH)}_2^{\text{b}}$	CaSO_4^{c}	$\text{CaSO}_4 \cdot \frac{1}{2} \text{H}_2\text{O}^{\text{c}}$	$\text{CaSO}_4 \cdot 2\text{H}_2\text{O}^{\text{c}}$
15	9.9×10^{-9}	2.21×10^{-11}	-	-	-
25	8.7×10^{-9}	-	-	-	4.3×10^{-7}
40	-	-	4.2×10^{-7}	12.2×10^{-7}	4.2×10^{-7}
60	-	-	2.4×10^{-7}	7.6×10^{-7}	3.6×10^{-7}
75	-	0.51×10^{-11}	-	-	-

Note: not seawater

^a CRC Handbook (76)

^b Water Quality and Treatment (77)

^c Lu and Fabuss (4)

CHAPTER 3 EXPERIMENTAL

3.1 Materials

These studies were performed using pure iron made by a vacuum remelting process as electrode material. Its composition is shown in Appendix 3. Three specimens with different geometry were used. For electrochemical studies, specimen A and specimen B were used. Specimen A has a diameter of 4.3 mm. The stock iron rod was machined to size and press-jointed to a brass base which has a thread. The assembly was mounted into a nylon tubing. The gap of about 2 mm between the center piece and the nylon tubing was sealed with epoxy resin in vacuum. Specimen A was seriously damaged during the course of this research because of the accidental disconnection of a salt bridge. The discontinuity of the circuitry of the electrochemical cell system caused a very large cathodic current to flow. Blistering was observed along the edge, apparently due to the hydrogen penetrated into the iron piece. Another specimen was made for further electrochemical measurements. Specimen B has the same geometry as specimen A except that the diameter of the center piece was slightly increased to 5.0 mm. This was done to reduce the effect of gap opening between the center piece and the surrounding

epoxy layer. Except for the factorial design experiments, specimen B was used throughout. Specimen C with different geometry was used for X-ray photoelectron spectroscopy analysis (XPS or ESCA) and infrared analysis. Because of the high vacuum requirement of XPS system, specimen B, which was permanently mounted in such outgassing polymeric materials as nylon and epoxy, could not be directly put into XPS vacuum. Therefore, a removable type of specimen became necessary. An iron disc was made from the same pure iron stock into 12 mm in diameter and 5 mm in thickness. This disc was attached to a brass adaptor by applying a small amount of polyester resin on the side wall of both the specimen and the adaptor. After experiment, the thin polyester layer was peeled off and the disc was separated from the adaptor. This specimen C not only met the high vacuum requirement but also was larger than the size of the ESCA X-ray beam. Also, its large surface area was suitable for infrared analysis.

The solutions used in this study were prepared according to ASTM D-1141-75 Substitute Ocean Water using ACS reagent grade chemicals. Ionic composition is shown in Table 3. Distilled and deionized water which had a conductivity of $4 \times 10^{-7} \text{ ohm}^{-1} \text{ cm}^{-1}$ was used. After adding chemicals, $4.8 \times 10^{-2} \text{ ohm}^{-1} \text{ cm}^{-1}$ was measured. Before mixing, water was stirred with a magnetic stirrer for ten minutes to ensure air saturation. The procedure of mixing was modified from the ASTM standard. Instead of adding NaHCO_3 into the

No. 2 stock solution, it was weighed and kept in a plastic container with the appropriate amount of NaCl and Na₂SO₄. 0.1 N NaOH was slowly added with stirring to avoid possible precipitation. For deposit-free experiments, MgCl₂·6H₂O, CaCl₂ and SrCl₂·6H₂O, which are the source chemicals for Mg⁺⁺, Ca⁺⁺ and Sr⁺⁺, were substituted with an additional 6 grams of NaCl and the same conductivity of 4.8×10^{-2} ohm⁻¹cm⁻¹ could be maintained.

3.2 Surface Preparation

Specimens were ground with SiC paper down to 600 grit and polished with 6 μm diamond paste. Because alcohol and acetone damage the epoxy layer of the specimen assembly, electrodes were ultrasonically cleaned in soap solution between each polishing step. Though such fine surface preparation is not employed in industry, it was necessary for surface area reproducibility and surface sensitive analytical work. Specimens for electrochemical measurements were frequently ground with 320 grit SiC paper to eliminate any possible gap opening between the epoxy layer and the iron piece.

3.3 Equipment

Electrochemical measurements were made using a rotating disc electrode system. The electrode was attached to a spindle which was designed to fit a Pine Instruments ASR-2 rotator unit. A Princeton Applied Research (PAR) potentiostat and a PAR programmer were used for electrochemical measurements.

The electrochemical cell has a 1 liter capacity with an outer water jacket connected to a temperature controller. Solutions were made with distilled deionized water, the temperature of which was adjusted to experiment temperature prior to mixing.

Scanning electron microscopy was carried out with JEOL JSM 35C and JSM 35CF microscopes. X-ray analysis was done with an Ortec EEDS II attached to JSM 35C microscope. A Kratos XSAM 800 with 1253.6 eV mg K_α source was used for X-ray photoelectron spectroscopy. Infrared analysis was carried out using a Nicolet Fourier transform infrared (FTIR) MX-1 with a 1200S data station in diffuse reflection mode in nitrogen gas environment. The stage was manufactured by Barnes Analytical Co.

3.4 Current Measurements

A 2^4 factorial design technique was employed (Appendix 2) to study the influence of parameters on cathodic current and deposit formation. The four parameters selected for these studies are cathodic potential (E), electrode rotation speed (RPM), solution pH (pH) and solution temperature (T). Each parameter was given two levels which are shown in Table 5. Therefore, a total of 16 different conditions were investigated. Potential had two levels of -0.8 and -1.0V vs Ag/AgCl. At -0.8V, oxygen reduction reaction takes place and, at -1.0V, both oxygen reduction and hydrogen evolution occur. For the two levels of rotation speed, 500 and 1000 rpm were studied. Solution pH had two values of 8.3 and 7.9

which represent high and low seawater pH values, respectively. The two temperatures used were 23 and 16°C, high and average temperature of natural seawater, respectively. Each of the two levels will be abbreviated to level 0 (zero) and level 1 as defined in Table 5. Each experiment was duplicated. Experimental period was 2 1/2 hours. For other experiments, the period was appropriately selected. Current was measured with Keithley 602 Electrometer. The output terminal which provides 1V full-scale deflection voltage output was connected to an Easterline Angus stripchart recorder.

Table 5 Parameters and their levels

<u>Level</u>	<u>E (V)</u>	<u>RPM (rpm)</u>	<u>pH</u>	<u>T (°C)</u>
0	-0.8	500	8.3	23
1	-1.0	1000	7.9	16

After cathodic polarization is over, specimens were removed from the cell and dried under N₂ stream and kept in a desiccator for further studies. An Ag/AgCl reference electrode was used throughout these experiments. To measure current at a different potential or at a different rotation speed, thumbwheels were slowly turned to the desired setting and a few minutes were allowed before reading until the current became stable.

3.5 Morphology and Chemical Analysis

For SEM studies, deposits were sputter coated with an Au-Pd alloy. This coating was employed to provide an electron flow path and to enhance secondary ion yield (78). To avoid strong Fe signals (characteristic and continuous) from the substrate iron, deposits were peeled off using acetate replicating tape and acetone and coated with carbon for X-ray analysis. Because of incomplete removal of deposits, quantitative analysis was not attempted. The deposits which were to be subsequently analyzed with EDX were not coated. Instead, 5 KeV electron beam was used to minimize charge build-up at the expense of imaging.

For ESCA work, specimen C was polarized under the same conditions as electrochemical experiments. Specimen was usually stored in desiccator for a few days before analysis. Resolution was controlled by properly adjusting the opening of the hemispherical spectrum analyzer.

Inductively coupled plasma (ICP) was employed for solution analysis to detect any change in concentration after experiment. However, this study was discontinued once its incapability to detect very small change was realized.

CHAPTER 4 RESULTS

Cathodic currents, measured after the deposit was formed on the electrode surface for $2\frac{1}{2}$ hours, are listed in Table 6 under the heading of "with deposit." From the experiments performed in the solution which does not contain deposit forming elements (Ca^{++} , Mg^{++} and Sr^{++}), cathodic currents were measured and also listed in Table 6 under the heading of "without deposit." From these measurements, four main effects and eleven interaction effects were calculated for both "with deposit" experiments and "without deposit" experiments (Table 7). The methods to calculate the effects and the standard errors are shown in Appendix 2. Zeroes (0) and ones (1) in Table 6 represent the values preassigned to each parameter (Table 5).

Taking the measured current "without deposit" as the reference, the effectiveness of surface coverage by calcareous deposit (effective surface coverage) was calculated by subtracting the current with deposit from the reference current and dividing the result by the reference current. For example, in case of (1110), reference current was $146\text{ }\mu\text{A}$ and the current "with deposit" was $125\text{ }\mu\text{A}$. Therefore, the effective surface coverage for (1110) experimental condition is $(146-125)/146 = 14\%$. Sixteen

Table 6 Current measurements under various conditions

E	RPM	pH	T	With deposit (μ A)			Without deposit (μ A)		
				First run	Second run	Avg	First run	Second run	Avg
0	0	0	0	36	35	35.5	79	87	83
1	0	0	0	65	58	61.5	115	119	117
0	1	0	0	61	57	59	121	122	121.5
1	1	0	0	69	77	73	138	146	142
0	0	1	0	65	66	65.5	86	89	87.5
1	0	1	0	95	100	97.5	109	107	108
0	0	1	0	94	89	91.5	118	121	119.5
1	1	1	0	125	125	125	146	146	146
0	0	0	1	56	58	57	81	86	83.5
1	0	0	1	67	73	70	100	105	102.5
0	1	0	1	78	81	79.5	120	119	119.5
1	1	0	1	87	95	91	140	128	134
0	0	1	1	68	73	70.5	79	87	83
1	0	1	1	95	89	92	105	108	106.5
0	1	1	1	102	105	103.5	117	118	117.5
1	1	1	1	125	118	121.5	131	138	134.5
Avg						80.8			112.8

Table 7 Main and interaction effects

<u>Effect</u>	<u>With deposit (μA)</u>	<u>Without density (μA)</u>
E	21.2 \pm 1.3	21.9 \pm 1.4
RPM	24.3	32.9
pH	30.1	-0.1
T	9.6	-5.4
E*RPM	-1.9	-2.3
E*pH	5.1	-0.1
E*T	-5.2	-3.4
RPM*pH	4.7	0.2
RPM*T	2.2	-0.4
pH*T	-7.6	0.6
E*RPM*pH	1.4	2.2
E*RPM*T	0.7	-0.4
E*pH*T	-1.3	1.8
RPM*pH*T	0.1	-1.4
E*RPM*pH*T	-1.9	-2.7

Note: \pm 1.3 and \pm 1.4 are standard errors. Calculation procedure is given in Appendix 2.

effective surface coverages obtained from 16 different experimental conditions were divided into two groups: Group Oxy (OXXX) and Group Hydr (1XXX). The letter "X" in the brackets indicates that the level of the corresponding parameter was either 0 or 1. Each group was divided into two subgroups in three different ways: RPM-0-Subgroup (XOXX) and RPM-1-Subgroup (X1XX), pH-0-Subgroup (XXOX) and pH-1-Subgroup (XX1X), and T-0-Subgroup (XXXO) and T-1-Subgroup (XXX1). Therefore, the subgroup of RPM-0-Subgroup in Group Oxy covered four different experimental conditions of (0000), (0010), (0001), and (0011). Likewise, each of the other subgroups represented four different experimental conditions. The grouping was done in a similar way. The result is shown in Table 8.

In Table 9, the currents were measured after one experimental condition was followed by another. The schedule for Run 3 will be explained as an example. Initially, deposit was formed at 1000 rpm (0100). After two hours, rotation speed was reduced to 500 rpm (0000) without interruption and another two hour cathodic protection was maintained. Current was measured at the end of the experiment. It should be noted that from this set of experiments on, Specimen B was used because Specimen A was damaged during this study.

In Figure 1, the deposit was formed under one set of conditions. Intermittently, the rotation speed was changed either from 500 to 1000 rpm or from 1000 to 500 rpm,

Table 8 Effective surface coverage

<u>Group</u>	<u>Group Oxy (OXXX)</u>	<u>Group Hydr (1XXX)</u>
RPM-0-Subgroup (XOXX)	31 %	26 %
RPM-1-Subgroup (X1XX)	30	26
pH-0-Subgroup (XXOX)	42	40
pH-1-Subgroup (XX1X)	19	12
T-0-Subgroup (XXXO)	38	30
T-1-Subgroup (XXX1)	23	22
Average	31	26

Note: $E.S.C. = \frac{i_{\text{without deposit}} - i_{\text{with deposit}}}{i_{\text{without deposit}}}$

Table 9 Combination of different experimental conditions

<u>No.</u>	<u>Initial (2 hrs)</u>	<u>Followed by (2 hrs)</u>	<u>Current</u>
Run 1	0100	0100	52 μ A
Run 2	0000	0100	46
Run 3	0100	0000	35
Run 4	0000	0000	35
Run 5	1000	1000	71
Run 6	0000	1000	98
Run 7	1000	0000	29
Run 8	0000	0000	35

For the convenience of comparison, each notation can be interpreted in the following way omitting common parameters:

Run 1 ~ Run 4 0000 : 500 rpm
 0100 : 1000 rpm

Run 5 ~ Run 8 0000 : -0.8 V
 1000 : -1.0 V

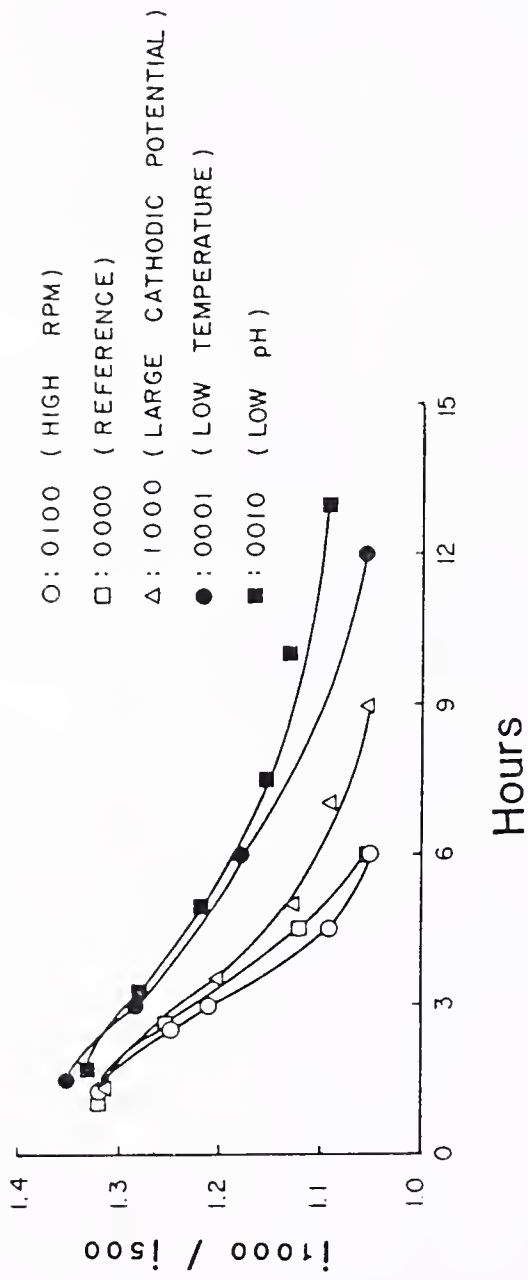


Figure 1 Decrease in the Ratio of i_{1000}/i_{500} With Time

depending upon the initial rotation speed. The ratio of the current measured at 1000 rpm (i_{1000}) to the current measured at 500 rpm (i_{500}) was plotted against time. Each of the five curves of Figure 1 represents (0000), (1000), (0100), (0010) and (0001). Except for (1000) and (0100), rotation speed was increased from 500 to 1000 rpm. For (0100), rotation speed was decreased from 1000 to 500 rpm. For (1000), after the cathodic potential was decreased from -1.0 to -0.8V, current was measured for i_{500} . Then rotation speed was increased to 1000 rpm for i_{1000} measurement. For all of the experiments, rotation speed and/or cathodic potential were set back to original values after i_{1000} measurement. In case of rotation speed change, a stable current was reached almost instantaneously and current went back to the previous value when the rotation was set back to the original speed. In the case of potential change, the current did not stabilize even after several minutes and the probable error caused by using the unstable current could obscure the exact evaluation of the ratio and the exact nature of the deposit formation at (1000). It has to be noted that i_{1000} and i_{500} were measured at -0.8V for all of these experiments. Experiments were discontinued when i_{1000}/i_{500} reached 1.05 ± 0.01 . Throughout the (0010) experiment, 0.1N H_2SO_4 was added at the rate of 1 drop for every hour to maintain pH 7.9. Because no automatic pH adjusting equipment was available, the (0010) experiment

could not be extended beyond thirteen hours so that the ratio could reach the same value as the others.

In Figure 2, the current vs. time relationship is shown. Deposit was formed at (1000) or $-1.0V$. Intermittently, the potential was changed to $-0.8V$. The current measured after the potential change ($i_{-0.8}$) was subtracted from the current measured before the current change ($i_{-1.0}$) and this difference was plotted against time on the right vertical scale. It has to be noted that positive values are always used for cathodic currents throughout this thesis. Therefore, $i_{-1.0}$ is larger than $i_{-0.8}$ and the difference is always positive. The difference was divided by $i_{-1.0}$ and multiplied by 100 and is shown on the left vertical scale.

Figure 3 is similar to Figure 2. But the deposition condition was (0001), or $16^{\circ}C$. Intermittently, the potential was changed from $-0.8V$ of (0001) to $-1.0V$. The definitions for the currents, $i_{-1.0}$ and $i_{-0.8}$, are the same as in Figure 2. To avoid a large transient current, the potential was changed by slowly turning the potential control thumbwheel at the rate of $0.1 V/min$, approximately.

Figures 4 through 8 are the scanning electron microscope (SEM) pictures, each of which was taken after the experiment for Figure 1 was finished. Therefore, the SEM pictures were taken after different periods of time.

Figure 9 is the electrode surface after deposit was removed with a Kimwipe paper. The specimen was stored in a dessicator for five days.



Figure 2 Variation of Hydrogen Current ($i_{-1.0} - i_{-0.8}$) and Its Percentage With Time

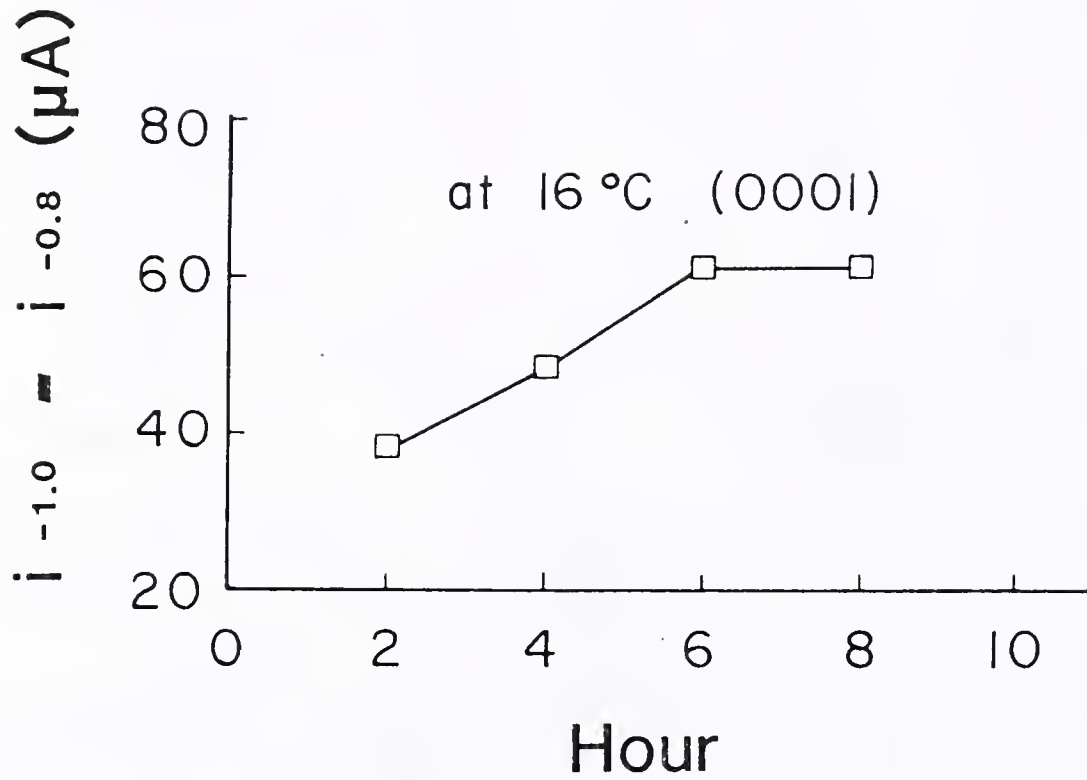


Figure 3 Variation of $i_{-1.0} - i_{-0.8}$ With Time



Figure 4 SEM Micrograph of Deposit Formed at (0100);
-0.8V, 1000 rpm, pH=8.3, 23°C

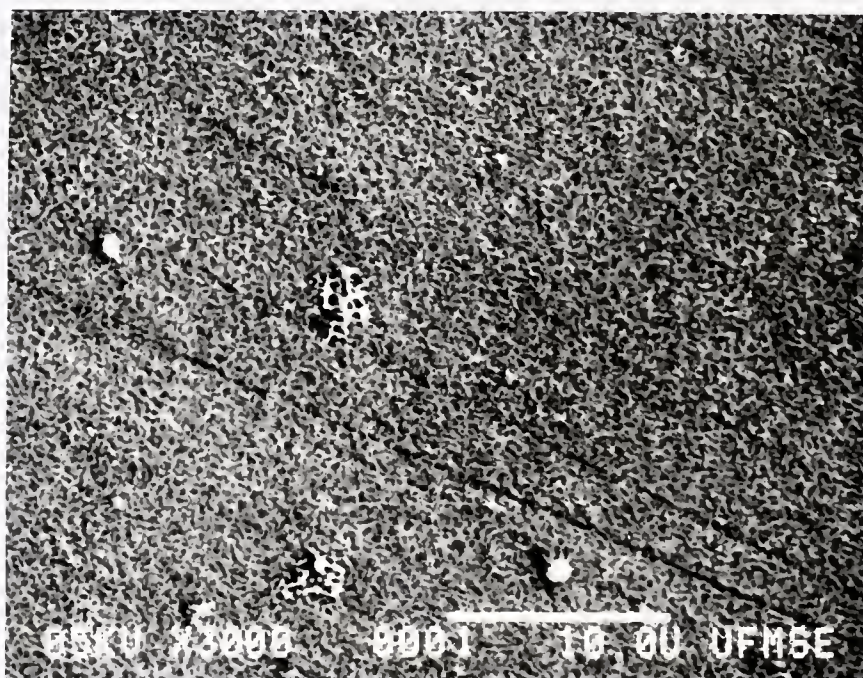


Figure 5 SEM Micrograph of Deposit Formed at (0000);
-0.8V, 500 rpm, pH=8.3, 23°C

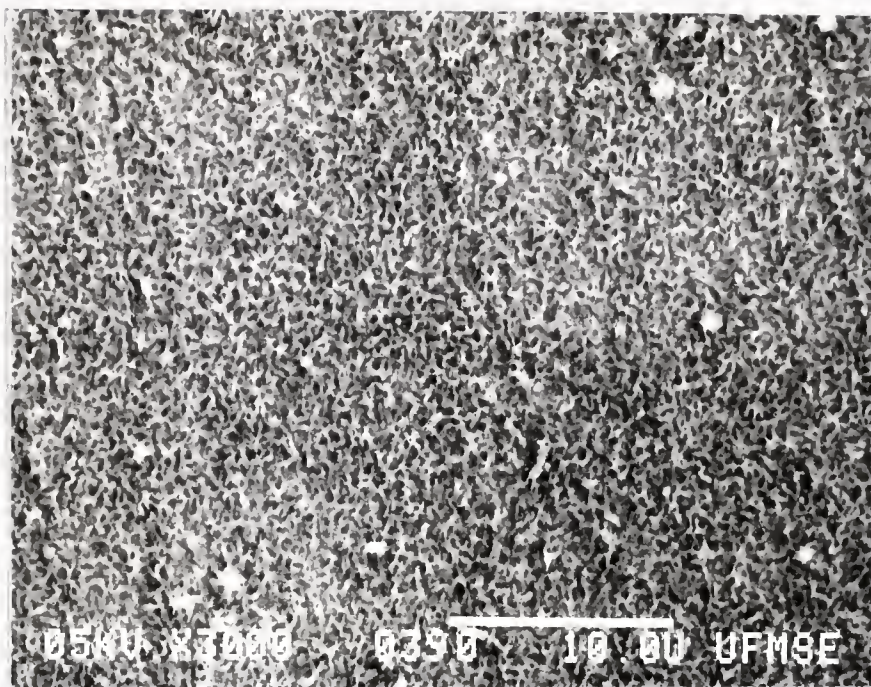


Figure 6 SEM Micrograph of Deposit Formed at (1000);
-1.0V, 500 rpm, pH=8.3, 23°C

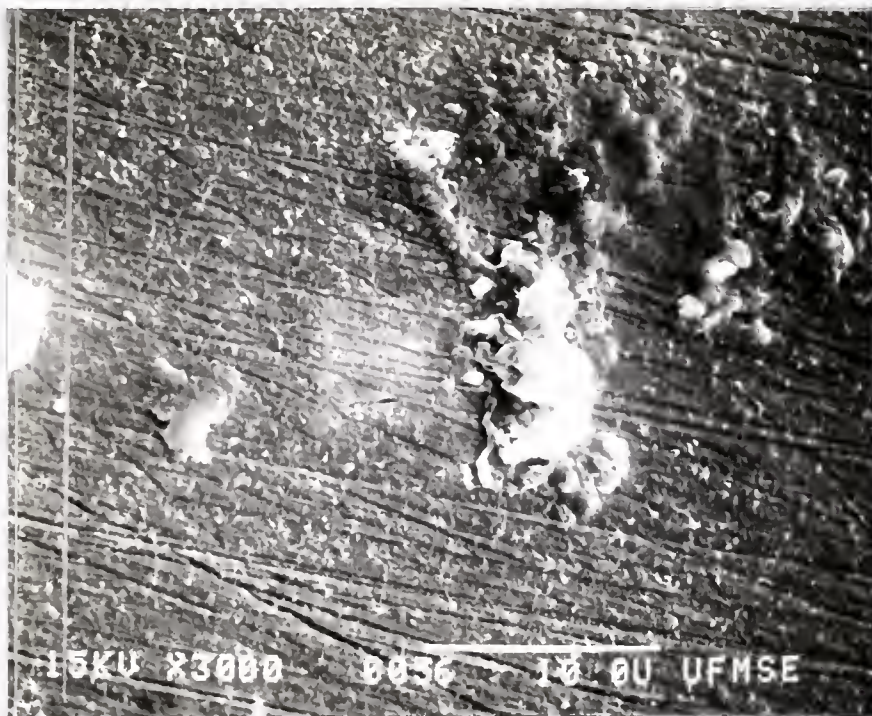


Figure 7 SEM Micrograph of Deposit Formed at (0001);
-0.8V, 500 rpm, pH=8.3, 16°C

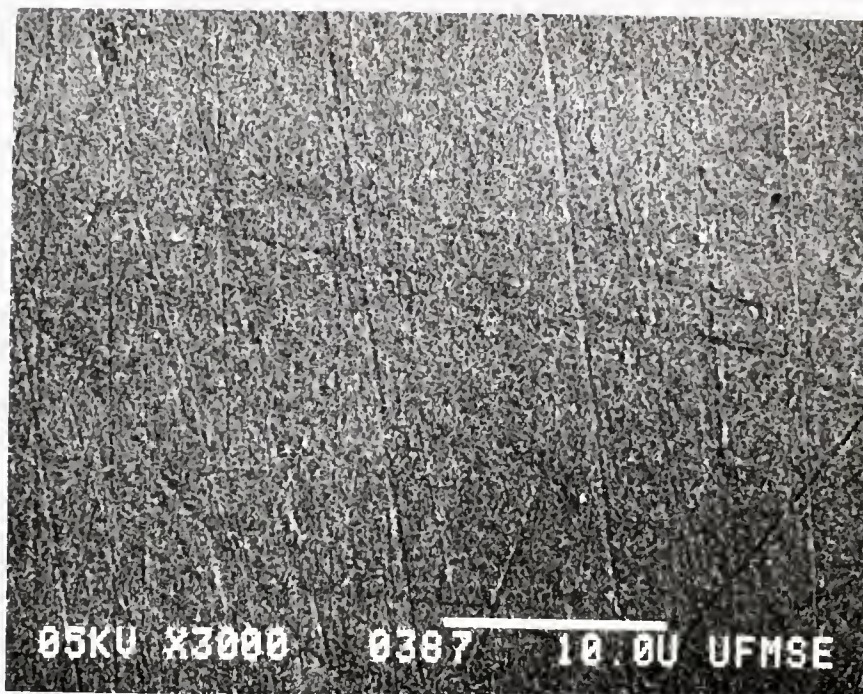


Figure 8 SEM Micrograph of Deposit Formed at (0010);
-0.8V, 500 rpm, pH=7.9, 23°C



Figure 9 Electrode Surface After Deposit Was Removed With
a Kimwipe Paper. . Specimen Was Stored in a
Desiccator for Five Days

Energy dispersive X-ray (EDX) spectra are shown in Figures 10 through 12. From the globular particles as can be seen in the SEM pictures (Figures 8 through 12), Figures 10 and 11 were obtained and, from the elongated-particle background, Figure 12 was obtained.

Figures 13 through 17 are the ESCA spectra obtained from the deposit formed at (0000). Figure 13 is the survey scan and the others are single element scans for Mg, Fe, and Ca.

Fourier transform infrared (FTIR) spectra were studied from the deposits formed at (0000) for 2 hours and 6 hours in order to obtain the chemical information for the anionic species in the deposits (Figure 18).

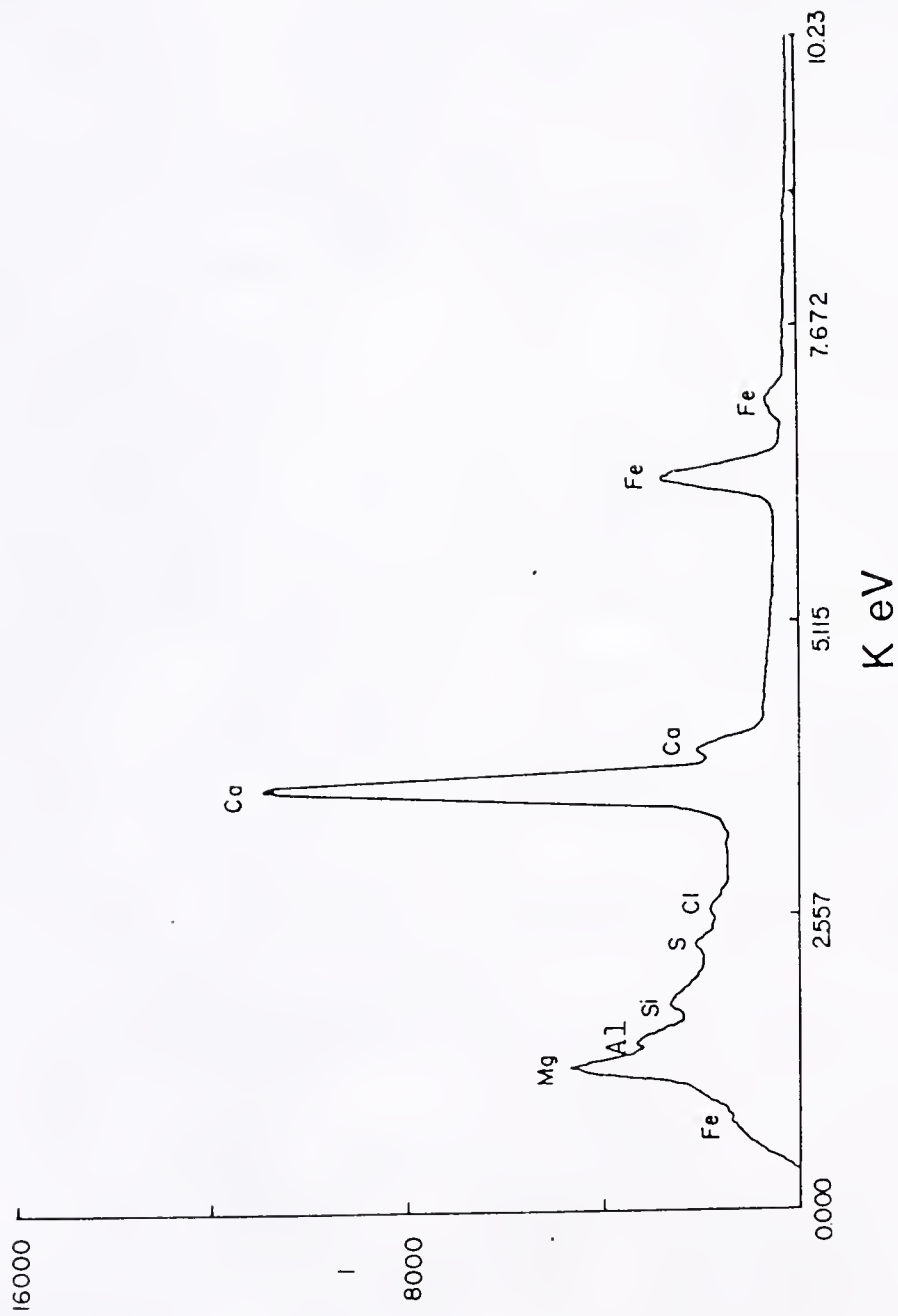


Figure 10 Energy Dispersive X-ray Spectra of Globular Particle

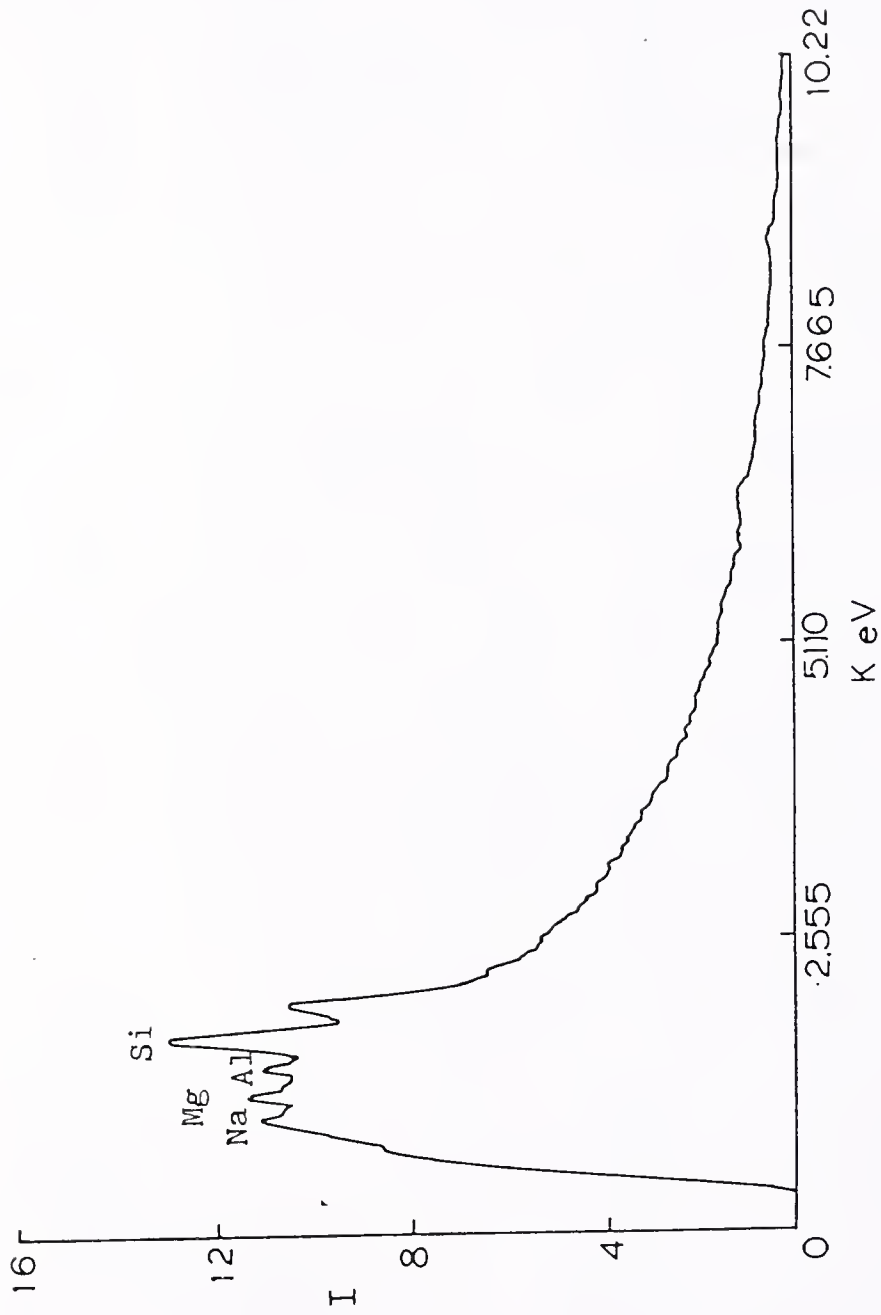


Figure 11 Energy Dispersive X-ray Spectra of Globular Particles

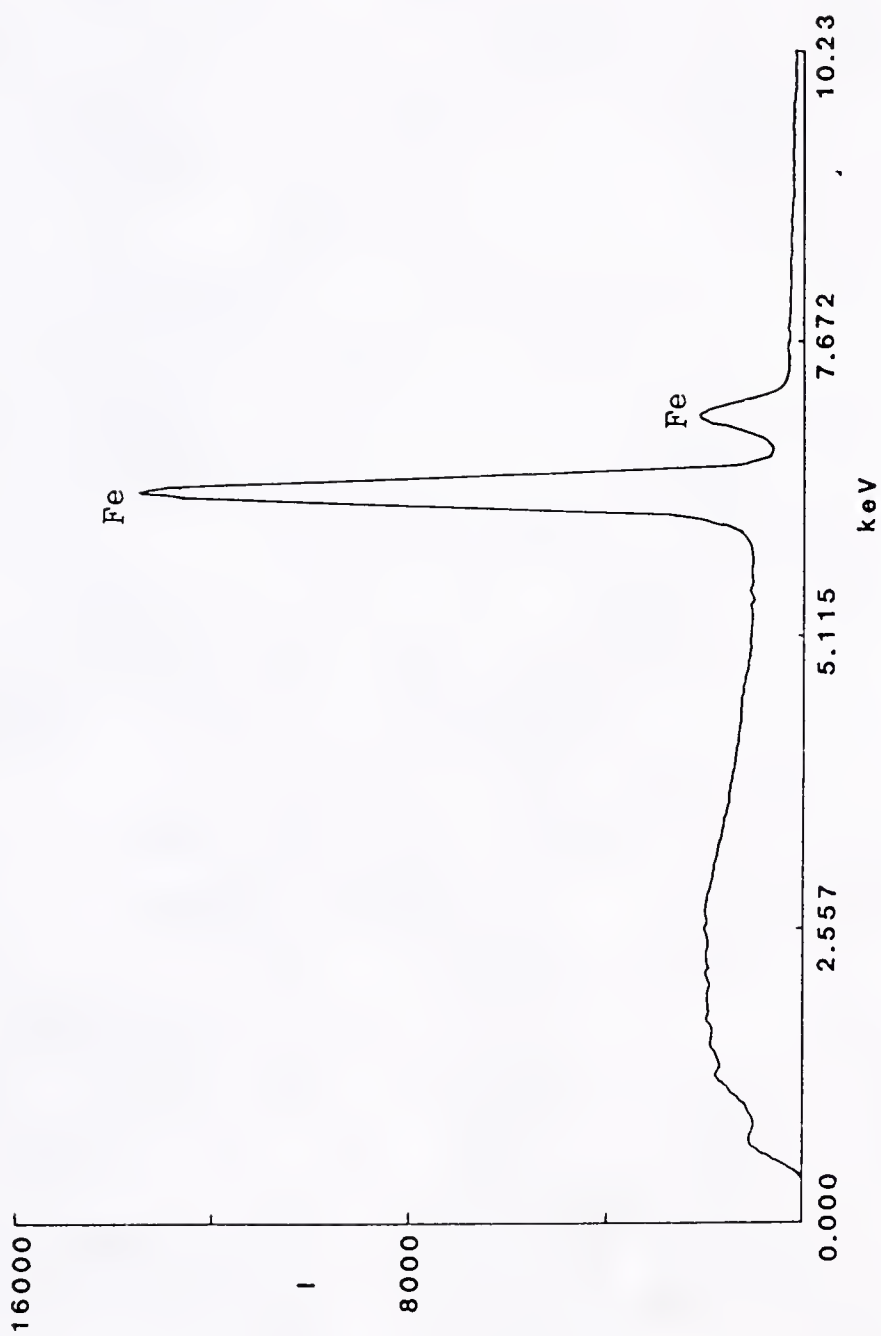


Figure 12 Energy Dispersive X-ray Spectra of Background Layer

RUN:-DVT6 / 20-APR-83 REG: 1.001 ST:0.30 #C:4000 #SW: 5 DWELL: 0.100
BACKGROUND : 108

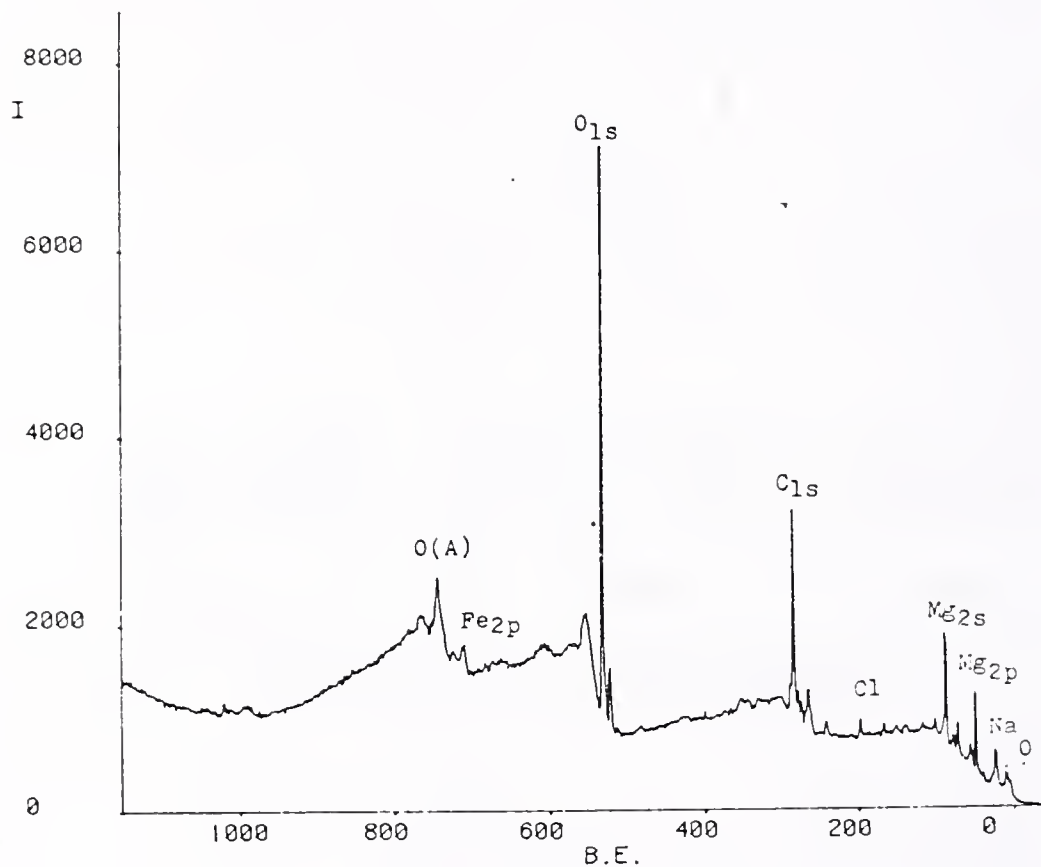


Figure 13 ESCA Survey Scan of Deposit Formed at (0000)

RUN:-CS21 / 16-NOV-83 REG: 2.001 ST:0.10 #C: 400 #SW: 50 DWELL: 0.200
BACKGROUND : 13057

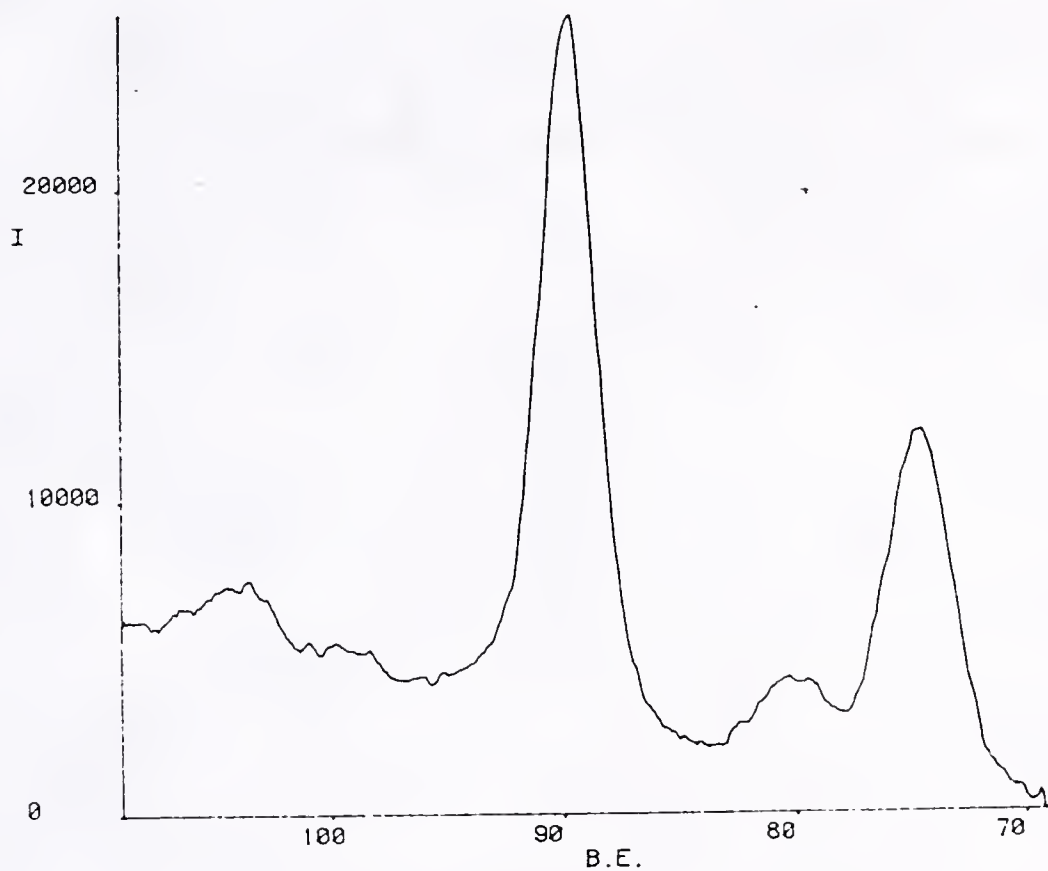


Figure 14 ESCA Mg Scan of Deposit Formed at (0000)

16-NOV-83 REG: 3.001 ST:0.10 #C: 400 #SW: 50 DWELL: 0.200
BACKGROUND : 27566

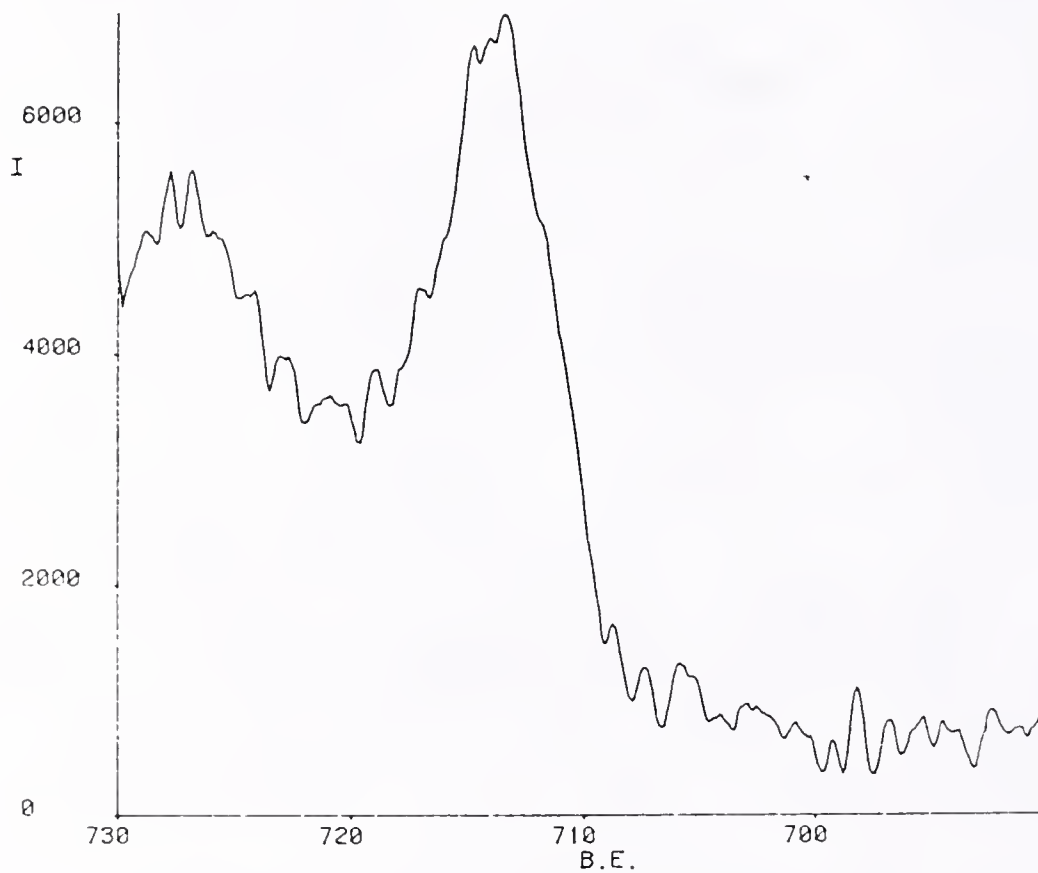


Figure 15 ESCA Fe Scan of Deposit Formed at (0000)

RUN:-CS21 / 16-NOV-83 REG: 1.001 ST:0.10 #C: 400 #SW: 50 DWELL: 0.200
BACKGROUND : 21344

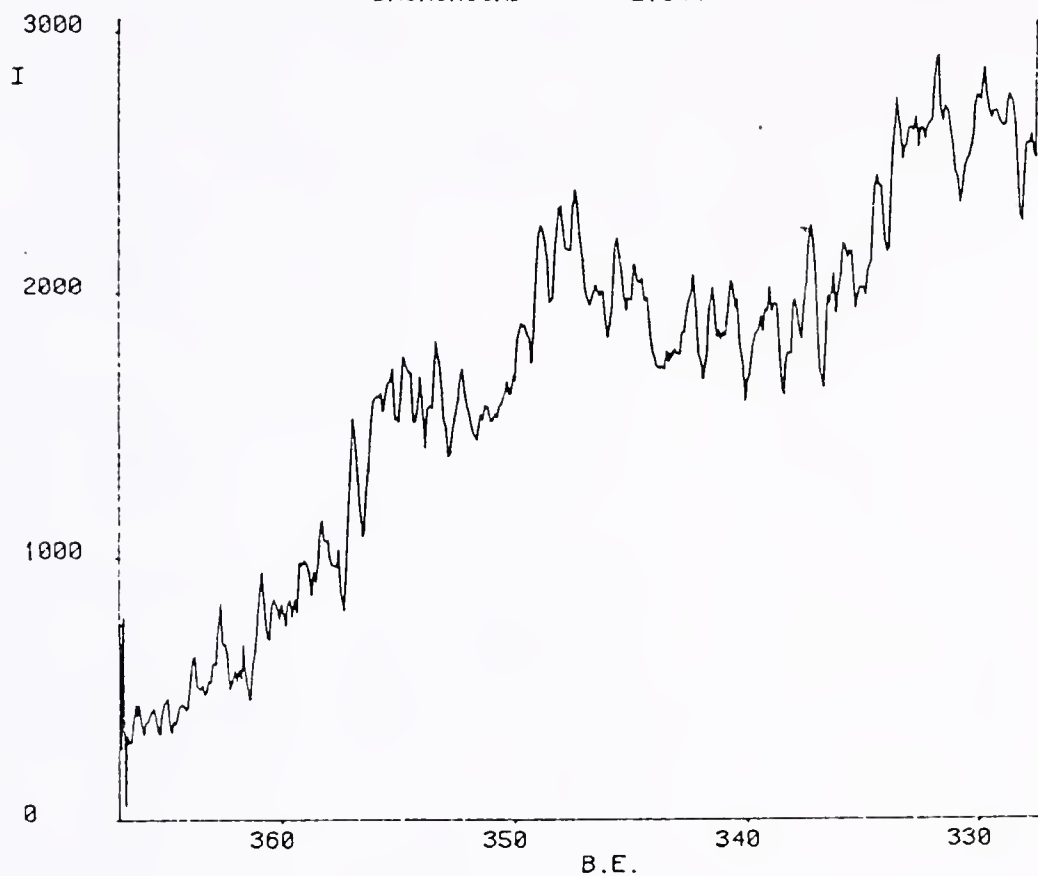


Figure 16 ESCA Ca Scan (Low Resolution) of Deposit Formed
at (0000)

RUN:-BH20 / 25-JUN-84 REG: 2.001 ST:0.10 #C: 400 #SW:100 DWELL: 0.200
BACKGROUND : 13448

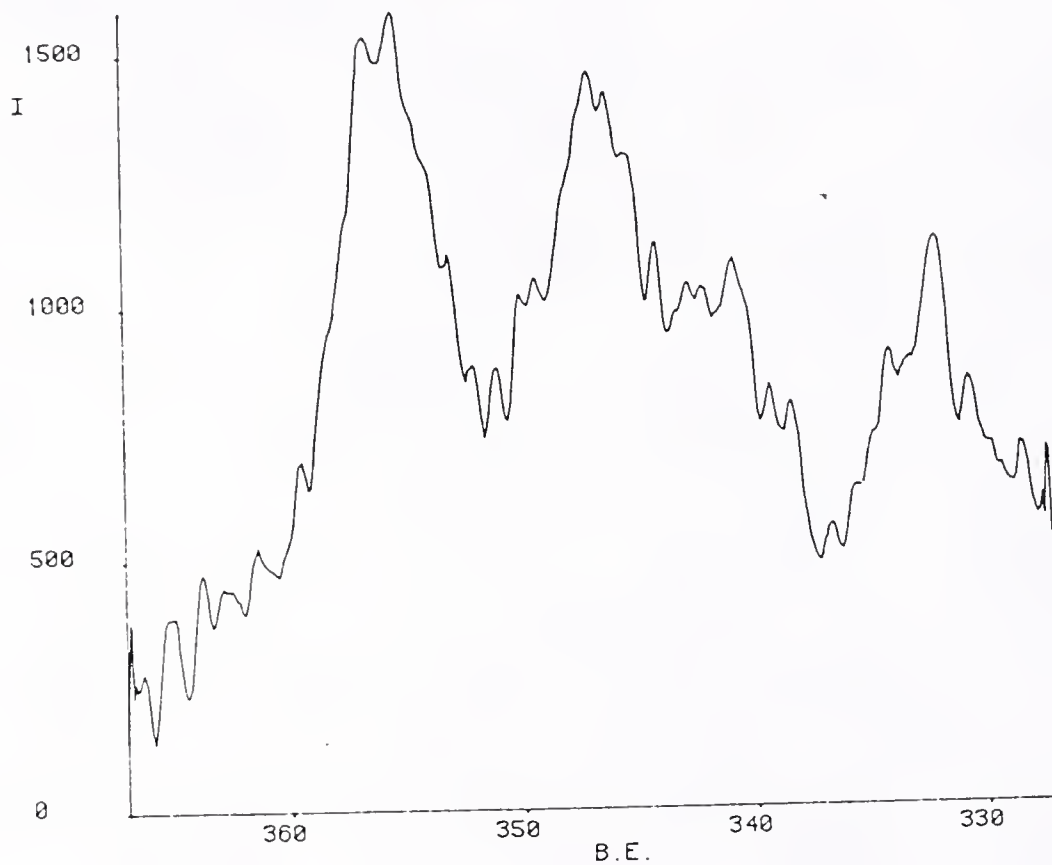


Figure 17 ESCA Ca Scan (Medium Resolution) of Deposit
Formed at (0000)

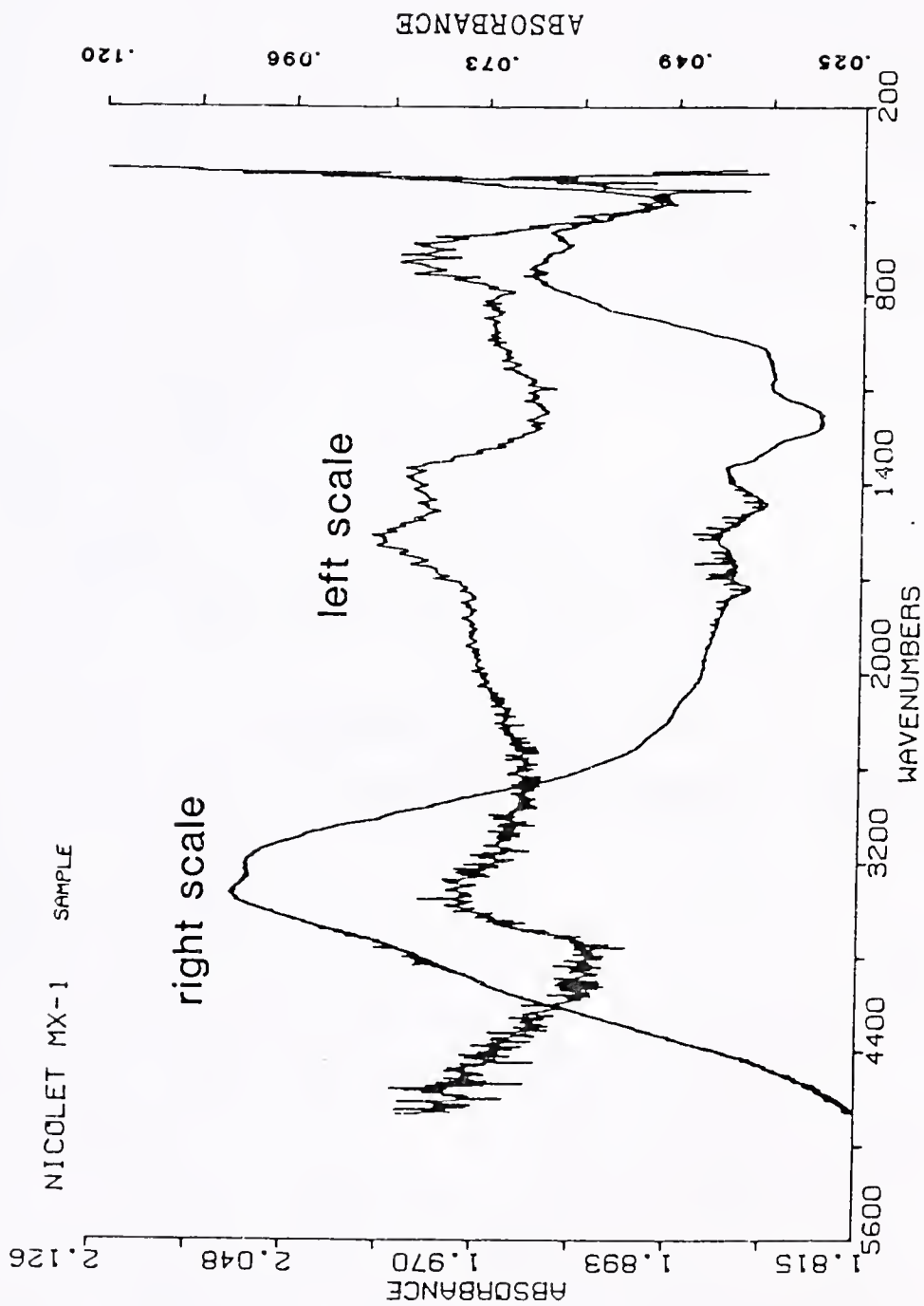


Figure 18 FTIR Spectra of Deposit Formed at (0000) for 2 (right scale) and 6 (left scale) hours

CHAPTER 5 DISCUSSION

5.1 Discussion of Background

5.1.1 Rotating Disc Electrode

When an electrode of a flat disk shape (Figure 19) rotates, the solution near the electrode follows the motion of the electrode because of the viscous nature of the liquid. As the distance from the electrode increases, the movement of the solution starts to deviate from that of the electrode. The three dimensional movement of the solution is shown in Figure 19. Because the perpendicular motion decreases as the distance from electrode surface decreases, at certain point, the perpendicular motion becomes almost zero and convection does not contribute to mass transport any more. Therefore, mass transport is solely driven by concentration gradient, i.e., diffusion. The term "diffusion layer" is defined as the solution layer from zero to this distance from electrode surface. The presence of a diffusion layer is not limited to a rotating disc electrode system. Every electrochemical system inherently containing a solid-solution interface can have this phenomenon depending upon reaction kinetics. Therefore, by employing rotating disc electrode system, mass transport across the diffusion layer can be successfully controlled.

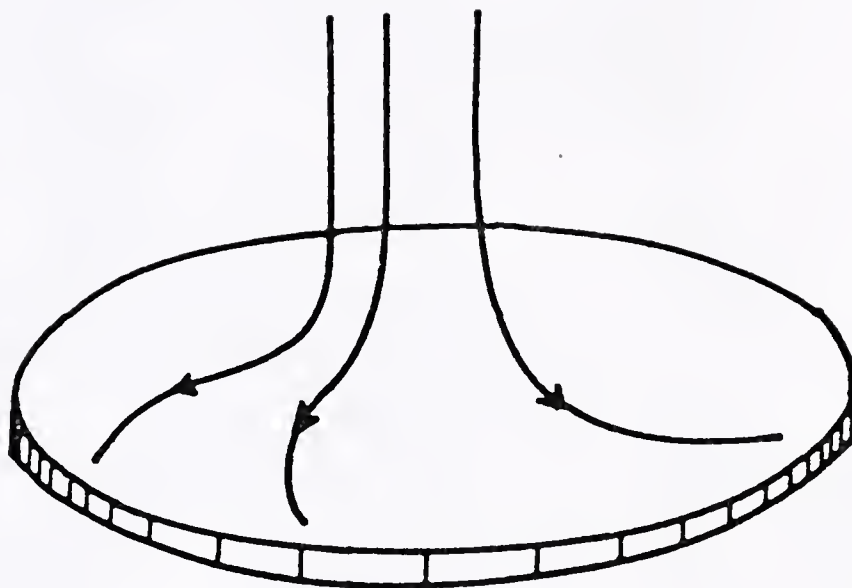


Figure 19 Three-Dimensional Flow of Liquid Near Rotating Disc Electrode

5.1.2 Effects of Parameters

The factorial design technique is well established and detailed information can be found in experimental statistics books (79,80). The magnitude of an effect can be interpreted in this way: when a parameter is changed from level 0 to level 1, average current increases by that amount. Therefore, a positive effect indicates increase in current and a negative effect indicates decrease in current. Detailed information on the procedure of calculation can be found in Appendix 2.

In the case of "with deposit" (Table 7), temperature has the smallest effect on current whereas pH has the largest effect. But these effects have to be carefully interpreted. A parameter has two different natures of influence; one on the rate of electrochemical cathodic reactions taking place on electrode surface and the other on the formation of deposit which effectively retards the passage of current through the deposit. The variation of a parameter will inevitably have these two aspects. Therefore, the effects reflect both, cathodic reaction and deposit formation. In order to study the influence on deposit formation only, the influence on the cathodic reaction has to be subtracted from the total influence. For this purpose, a solution which did not contain deposit forming elements (deposit-free solution) such as Ca^{++} , Mg^{++} and Sr^{++} was used. Because deposits did not form on metal surfaces, the variation of a parameter had an influence on the

cathodic reaction only. Therefore, the figures under the heading of "without deposit" in Table 7 represent the influence (or effect) of the four parameters on the rate of electrochemical reactions only. Unfortunately, the right column ("without deposit") can not be directly subtracted from the left column ("with deposit"), even though the former represents the influence on reaction rate and the latter represents the influence on both reaction rate and deposit formation. Because the original electrode surface area did not change in the "without deposit" experiments whereas the area was reduced in the "with deposit" experiments, direct subtraction should not be used unless the "without deposit" effects (or currents) are compensated for the change in the surface area. However, a "without deposit" effect can be compared to the corresponding "with deposit" effect in order to evaluate the influence of the parameter on deposit formation.

5.1.3 Ratio of Currents at Two Different Rotation Speeds

When an electrochemical reaction is diffusion controlled, the diffusion limited current i can be expressed as (81,82)

$$i = m \frac{DC}{\delta} \quad [1]$$

where m = constant

D = diffusion coefficient

C = bulk concentration of the rate limiting species

δ = diffusion layer thickness.

Also, diffusion layer thickness δ can be expressed as
(81,82)

$$\delta = s D^{1/3} \nu^{1/6} \omega^{-1/2} \quad [2]$$

where s = constant

ν = kinematic viscosity

ω = rotation speed.

Substituting [2] into [1]

$$i = \frac{m}{s} \frac{D^{2/3} \omega^{1/2} C}{\nu^{1/6}} \quad [3]$$

It can be seen from [3] that a diffusion limited current is proportional to the square root of the electrode rotation speed (ω). The linear relationship between cathodic current and $\omega^{1/2}$ is shown in Figure 20, based upon which it can be said that the electrochemical reaction at -0.8V is diffusion controlled. The ASTM standard artificial seawater does not have any other reducible species at the potential used but dissolved oxygen. The presence of the plateau in the polarization curves both in the artificial seawater and in the deposit-free solution confirms that oxygen reduction

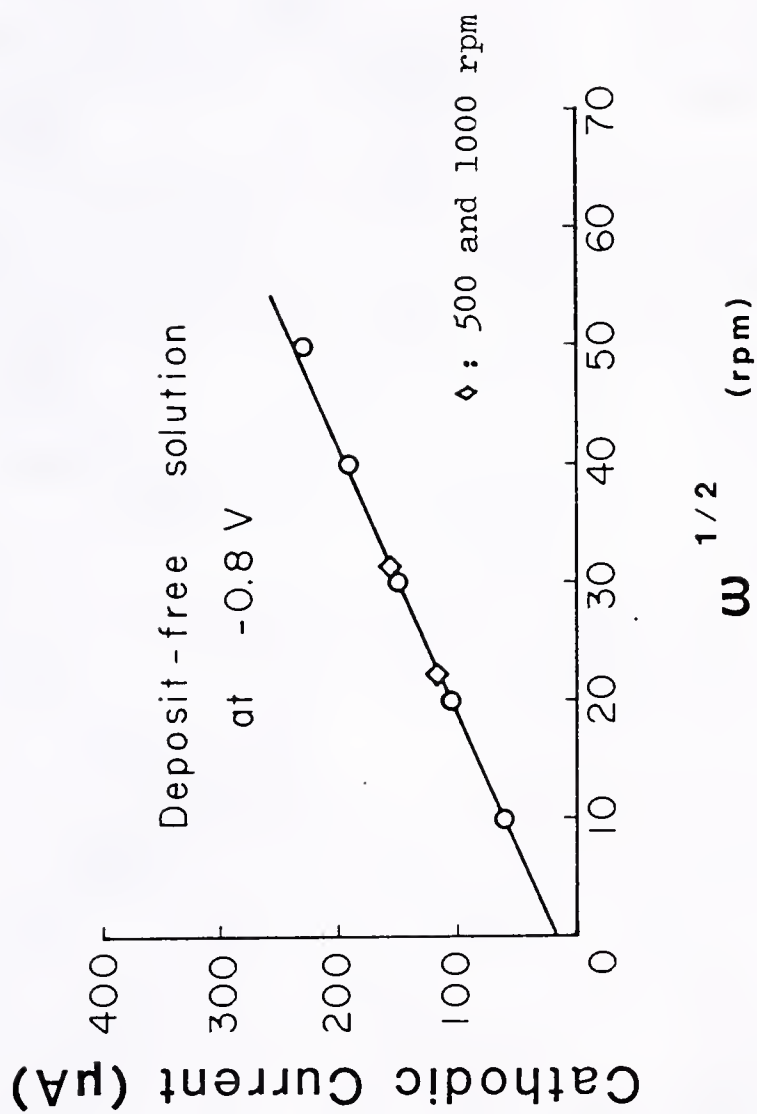


Figure 20 Cathodic Current vs. (Electrode Rotation Speed)^{1/2}

reaction is diffusion controlled at -0.8V and the more negative potentials (Figure 21), even with deposits formed on the electrode surface.

The dependence of oxygen reduction current on electrode rotation speed is, as shown in [2], due to the fact that increase of rotation speed results in the decrease in diffusion layer thickness which, in turn, increases the arrival rate of dissolved oxygen. According to [3], the current should increase by the factor of $\sqrt{2}$ when the rotation speed is raised from 500 rpm to 1000 rpm.

Because it is inconceivable that electrons leave metallic electrode and become hydrated in solution and because it is equally inconceivable that calcareous deposits, which can be characterized as ionic compounds, conduct electrons, all electrochemical reactions must take place on electrode surface. Though the deposits can not conduct electrons, they can conduct electricity through the water which the deposits contain; trapped or adsorbed. Insofar as the deposits contain water, oxygen molecules can travel through the water in the deposit leading to any oxygen current; hydrogen current also becomes a factor at more negative applied potentials. As the deposit increases its physical coverage of electrode surface, the current path from the bare metal to the bulk solution loses its role as the major conduction path and the current path from the metal surface through the solution contained in the pores and adsorbed deposit particles becomes the more important

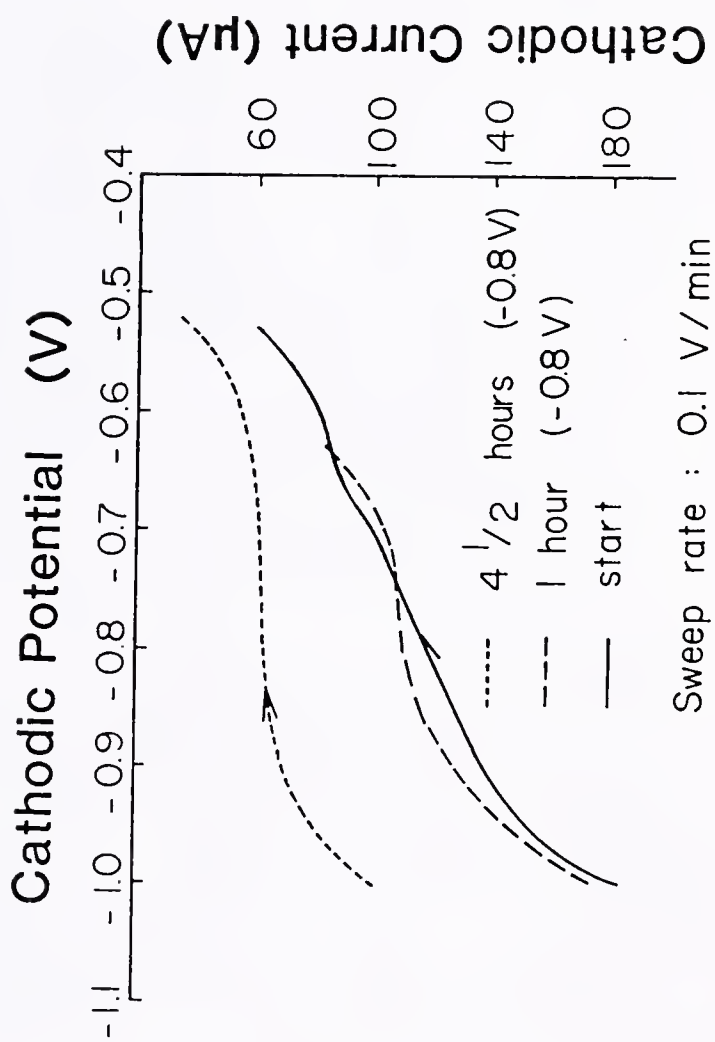


Figure 21 Cathodic Polarization Curves. The Top Curve Was Obtained After Deposit Was Formed for 4 1/2 Hours and the Bottom Two Curves Were Obtained in Deposit-Free Solution. Electrode Rotation Speed Was 500 rpm

conduction path. Also, as deposits grow in thickness, mass transport across the deposits becomes more difficult and mass transport across diffusion layer, whose thickness can be calculated from the equation [2], gradually loses its effect on total mass transport. Therefore, as deposit grows, increase in rotation speed, even though it decreases the original diffusion layer thickness proportional to the inverse one-half power of rotation speed, does not accelerate oxygen diffusion through the deposit as much as can be predicted from [2] and the amount of current increase will become smaller and smaller. As a result, the $\sqrt{2}$ relationship between the current at 1000 rpm (i_{1000}) and the current at 500 rpm (i_{500}) predicted from [3] will fail and the ratio, i_{1000}/i_{500} will decrease to approach unity at which mass transport across the deposit becomes rate controlling step. Therefore, observation of decrease in i_{1000}/i_{500} against time will be able to show the development process of deposit on the electrode surface (Figure 1).

5.2 Discussion of Influence of Parameters on Deposit Formation

5.2.1 pH

The effects of pH of Table 7 are shown schematically in Figure 22, "without deposit" and "with deposit." "Without deposit," the current at level 1 was almost the same as that at level 2. In other words, variation of bulk pH had little influence on the rate of cathodic reaction which was measured in terms of current, though $[\text{OH}^-]$ is in the

pH effect : $-0.1 \rightarrow 30.1 \mu\text{A}$

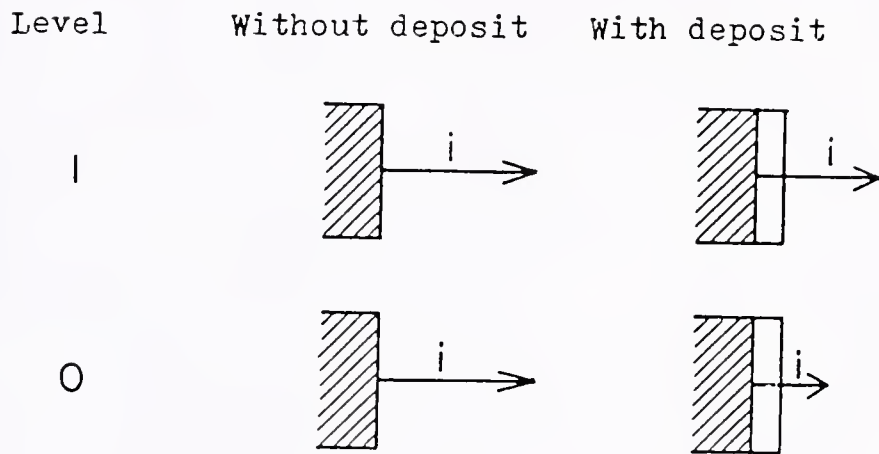
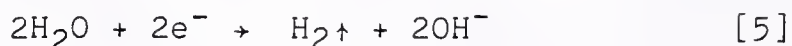
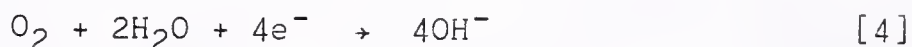


Figure 22 Schematic Presentation of the pH Effects

reaction path for both oxygen reduction reaction and hydrogen evolution reaction.



The fact that the cathodic current is mainly comprised of hydrogen evolution current and oxygen reduction current allows us to interpret the measured pH effect ("without deposit") as the sum of the two corresponding parts.

As was discussed in 5.1.3, the oxygen reduction reaction is diffusion controlled at the potentials of this study. Therefore, variation in pH should not have any influence on oxygen current, though $[\text{OH}^-]$ is in the reaction path of oxygen reduction reaction [4].

In contrast, hydrogen evolution is kinetically controlled. Therefore, decrease in pH from 8.3 (level 0) to 7.9 (level 1) is expected to yield a slight increase in hydrogen evolution current. The amount of hydrogen current increase can be calculated from the relationship between current and overpotential. For hydrogen evolution reaction, equilibrium potential is related to pH in the following equation:

$$E = E^0 - \frac{2.303RT}{F} \text{pH} \quad [6]$$

where E is the equilibrium potential and the other symbols are conventional. As pH decreases from 8.3 to 7.9, at

$$T = 23^{\circ}\text{C},$$

$$\Delta E = E_1 - E_0 = 0.023\text{V}$$

where the subscripts are the two levels of pH. From the following equation between current and overpotential, for cathodic reaction:

$$\eta = B - \frac{2.303}{\alpha F} RT \log i \quad [7]$$

where η is the overpotential and the other symbols are conventional. Therefore,

$$\eta_1 - \eta_0 = \frac{2.303}{\alpha F} RT \log \frac{i_1}{i_0} \quad [8]$$

where the subscripts are the two levels of pH. From the slope of the cathodic polarization curve (Figure 23),

$$\frac{2.303}{\alpha F} RT = 0.18\text{V} \quad [9]$$

at $T = 23^{\circ}\text{C}$. From above calculation, $\eta_1 - \eta_0 = -0.023\text{V}$. Therefore, from [8], $i_1 = 1.34 i_0$. Because the average current increase as cathodic potential increases can be regarded as an average hydrogen current,

$$\Delta i = i_1 - i_0 = 0.34 i_0 \approx 7 \mu\text{A}$$

can be obtained. The effect of $22 \mu\text{A}$, the average hydrogen current, was used for i_0 . Effect is calculated from 16

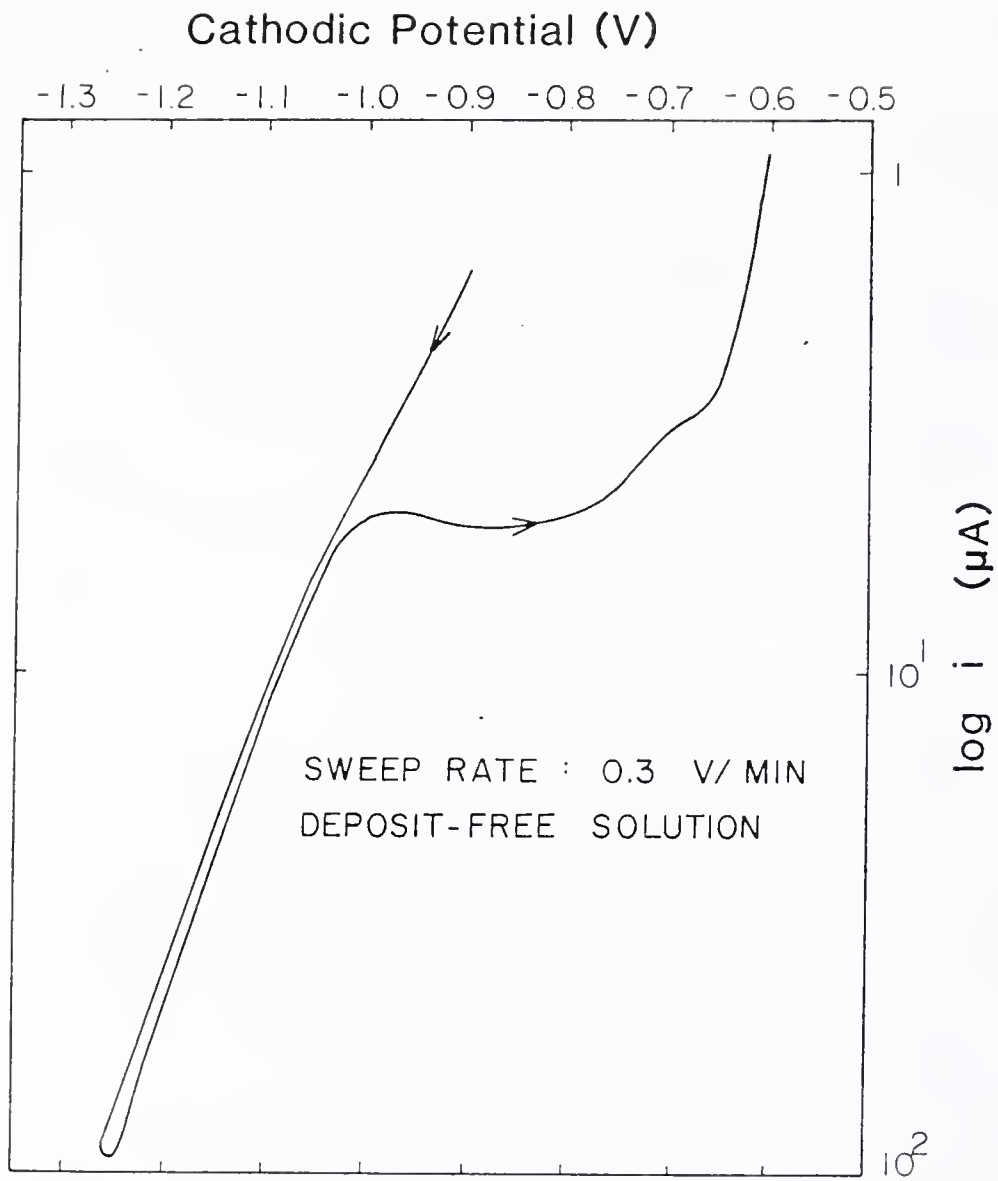


Figure 23 Cathodic Polarization Curve

different experimental conditions among which 8 have oxygen current only and the other 8 have both oxygen and hydrogen currents. Therefore, pH effect, which is the average current increase with pH variation from level 0 to level 1, is half of the sum of the influences on oxygen current (zero expected, theoretically) and on hydrogen current ($7 \mu\text{A}$ expected, theoretically). So the measured pH effect of $-0.1 \mu\text{A}$ "without deposit" can be theoretically explained by the preceding discussion.

This almost zero pH effect changed to $+30.1 \mu\text{A}$ when deposit was introduced into the system. And i_1 became larger than i_0 ("with deposit" in Figure 22). If the two deposits formed at the two different pH values are identical in their current blocking capability, i_1 has to be almost the same as i_0 ("with deposit" in Figure 22), which is suggested by the negligible difference in currents "without deposit." The fact that i_1 became larger than i_0 ("with deposit" in Figure 22) allows us to draw the conclusion that the deposit formed at level 1 is poorer than the deposit formed at level 0 in terms of current blocking capability.

The effect of pH decrease from 8.3 (level 0) to 7.9 (level 1) on the formation of deposit is obvious. The pH at the immediate vicinity of electrode surface (surface pH) is much higher than bulk pH and such a small increase or decrease in bulk pH may not be substantial in increasing or decreasing surface pH. However, if surface pH does not change with bulk pH, the OH^- concentration gradient across

the diffusion layer will be greater at lower bulk pH and OH^- diffusion rate will be accelerated. To maintain same surface pH at a lower bulk pH as at a higher bulk pH, OH^- generation rate at a lower bulk pH must be greater to keep up the increased diffusion rate. However, the nil pH effect on the rate of cathodic reaction(s) indicates that OH^- generation is not accelerated at a lower bulk pH. As a result, surface pH decreases as bulk pH decreases. As was discussed in Section 2.1, the deposit forming reactions are driven by high surface pH near metal surface. The decrease in surface pH will decrease the rates of the deposit forming reactions. Therefore, at a lower bulk pH, rates of the deposit forming reactions decrease and, in the same period of time, the quantity of the deposit will be smaller leading to a lower degree of protection, in terms of cathodic current decrease.

The lower degree of protection of the electrode surface by the deposit at the low bulk pH, in terms of the reduction of cathodic current, is also indicated by the large difference between the effective surface coverages (ESC) of the two pH subgroups (Table 8). Because ESC is the percentage of current decrease from the base metal condition, the small percentage at the low bulk pH (level 1) suggests that the deposit formed at the low bulk pH is poorer than the deposit formed at the high bulk pH. This can be explained by the low deposition rate, as was discussed previously. It can also be noted that the largest difference in ESC was between

the two pH subgroups, indicating that the variation of solution pH has the most significant influence on deposit formation under the experimental conditions employed for this study.

This conclusion is also supported by Figure 1. Because the decay of the ratio i_{1000}/i_{500} was due to the fact that the deposit on the metal surface controls the transportation of oxygen, the slow decay of the ratio at (0010), (low pH), compared to (0000), (high pH), indicates that the deposit formed at the low bulk pH is not as effective as the deposit formed at the high bulk pH in its capability to control the transportation of oxygen. This can be explained by the low deposition rate at the low bulk pH.

5.2.2 Temperature

The T effects of Table 7 are shown schematically in Figure 24, "without deposit" and "with deposit." "Without deposit," the current at level 1 (16°C) was smaller than the current at level 0 (23°C). At low temperatures, more oxygen is dissolved and oxygen current should increase, as a result. However, there are compensatory effects which occur as temperature is lowered: increase in diffusion layer thickness and decrease in diffusion coefficient. Semi-quantitative predictions can be made using well established equations that apply to diffusion limited reactions in rotating disc systems. The fact that oxygen reduction reaction is diffusion limited was previously discussed.

T effect : $-5.4 \rightarrow 9.6 \text{ } \mu\text{A}$

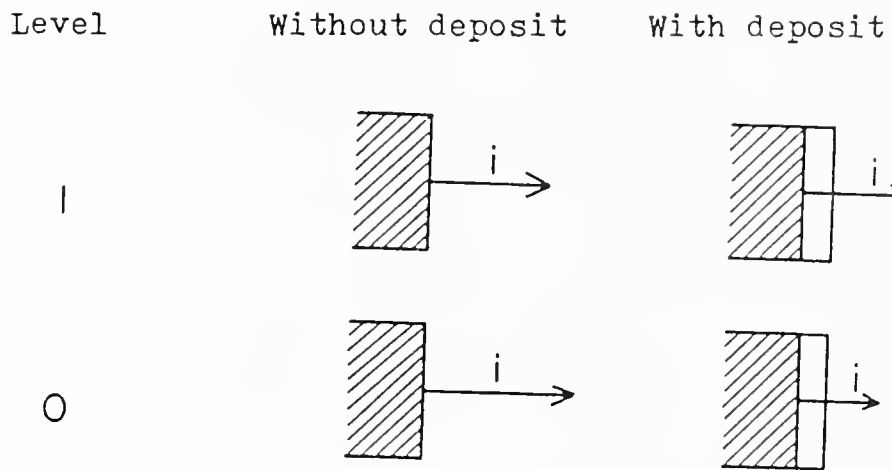


Figure 24 Schematic Presentation of the T Effects

Based upon the diffusion limited oxygen current, the negative effect of temperature will be discussed.

The dependence of diffusion layer thickness on temperature can be expressed by (83)

$$\delta = p \frac{T}{i} C \quad [10]$$

where p is a constant. Equation [3] is

$$i = \frac{m}{s} \frac{D^{2/3} \omega^{1/2} C}{\nu^{1/6}} \quad [3]$$

Substituting [3] to [10],

$$\delta = \frac{ps}{m} \frac{T \nu^{1/6}}{D^{2/3} \omega^{1/2}} \quad [11]$$

To compare the thickness at level 0 (δ_0) to that at level 1 (δ_1) where ω is constant,

$$\frac{\delta_1}{\delta_0} = \left(\frac{T_1}{T_0} \right) \left(\frac{\nu_1}{\nu_0} \right)^{1/6} \left(\frac{D_0}{D_1} \right)^{2/3} \quad [12]$$

Kinematic viscosity ν is related to dynamic viscosity μ by

$$\nu = \frac{\mu}{\rho}$$

where ρ = density. Neglecting the small difference in ρ between 16°C and 23°C,

$$\frac{\nu_1}{\nu_0} = \frac{\mu_1}{\mu_0} \quad .$$

Using the interpolated data from Table 10, $\mu_1 = 0.660$ and $\mu_0 = 0.559$. Therefore,

$$\frac{\nu_1}{\nu_0} = \frac{0.660}{0.559}$$

Glasstone (57) reported that diffusion coefficient of most substances in aqueous solutions is experimentally found to increase about 2.5% per degree ($^{\circ}\text{C}$), because of the increase in viscosity. In fact, the increase in viscosity is of the same magnitude. From the relationship,

$$D_0 = 1.175 D_1$$

can be calculated. Therefore, from [12],

$$\frac{\delta_1}{\delta_0} = \frac{289}{296} \left(\frac{0.660}{0.559} \right)^{1/6} \left(\frac{1.175 D_1}{D_1} \right)^{2/3} = 1.12$$

From equation [1],

$$\frac{i_1}{i_0} = \frac{D_1}{D_0} \frac{\delta_0}{\delta_1} \frac{C_1}{C_0}$$

where superscripts are used same as elsewhere. Using the oxygen solubility of 8.0 and 7.0 mg/l at 16 and 23°C , respectively, in water containing 20 gm/l of chloride (84),

$$\frac{i_1}{i_0} = \frac{D_1}{1.175 D_1} \frac{\delta_0}{1.12 \delta_0} \frac{8.0}{7.0} = 0.87$$

Table 10 Relative viscosity of seawater

<u>Temp (°C)</u>	<u>Relative viscosity*</u>
0	1.056
5	0.891
10	0.772
15	0.675
20	0.599
25	0.533
30	0.481

Note: From Handbook of Marine Science (2)

* Relative viscosity = $\frac{\text{viscosity of seawater}}{\text{viscosity of pure water at } 0^{\circ}\text{C (1.787 centipose)}}$

Therefore, oxygen current is expected to decrease by 13% with temperature decrease from 23 to 16°C.

The direction of the change of hydrogen current will be a negative increase because hydrogen evolution reaction is activation controlled. Cathodic current is exponentially related to temperature in the following equation:

$$i = A i_{ex} \exp \left[-\frac{\alpha F}{RT} \eta \right] \quad [13]$$

where A = surface area

i_{ex} = exchange current density

α = symmetry coefficient

F = Faraday constant

R = gas constant

T = temperature

η = overpotential.

Lack of information about the dependence of i_{ex} and α on temperature variation does not allow good approximation. Theoretically expected temperature effect is one half of the sum of temperature influences on oxygen current and on hydrogen current. Because the temperature influence on oxygen current is about 13% decrease or about -12 μ A, its influence on hydrogen current should be relatively small to explain the measured T effect of -5.4 μ A.

This negative T effect was changed to a positive T effect when deposit was introduced into the system. And i_1 became larger than i_0 ("with deposit" of Figure 24). If the

two deposits formed at the two different temperatures are identical in their current reducing capability, i_1 has to be smaller than i_0 ("with deposit" of Figure 24), which is suggested by the relationship between currents "without deposit." The fact that i_1 became larger than i_0 ("with deposit" of Figure 24) allows us to draw the conclusion that the deposit formed at level 1 is poorer than the deposit formed at level 0 in terms of current blocking capability. In other words, the lower temperature (16°C) caused the deposit to become less efficient in obstructing current flow through the deposit than at the higher temperature (23°C).

The effect of temperature on formation of calcareous deposits is believed to be bifold. As temperature decreases, the solubility products of both $\text{Mg}(\text{OH})_2$ and CaCO_3 increase (Table 4) and the deposition rate of these compounds is expected to decrease. Also, a decrease in temperature may cause a decrease in the rate of the deposition reaction. In general, a chemical reaction can be expressed in an Arrhenius type relationship between reaction rate and temperature like the following:

$$\text{Rate} = A \exp \left(- \frac{Q}{RT} \right) \quad [13]$$

where A = rate constant

Q = activation energy

R = gas constant

T = temperature.

Therefore, for the deposition of calcareous scales, an exponential decrease in the rate with temperature decrease may be substantial in the process of calcareous deposit formation.

The low deposition rate at low temperatures caused by the increase in the solubility products of both $\text{Mg}(\text{OH})_2$ and CaCO_3 , and also possibly caused by the thermal activation mechanism yields a less protective deposit. This can also be shown in Table 8. Because effective surface coverage (ESC) is the percentage of current decrease from the bare metal condition, the smaller percentage at the low temperature (level 1) suggests that the deposit formed at the low temperature is poorer than the deposit formed at the high temperature in its current reducing capability. This can be explained by the low deposition rate at the low temperature, as was discussed previously. It can also be noted that the difference in ESC between the two temperature subgroups is the second largest, indicating that the variation of temperature has the second most significant influence on deposit formation under the experimental conditions employed for this study. This can also be drawn from Figure 1. Because the decay of the ratio, i_{1000}/i_{500} was caused by the development of the calcareous deposit which functions as a barrier to the transportation of oxygen, the slow decay shown by the low temperature curve, (0001), indicates that the deposit is not as effective as the deposit at the high temperature (0000), with respect to

capability to slow down the oxygen diffusion rate through the deposit. The reduced deposition rate at the low temperature results in the smaller amount of the deposit formed on the metal surface and thus the lower degree of protection in terms of cathodic current decrease.

5.2.3 Potential

The potential effects (E effects) of Table 7 are schematically presented in Figure 25. Potential (E) effect did not vary significantly from "with deposit" experiments to "without deposit" experiments. Potential effect can be viewed as the average increase in cathodic current through the 16 different experimental conditions as potential is raised from -0.8V to -1.0V. Because oxygen current is limited by the diffusion of oxygen molecules onto electrode surface, increase in cathodic potential has little influence on it. In Figure 4 is shown a typical polarization curve with deposit formed on electrode surface. Oxygen current does not increase in the plateau region. Therefore, the increase in current (E effect) is believed to be due to hydrogen current. E effect of 21.9 μA "without deposit" does not significantly decrease as deposit is formed on electrode surface as shown by 21.2 μA "with deposit." From this, the following can be suggested:

Though formation of deposit effectively decreases oxygen current by its nature of transportation barrier, hydrogen evolution reaction does not need transport of reacting species and as far as the

E effect : $21.9 \rightarrow 21.2 \mu\text{A}$

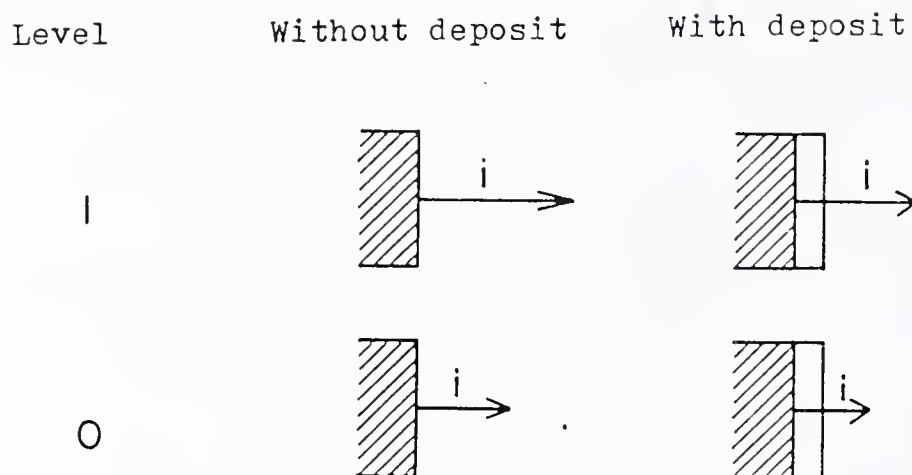


Figure 25 Schematic Presentation of the E Effects

deposit has enough water to be hydrolyzed on electrode surface, hydrogen current is little affected by the presence of deposit. Therefore, initially oxygen current comprises most of the cathodic current but, in later stage of deposit formation, hydrogen current will become significant.

To confirm this suggestion, the experimental condition of selected. Deposit was formed at -1.0V. Intermittently, potential was changed to -0.8V. From the previous discussion, hydrogen current can be defined as

$$i_{H_2} = i_{-1.0} - i_{-0.8}$$

where $i_{-1.0}$ = current at -1.0V

$i_{-0.8}$ = current at -0.8V.

Also, hydrogen current percentage in total hydrogen current was calculated as $(i_{H_2}/i_{-1.0}) \times 100$. Figure 2 is the variation of the hydrogen current and its percentage with time. Hydrogen current percentage increased with time. Hydrogen current did not decrease initially though its percentage increased rapidly. After several hours, hydrogen current started to decrease and its decay rate became smaller at longer period of time. Taking the first data point as reference current, about 20% of hydrogen current has decreased whereas oxygen current has decreased by more

than 60% during the same period. Oxygen current was calculated by subtracting hydrogen current ($i_{-1.0} - i_{-0.8}$) from total current. This is direct evidence that the deposit that functions as a diffusion barrier for dissolved oxygen transportation from solution to metal surface is not as effective in controlling hydrogen evolution reaction; it is believed to be due to the presence of solution in deposit.

The presence of water in the deposit can be explained by the nucleation and growth phenomena of precipitates from supersaturated solutions. Precipitation from concentrated (supersaturated) solution inevitably goes through the procedure of nucleation and growth. When the solubility of a compound is exceeded, anions and cations of several angstrom units cling together forming a crystal lattice. As the particle size surpasses critical size for further growth, stable nuclei are formed. As the nuclei grow in size, a colloidal state is reached in which particles are submicron in size. If surface charge is significant, colloidal state is stabilized and no further growth in particle size can be achieved. Reports can be found on positive surface charge of $\text{Mg}(\text{OH})_2$ and negative surface charge of CaCO_3 in alkaline solutions of pH up to 10 (85-87). It may be possible that the positively charged $\text{Mg}(\text{OH})_2$ colloidal particles are preferentially attracted to electrode surface whereas negatively charged CaCO_3 particles are repelled. However, the solutions used for these studies have large amount of anions and cations and it is very

unlikely that such a stable colloidal state can be maintained throughout the process of deposit formation. Fine crystals of micron size grow from the colloidal state. Depending upon conditions, these micron size particles form large particles greater than 10 μm in size which can be easily filtered with coarse filter paper. SEM photographs (Figures 4 through 8) show such large particles are not formed. Therefore, particles are thought to be present as fine crystals. Fine crystals, when they precipitate, take up large amount of impurities in several different ways such as coprecipitation, surface adsorption, occlusion, etc. compared to coarse crystals. Occlusion is the type of contamination in which impurities are trapped within crystals or between crystals. Unless the whole precipitate is one single crystal, it is inevitable that the voids between particles provide space for mother liquor entrapment. There are other sources of the presence of water in water-born precipitates (88). Adsorbed water on particle surface, water of hydration, inclusions within crystals and superficial adherent water are examples of them. Water present in deposit provides an electrical conduction path. When samples were kept in a desiccator for several days waiting for analysis, small pits were found to have developed on electrode surface, evenly distributed over the surface. Figure 9 is SEM photograph taken from one of these observations. When deposit was removed from electrode surface immediately after deposition experiment, pits were

not found. Therefore, the pits were formed during the storage in a desiccator due to the presence of water. The difference in effective surface coverage (Table 8) between the two main groups can be explained based upon the above finding that hydrogen current does not decrease significantly because of the presence of water in the deposit. As was discussed previously, hydrogen current is not so much affected by deposit as oxygen current. Because effective surface coverage was obtained from the formula,

$$\text{effective surface coverage} = \frac{i_{\text{without deposit}} - i_{\text{with deposit}}}{i_{\text{without deposit}}}$$

presence of almost the same amount of hydrogen current in $i_{\text{with deposit}}$ always yields a lower result. Because of this, the lower ESC at -1.0V does not necessarily indicate that -1.0V provides the "poorer" deposition condition than -0.8V. As a matter of fact, at -1.0V, hydrogen evolution reaction generates additional hydroxyl ions to the vicinity of the metal surface compared to at -0.8V. This increased surface pH should accelerate the deposit forming reactions and consequently, -1.0V deposit will show a larger current decrease than -0.8 deposit, if the currents are measured at the same potential. To confirm this, additional experiments were done. The schedule for these experiments are shown in Table 9. Run 7 will be explained as an example. Initially, deposit was formed at -1.0V (1000). After two hours, potential was changed to -0.8V (0000) and two hours was

allowed at the potential. At the end, current was measured. The difference between Run 5 and Run 6 is that initial deposit were formed at different potentials. Because the final current was measured at the same potential, the result of Run 5 can be directly compared to that of Run 6. Likewise, such a comparison can be made for Run 7 and Run 8. It can be deduced from these experiments that -1.0V which yields the deposit with lower cathodic current requirement provides "better" deposition condition than -0.8V does and the high surface pH at -1.0V is more favorable for deposit formation.

The general terms of "poor," "better" and "favorable" used so far to describe the condition for deposit formation need discussion. High solution pH values, high temperatures and large cathodic potentials are found to provide "favorable" conditions for deposit formation and these phenomena could be well explained in terms of surface pH and degree of supersaturation. With known information about the formation of calcareous deposits, it is extremely unlikely that the four parameters of this study have a direct influence on deposit formation. Uncertainty in the direct influence of cathodic potential is still unsolved, but its contribution, if there is any, is not believed large enough to overwhelm its indirect influence. (Attraction and repulsion of charged colloidal particles to and from electrode surface will be discussed later.) Therefore, interpretation of observed behaviour based upon surface pH and degree of

supersaturation is believed to be valid. At high surface pH, i.e., at high degree of supersaturation, the driving force for precipitation is large and, as discussed in Section 2.1 in kinetics, deposition rate becomes high. Therefore, more amount of deposit will precipitate on electrode surface. Unfortunately, experimental evidence can not be presented to prove that the weight of deposit increases under the conditions which provide high degree of supersaturation near electrode surface. The absolute amount of deposit formed over the polarization periods employed in this study was too small for weight comparison. Also, the small decrease in the concentration of deposit forming ions is not adaptable to solution analysis. Also, the unevenness and lack of uniformity of the deposit does not allow modern surface analytical techniques to provide reasonably reliable information about deposit thickness for comparison purposes. However, knowledge of precipitation chemistry allows the terms, "better" and "favorable" to be changed to "higher deposition rate" directly caused by "higher degree of supersaturation." Therefore, in the remaining discussion, these two terms will be used interchangeably.

In Figure 1, the two curves of -1.0V (triangles) and -0.8V (open squares) are shown with others. The slower deviation of the ratio, i_{1000}/i_{500} from the original $\sqrt{2}$ was observed with the -1.0V curve. Because the decay of the ratio was caused by the formation of deposit which functions as an oxygen diffusion barrier, the slower decay with the

-1.0 curve suggests that the deposit formed at -1.0V is poorer than the deposit formed at -0.8V in its capability to block oxygen diffusion. This statement seems to be contradictory to the previous discussion that the high deposition rate obtained at -1.0V results in a better deposit or the lower cathodic current requirement. It has to be noted that the discernible difference between the two curves (triangles and open squares) can be observed only after 5 or 6 hours of deposit formation. Therefore, the discussion that -1.0V provides a better deposition condition because -1.0V gives a higher surface pH than -0.8V is valid only during the initial stage. When an experiment is prolonged, this statement does not seem to hold as suggested by the (1000) curve in comparison with the (0000) curve.

For this behavior, the following explanation is proposed:

Hydrogen evolution reaction inherently involves hydrogen gas formation on electrode surface. When surface coverage is poor and the evolved gas has enough paths to leave the interface, the gas can leave the system without causing any damage to the deposit. Because the gas forming reaction takes place on a metal surface under the deposit, as deposit develops its coverage over electrode surface, the escape paths of the evolved gas decrease and the chances to form gas bubbles and to damage the deposit from their escaping actions increase.

As an attempt to show the above postulation experimentally, a -0.8V condition was studied. At (0001), deposit was formed at -0.8V and potential was changed to -1.0V and held for several minutes. Current was measured every 2 hours. $i_{-1.0}-i_{-0.8}$ was plotted against time (Figure 3). To avoid a large transient current, the potential was changed by slowly turning the potential control thumbwheel at the rate of approximately 0.1 V/min . As shown in Figure 7, the difference of $i_{-1.0}-i_{-0.8}$ increased. Previously in (1000) experiment (Figure 2), it decreased gradually and the presence of water in deposit could explain the different rates of current decay for oxygen current and hydrogen current. The observation with (1000) experiment is in contradiction to this. It is hard to believe that some deposits affect kinetics of cathodic reactions and some others do not. One possible explanation is that gas forming hydrogen evolution reaction damages the continuity of deposit exposing extra electrode surface to solution. Therefore, the current difference, $i_{-1.0}-i_{-0.8}$ for this experiment has two components; hydrogen current and extra amount of oxygen current due to the newly exposed electrode surface. The previous observation of slow decay rate of i_{1000}/i_{500} ratio at (1000) compared to that at (0000) is in good agreement with the present finding, if both behaviors are explained as a hydrogen gas effect. Occurrence of an additional cathodic reaction when cathodic potential is raised to -1.0 , however, can not be precluded, contributing

to the increase in $i_{-1.0}-i_{-0.8}$ to some extent. As shown in Figure 4, the plateau region of cathodic polarization curve was obtained after the electrode was polarized in deposit-free solution for one hour at $-0.8V$. During this period, air formed surface iron oxide film is believed to be reduced gradually. If deposit covers this surface oxide, the presence of oxide film may extend for a longer period and when cathodic potential is raised to $-1.0V$, its reduction can contribute to the increase in total cathodic current.

5.2.4 Fluid Velocity

The three-dimensional motion of a liquid near a rotating disc is well explained by Pleskov and Filinovskii (81). In the bulk, as an example, the velocity of the solution perpendicular to the disc can be expressed as

$$\text{velocity} = 0.886 (\nu \omega)^{1/2}$$

where ν = kinematic viscosity

ω = rotation speed.

Therefore, various flowing conditions can be simulated by rotating a disc electrode. In this study, 500 and 1000 rpm were used.

The effects of electrode rotation speed (RPM) of Table 7 are schematically presented in Figure 26. The effect decreased from $32.9 \mu A$ "without deposit" to $24.3 \mu A$ "with deposit." However, the average current also decreased from $112.8 \mu A$ "without deposit" to $80.8 \mu A$ "with deposit."

RPM effect : $32.9 \rightarrow 24.3 \text{ } \mu\text{A}$

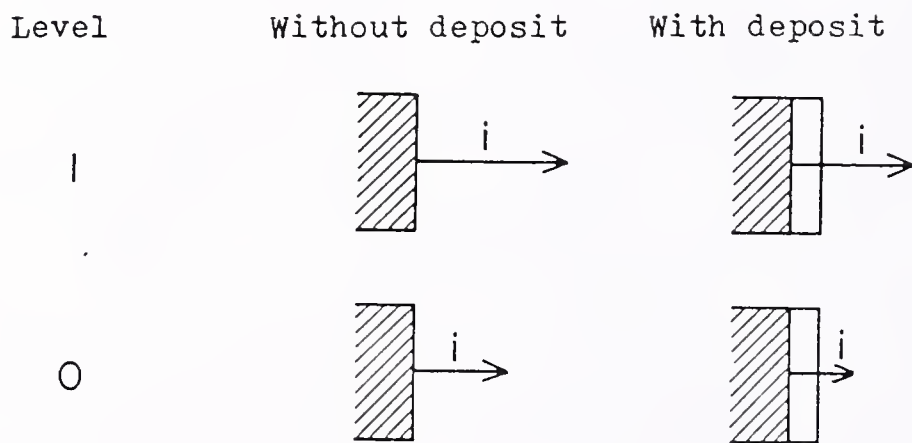


Figure 26 Schematic Presentation of the RPM Effects

Therefore, direct comparison cannot be made between the two effects.

In Table 8, RPM-0-Subgroup has the same effective surface coverage as RPM-1-Subgroup for both Group Oxy and Group Hydr indicating that the percentage of current decrease is the same whether electrode rotation speed is 500 or 1000 rpm. From equation [2],

$$\delta = s D^{1/3} v^{1/6} \omega^{-1/2} \quad [2]$$

as rotation speed (ω) increases, diffusion layer thickness (δ) decreases to the minus one-half power of ω . As the diffusion layer decreases in thickness, oxygen diffusion rate increases, generating more OH^- . However, the diffusion rate of OH^- away from electrode surface also increases because of the decrease in δ . In addition, HCO_3^- diffusion to electrode surface also increases. With its high buffering capacity, the net increase in surface pH, if there is any, will be negligible. Also, the negligible difference in effective surface coverage indicates that these opposing factors compensate the increase in OH^- generation rate with no net influence on deposit formation within the pH range studied. Because hydrogen evolution reaction is activation controlled as can be seen in Figure 21, variation in electrode rotation speed should not affect this reaction and the rate of OH^- generation. Therefore, the above discussion

considering the accelerated oxygen transport as the source of accelerated OH^- generation is valid.

To further verify that level 0 of RPM (500 rpm) provides the same deposit forming condition as level 1 does, which is the indication from the previous effective surface coverage study, additional experiments were carried out. Table 9 shows the schedule used for this study. The schedule for Run 3 will be explained as an example. Initially, deposit was formed at 1000 rpm (0100). After two hours, rotation speed was reduced to 500 rpm (0000) without interruption and another two hour cathodic protection was maintained. Current was measured at the end of the experiment. It has to be noted that from these experiments on, Specimen B was used because Specimen A was damaged during this study.

The difference between Run 1 and Run 2, and Run 3 and Run 4 is that initial two hour deposit formation was done at different rotation speeds. When Run 1 is compared to Run 2, and Run 3 is compared to Run 4, no significant difference is found between the final currents, supporting the previous discussion that increase in OH^- generation rate or oxygen transport rate with increase in rotation speed is compensated by the increase in the rate of OH^- diffusion away from electrode surface. The deposition rate is same for both rotation speeds.

Also, the 1000 rpm curve (open circles) shows almost the same behavior as the 500 rpm curve (open squares) in

Figure 1, supporting previous discussion that the increased oxygen transport rate and thus the increased OH^- generate rate with the increase in the rotation speed was compensated by the increased OH^- diffusion rate.

5.2.5 Deposit Morphology

The SEM pictures (Figures 4 through 8) were taken after the i_{1000}/i_{500} ratio reached 1.05 ± 0.1 (except (0010)). Therefore, polarization times were different. There is no distinctive difference among the photographs except that high deposition rate group, i.e., (0000), (1000) and (0100), shows large elongated particles whereas low deposition rate group, i.e., (0010) and (0001), shows relatively small particles. Some of the deposits formed at (1000), i.e., -1.0V, showed amorphous type deposit near the center of electrode. It may be due to very large deposition rate at which crystal growth rate exceeds lattice alignment rate yielding precipitates of high degree of imperfection. Though deposit thickness can not be measured under SEM, the scratches formed at 6 μ diamond polish can be related to it. At high deposition rate (Figures 4, 5 and 6), the scratches are well coated and at low deposition rate (Figures 7 and 8) many scratches can be seen suggesting thin deposits, though the period of cathodic protection was longer for the latter. The difference in deposit morphology can be related to the nucleation growth phenomena of precipitation in supersaturated solution.

The difference in degree of supersaturation or concentration of reacting species results in the change of the size of precipitates. In general, particle size increases, passes through a maximum and then decreases as the concentration of reacting species increases (89). Same type of explanation is offered by Laitinen and Harris (84). But the decrease in particle size is attributed to homogeneous nucleation whereas the increase in particle size represents heterogeneous nucleation. They stated that homogeneous nucleation is very rare and, citing the work by Fisher (90), stated that even high purity reagents contain large number of insoluble particles, far more than needed for nucleation sites. The system employed for these studies also provides metal surface as nucleation sites. Therefore, whether particles are formed in solution or on electrode surface, the mode of nucleation is believed to be heterogeneous. And, as was discussed above, in heterogeneous nucleation, particle size increases with increase in degree of supersaturation which results in increased deposition rate. The SEM micrographs show the same trend in particle size. The high deposition rate group has large particles (Figures 4-6), whereas the low deposition rate group has small particles (Figures 7 and 8). This is also in good agreement with the observation of large particles at large cathodic potentials (53).

It was found that the peculiar behavior of increase in $(i_{-1.0}-i_{-0.8})$ was distinctive at (0001) (Figure 3). From

the above discussion and the SEM micrographs, it can be stated that low degree of supersaturation results in fine particles and consequently dense film because low deposition rate reduces occlusion type contamination, e.g., mother liquor (91). If this is the situation, escape of hydrogen gas bubbles may be more difficult at the conditions which yield dense films. Therefore, the damage of the film caused by the escape of the hydrogen gas bubbles will be more serious for dense films. This mechanism can explain the increase in $i_{-1.0}$ - $i_{-0.8}$.

5.2.6 Chemical Analysis

Two different types of deposit morphology were observed; a background layer and globular particles with various irregularities on top of the background layer. It is not clear if the particles actually sit on top of the background layer or they both grew together with different growth rates.

With energy dispersive X-ray analysis, the globular particles were analyzed (Figure 10). Two peaks of Ca, K_{α} and K_{β} are detected. Small peaks of Mg, Al, Si, S and Cl are also found. S and Cl are apparently from the solution and Si is from SiC grit paper used for surface preparation. Al is from the aluminum foil used to fix the specimen in specimen holder also serving as an electron flow path so that surface charge effect can be minimized. It is hard to think that Fe is dissolved and incorporated into the deposit under cathodic protection condition. Instead, the probable

source of the detected Fe peak is the iron substrate present under the deposit. Because of large escape depth of X-ray, the iron present under and in the neighborhood of globular particles can send out relatively large signal. Not all the globular particles are rich in Ca. Some particles are found not to have enough Ca detectable from X-ray analysis (Figure 11). These particles are mostly Si with less amount of Mg, probably the particles formed around SiC grinding paper residues. Electron beam was focused on the background layer for compositional analysis (Figure 12). Only Fe peaks are detected; two K lines and one L line. It should not be concluded that the background layer is all iron compounds because the relative mass of deposit is very small compared to the mass of iron substrate which can send out X-ray signals up to several microns in thickness. Therefore, small signals coming out from the deposit can be obscured by the large signals from substrate. Because different elements have different response against incoming electron beam, the peak heights do not necessarily indicate the relative amount (or concentration) of each element. In principle, peak intensity is proportional to the concentration of corresponding element (92).

$$\frac{I_A}{I_B} = k \cdot \frac{C_A}{C_B}$$

where I_A = intensity of element A peak

I_B = intensity of element B peak

C_A = concentration of A

C_B = concentration of B

k = ratio of cross-sectional area.

But k is influenced by such factors as atomic number, excitation energy, depth, sample geometry and concentration among which atomic number is the most important factor, especially as sample becomes thin. Taking the Si peak as an arbitrary reference, Hren et al. (92) reported the intensity of other elemental peaks (Table 11). Taking these factors into consideration, globular particles are rich in Ca with Mg content reduced to about half of its original intensity.

To obtain compositional information from background layer, a surface sensitive analytical technique was used. Because of the small escape depth of photoelectrons ($\sim 50 \text{ \AA}$ or less), ESCA (or XPS) was selected. The source beam of ESCA is Mg K_{α} X-ray with 1253.6 KeV of energy. Because the size of the X-ray beam used for this study was almost 1 cm^2 in area, ESCA spectra provide chemical information over the almost entire area of Specimen C. However, the area coated with globular particles is small compared to non-coated area, ESCA scans can be interpreted as representing the background layer without significant error.

ESCA survey scan is shown in Figure 13. Because of the presence of water as well as oxygen containing compounds, a large peak of O_2 is detected. Peaks of Na and Cl suggest that these ions are present in the deposit, either adsorbed or trapped. Auger peaks are also detected for O and Fe.

Table 11 Values of k

<u>Atomic No.</u>	<u>Element</u>	<u>k</u>
11	Na	5.77
12	Mg	2.07
13	Al	1.42
14	Si	1.0
15	P	-
20	Ca	1.02
26	Fe	1.27

Note: Thin film at 100 keV.

The peak of Cl was used as internal standard and all other peaks were adjusted by such an amount of eV that was necessary to make the Cls peak to 285.0 eV. Single element scans were done for Mg, Fe and Ca (Figures 14, 15 and 16). Presence of a large amount of Mg gave a well-defined 2s peak at 90 eV (Figure 14). In Figure 15, Fe 2p doublets are shown; 2p₃ at 714 and 2p₁ at 726 eV. Full width at half height (FWHH) of 2p₁ peak is about 5 eV which is too large to be a single peak. Several iron compounds such as FeO, Fe₂O₃, FeOOH and Fe₃O₄ are reported to have 2p₁ peak between 710 and 712 eV (93) and the large FWHH of 2p₁ peak is believed to be due to the presence of these various iron compounds. Ca peak is not so well-defined as the others. 2p₁ and 2p₂ doublets are not seen.

For quantitative analysis, each peak was normalized according to the following equation (94):

$$A_N = \frac{A}{\sigma \cdot E_K^{1.75} \cdot \Delta T \cdot \#sw}$$

where A_N : normalized area
 A : area under the peak
 σ : cross-sectional area
 E_K : kinetic energy
 ΔT : dwell time
 $\#sw$: number of sweeps.

Reported values of σ were used for normalization (93). For Fe, the 2p₁ peak at 714 eV was used and for Ca, 347 eV peak

was used. The normalized areas of Fe and Ca were compared to that of Mg. Calculation showed that the amount of Fe present in the deposit is less than 10% of Mg and that of Ca is less than 5% of Mg. In an attempt to find the relationship between chemical composition and the four parameters, deposits formed under various conditions were studied with ESCA. However, Ca varied from 2 to 7% of Mg at most and Fe varied from 6 to 13% of Mg at most. No trend was found for the compositional variation with parameter variation. A large concentration of Ca as reported by Humble (45) was not found. To remove sample handling contamination which was indicated by a large C1s peak and which might have affected signal collection, the sample was sputtered with Ar beam and the three single element scans were repeated. For better Ca resolution, medium level resolution was used and to compensate weak signal, number of sweeps was increased to 100 (Figure 17). $2p_1$ peak at 350 eV and $2p_3$ peak at 347 could be separated. The neighboring peaks match the Auger lines of Zn which might have come from the polishing wheel used for diamond polishing. The method of using the 347 peak as $2P_3$ for normalization was confirmed to be appropriate. Sputter etching did not change the result.

To find anions which are coordinated with Mg and Ca in the deposit, FTIR was used. Figure 18 was obtained from (0000) after 2 hours and 6 hours of polarization. Water peaks are at 3300 and 1600 cm^{-1} , CO_3^{--} peak at 1400 cm^{-1} and

$\text{SO}_4^{=}$ peak at 1100 cm^{-1} . The large peak at 750 cm^{-1} was also detected with a fresh sample. Longer period of polarization gave a smaller water peak at 3300 cm^{-1} indicating the relative amount of deposit has increased compared to water.

Because MgSO_4 and CaSO_4 compounds have a large solubility product, $\text{SO}_4^{=}$ peak is believed from the solution remaining in the deposit. The other two anion peaks, OH^- and $\text{CO}_3^{=}$ are believed to be coordinated with Mg^{++} and Ca^{++} .

Chemical analysis showed that the elongated particles forming network type background is mostly comprised of magnesium. Globular particles with some irregularity are relatively rich in calcium. Smith and Mattson (52) have made similar observations. FTIR analysis result indicated that $\text{CO}_3^{=}$ and OH^- are present. From solubility consideration, $\text{CO}_3^{=}$ can be assigned to CaCO_3 and OH^- can be assigned to $\text{Mg}(\text{OH})_2$. As discussed, CaCO_3 is believed to have certain amount of MgCO_3 ; the ratio of which is not known.

5.2.7 Interaction Effects

Interaction effect is the variation of current when two or more parameters are changed at the same time. For example, E*T interaction effect implies the difference between cathodic currents when E is changed to level 1 with T at level 0 and with T at level 1. A few interaction effects are significant. In case of "without deposit," E*T interaction effect is the most significant. This may be explained as: when potential is changed to -1.0V (level 1)

from -0.8V (level 0), additional hydrogen evolution reaction takes place. As was discussed in Section 4.1, at 16°C (level 1) this cathodic reaction slows down and the total current increase due to the occurrence of this additional reaction will be smaller. Therefore, E effect will diminish at 16°C (level 1).

In case of "with deposit," pH*T interaction effect is the most significant. The effect of temperature is, according to the suggested surface pH model, increase in surface pH. However, as was previously discussed, its effect on the rate of precipitation reaction may be more significant. If this is the correct mechanism of temperature effect on reaction kinetics, then

$$\text{rate} = A \exp \left[-\frac{Q}{RT} \right]$$

where A: constant

Q: activation energy.

Therefore, at two different levels of temperature,

$$\ln \frac{\text{rate}_1}{\text{rate}_0} = \frac{Q}{R} \left(\frac{1}{T_0} - \frac{1}{T_1} \right) .$$

Whatever surface pH is, the ratio of two rates is same. At high surface pH (pH level at 0), reaction rate is large compared to that at low surface pH (pH level at 1).

Therefore, at low surface pH, decrease in reaction rate with temperature decrease will be smaller than that at high surface pH. The negative interaction effect which indicates

that the change in pH from 0 to 1 is not significant for deposit formation at low temperature (level 1) may be explained as above.

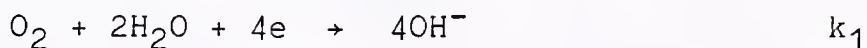
Other interaction effects are less significant. They can be explained in view of surface pH and degree of supersaturation, or deposition rate, as above.

5.3 Surface pH Model

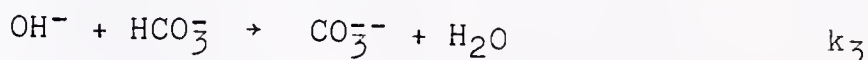
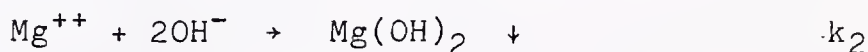
So far, discussion about the influence of parameters on surface pH and degree of supersaturation has been limited to such qualitative descriptions as "increase in surface pH," "higher degree of supersaturation" and "higher deposition rate." It would be ideal if these descriptions could be made quantitatively, instead of qualitatively. From previous discussion, it can be deduced that surface pH is the master parameter and other phenomena can be quantitatively described if surface pH can be obtained.

Reactions taking place near the electrode surface which affect surface pH are

1. OH⁻

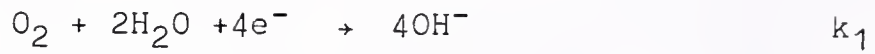


$$\text{Diffusion:} \quad J = -D_{\text{OH}^-} \frac{C_{\text{OH}^-}^s - C_{\text{OH}^-}^b}{\delta}$$

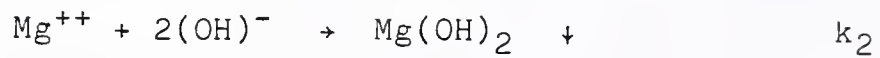


2. O₂

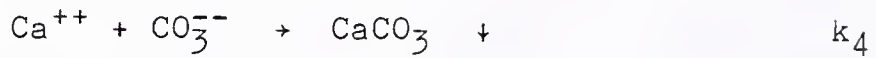
$$\text{Diffusion: } J = D_{O_2} \frac{C_{O_2}^b - C_{O_2}^s}{\delta}$$

3. Mg⁺⁺

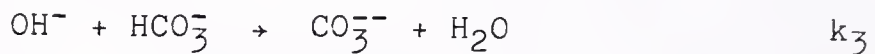
$$\text{Diffusion: } J = D_{Mg^{++}} \frac{C_{Mg^{++}}^b - C_{Mg^{++}}^s}{\delta}$$

4. CO₃⁻⁻

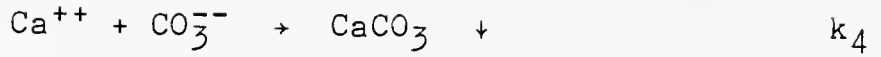
$$\text{Diffusion: } J = -D_{CO_3^{--}} \frac{C_{CO_3^{--}}^s - C_{CO_3^{--}}^b}{\delta}$$

5. HCO₃⁻

$$\text{Diffusion: } J = -D_{HCO_3^-} \frac{C_{HCO_3^-}^s - C_{HCO_3^-}^b}{\delta}$$

6. Ca⁺⁺

$$\text{Diffusion: } J = D_{Ca^{++}} \frac{C_{Ca^{++}}^b - C_{Ca^{++}}^s}{\delta}$$



where k 's are rate constants with appropriate units. C^s and C^b are surface concentration and bulk concentration, respectively. Negative sign is assigned to a diffusional flux if it is flowing away from the surface, and vice versa. From the above reactions, six rate equations can be set up per unit area:

$$\begin{aligned} \frac{d[\text{OH}^-]}{dt} = & 4k_1 f([\text{O}_2]) - D_{\text{OH}^-} \frac{C_{\text{OH}^-}^s - C_{\text{OH}^-}^b}{\delta} - 2k_2 g([\text{Mg}^{++}], [\text{OH}^-]) \\ & - k_3 [\text{OH}^-][\text{CO}_3^{--}] \end{aligned} \quad [14]$$

$$\frac{d[\text{O}_2]}{dt} = D_{\text{O}_2} \frac{C_{\text{O}_2}^b - C_{\text{O}_2}^s}{\delta} - k_1 f([\text{O}_2]) \quad [15]$$

$$\frac{d[\text{Mg}^{++}]}{dt} = D_{\text{Mg}^{++}} \frac{C_{\text{Mg}^{++}}^b - C_{\text{Mg}^{++}}^s}{\delta} - k_2 g([\text{Mg}^{++}], [\text{OH}^-]) \quad [16]$$

$$\begin{aligned} \frac{d[\text{CO}_3^{--}]}{dt} = & - D_{\text{CO}_3^{--}} \frac{C_{\text{CO}_3^{--}}^s - C_{\text{CO}_3^{--}}^b}{\delta} - k_4 h([\text{Ca}^{++}], [\text{CO}_3^{--}]) \\ & + k_3 [\text{OH}^-][\text{HCO}_3^-] \end{aligned} \quad [17]$$

$$\frac{d[\text{HCO}_3^-]}{dt} = D_{\text{HCO}_3^-} \frac{C_{\text{HCO}_3^-}^b - C_{\text{HCO}_3^-}^s}{\delta} - k_3[\text{OH}^-][\text{CO}_3^{--}] \quad [18]$$

$$\frac{d[\text{Ca}^{++}]}{dt} = D_{\text{Ca}^{++}} \frac{C_{\text{Ca}^{++}}^b - C_{\text{Ca}^{++}}^s}{\delta} - k_4 h([\text{Ca}^{++}], [\text{CO}_3^{--}]) \quad [19]$$

where f , g and h are appropriate rate functions with arguments in brackets.

Because the rate of cathodic current decay is large in initial period and nucleation may require induction period, the steady state assumption can not be made for initial stage. However, as current decay rate decreases and particle growth reaches stable state at which deposition rate can be expressed as a function of degree of supersaturation, a steady state assumption is valid.

At steady state,

$$\frac{d[\text{species}]}{dt} = 0$$

for all of the six equations. By substituting [15], [16] and [18] into [14], and [8] and [19] into [17], the two following equations can be derived:

$$4D_{\text{O}_2} \frac{C_{\text{O}_2}^b - C_{\text{O}_2}^s}{\delta} = D_{\text{OH}^-} \frac{C_{\text{OH}^-}^s - C_{\text{OH}^-}^b}{\delta} + 2D_{\text{Mg}^{++}} \frac{C_{\text{Mg}^{++}}^b - C_{\text{Mg}^{++}}^s}{\delta}$$

$$+ D_{\text{HCO}_3^-} \frac{C_{\text{HCO}_3^-}^b - C_{\text{HCO}_3^-}^s}{\delta} \quad [20]$$

$$D_{\text{Ca}^{++}} \frac{C_{\text{Ca}^{++}}^b - C_{\text{Ca}^{++}}^s}{\delta} = - D_{\text{CO}_3^{--}} \frac{C_{\text{CO}_3^{--}}^s - C_{\text{CO}_3^{--}}^b}{\delta} + D_{\text{HCO}_3^-} \frac{C_{\text{HCO}_3^-}^b - C_{\text{HCO}_3^-}^s}{\delta} \quad [21]$$

The left side of equation [20] corresponds to the oxygen reduction current per unit area uncoated with deposit. In principle, a surface pH which satisfies [20] must also satisfy [21]. At present time, since the kinetics of CaCO_3 precipitation are not well quantified, $C_{\text{Ca}^{++}}^s$ can not be calculated. Its calculation from the solubility of CaCO_3 does not satisfy [21] at any pH. Thus, equation [21] can not function as a test tool to verify the pH value calculated from equation [20].

During the initial period, but after steady state assumption is satisfied, diffusional flux will not be affected by the small amount of deposit present as a diffusion barrier. As the deposit grows and effectively covers the surface, ionic species see the deposit as

diffusion barrier and the "operational" D value will change. However, species are traveling through the solution in the deposit, whether adsorbed or trapped, not through the ionic compounds of the deposit. Therefore, the inherent nature of diffusion does not change with deposit growth. Instead of changing D values to "operational" D values, change of δ is preferable in view of the fact that ionic species traveling between the deposit particles in a zig-zag type will have a longer diffusion path than the thickness of deposit. Because all the terms in [20] and [21] have same length of diffusion path, δ , it can be simply dropped. Therefore, using D values in solution should not affect the surface pH calculation.

All experimental D values could not be found. To obtain D values, the Einstein relation between mobility and diffusion coefficient was used.

$$D = 411.7 \times 10^{-16} \text{ kT } U_{\text{abs}} \quad [22]$$

where D: diffusion coefficient (cm^2/sec)

U_{abs} : absolute mobility ($\text{cm}/\text{sec-dyne}$)

k: Boltzman's constant ($\text{cal}/^\circ\text{K}$)

T: temperature ($^\circ\text{K}$).

Also,

$$U_{\text{abs}} = 6.469 \times 10^6 \frac{\Lambda}{z} \quad [23]$$

where Λ : equivalent conductivity ($\text{cm}^2/\Omega\text{-equivalent}$)

z : number of charge.

From [22] and [23],

$$D = 2.663 \times 10^{-7} \frac{\Lambda}{z} . \quad [24]$$

Reported conductivities (95) are listed in Table 12 with calculated diffusion coefficients. It has to be noted that the conductivities listed in Table 12 are limiting conductivities, i.e., at infinite dilution. Because of lack of data on equivalent conductivities at various concentrations, especially in seawater, these data were used for approximation. For D_{O_2} , $1.98 \times 10^{-5} \text{ cm}^2/\text{sec}$ was used (96). For HCO_3^- calculations, $pK_1=6$ and $pK_2=9.1$ (2) were used according to

$$\text{HCO}_3^- = C_T \alpha_1$$

where C_T : total carbonate concentration, $2.39 \times 10^{-2} \text{ M}$

$$\alpha_1 = \frac{K_1 [\text{H}^+]}{[\text{H}^+]^2 + K_1 [\text{H}^+] + K_1 K_2} .$$

Kinetic parameters of the rate of $\text{Mg}(\text{OH})_2$ precipitation could not be found. In general, once nucleation and growth are initiated, degree of supersaturation decreases from its high initial value for further precipitation (84). Thus

$C_{\text{Mg}^{++}}^S$ was calculated from its solubility product

Table 12 Limiting equivalent ionic conductivities in aqueous solutions at 25°C and calculated diffusion coefficients

<u>Species</u>	<u>Λ^* ($\frac{\text{cm}^2}{\Omega \cdot \text{eq}}$)</u>	<u>$D_{\text{calculated}}^{**}$ (cm/sec²)</u>
Ca ⁺⁺	59.5 0.79x10 ⁻⁵	
Mg ⁺⁺	53.06 0.71x10 ⁻⁵	
OH ⁻	198.6 5.24x10 ⁻⁵	
HCO ₃ ⁻	44.5 1.19x10 ⁻⁵	
CO ₃ ⁻⁻	72 0.96x10 ⁻⁵	

* Λ from Lange's Handbook of Chemistry (95)

** D was calculated from

$$D = 2.663 \times 10^{-7} \frac{\Lambda}{121}$$

$$[\text{Mg}^{++}] = \frac{K_{\text{Mg}(\text{OH})_2}}{[\text{OH}^-]^2}$$

where $K_{\text{Mg}(\text{OH})_2} = 10^{-10.6}$.

Calculations were repeated until both sides of [20] are equated. It was found by trial and error that a surface pH between 9.3 and 9.4 could satisfy [20]. This calculated pH is at a cathodic potential at which oxygen transport is diffusion limited. At a higher cathodic potential which is large enough to evolve hydrogen, an additional OH^- source can be created which can be quantified from current measurement, and surface pH will increase accordingly. For a better approximation, quantitative information on the kinetics of $\text{Mg}(\text{OH})_2$ and CaCO_3 precipitation is necessary. Even when precipitation of $\text{Mg}(\text{OH})_2$, i.e., the second term of equation [20] is neglected, surface pH well below 10 can be obtained.

Based upon this model and equation [20], influence of the four parameters on the variation of surface pH can be investigated:

1) Cathodic potential

Because of the presence of additional OH^- generation source, surface pH ($C_{\text{OH}^-}^s$) increases and deposit formation will be accelerated. Net increase will be reduced by the decrease in $C_{\text{Mg}^{++}}^s$ and $C_{\text{HCO}_3^-}^s$.

2) Rotation speed

Increase in rotation speed increases oxygen current and OH^- generation rate. However, mass transport of other species also increases and there is no net increase in $C_{\text{OH}^-}^s$. Equation [20] does not contain any term which varies with rotation speed except the common denominator δ . Same surface coverage, same final current requirement under combined conditions and the same behavior of i_{1000}/i_{500} decay, at two different rotation speeds, can be explained from this effect.

3) pH

Decrease in bulk pH will decrease surface pH, also. From equation [20], decrease in $C_{\text{OH}^-}^b$, if $C_{\text{OH}^-}^s$ does not vary, will increase $(C_{\text{OH}^-}^s - C_{\text{OH}^-}^b)$ and $(C_{\text{HCO}_3^-}^b - C_{\text{HCO}_3^-}^s)$ will also increase because $C_{\text{HCO}_3^-}^b$ increases. Maintaining same $C_{\text{OH}^-}^s$ will not vary $(C_{\text{Mg}^{++}}^b - C_{\text{Mg}^{++}}^s)$. But the left term of equation [20] does not vary with $C_{\text{OH}^-}^b$. Therefore, $C_{\text{OH}^-}^s$ must vary in such a way that the right side of equation [20] can be maintained same as the unvarying left side. Because all the three terms of the right side of equation [20] vary in the same direction, $C_{\text{OH}^-}^s$ should decrease and, as a result, deposition rate decreases. Lower effective surface coverage and higher i_{1000}/i_{500} ratio at a lower solution pH can be explained from this effect.

4) Temperature

Influence of temperature on surface pH is somewhat complicated. The left side of equation [20] increases with decrease in temperature because $C_{O_2}^b$ increases. Because of higher solubility of $Mg(OH)_2$ at a lower temperature, $C_{Mg^{++}}^s$ will increase. The decrease of the second term on the right side of the equation, therefore, must be compensated by increase of the first and/or the third term. These two terms always vary in the same direction. Therefore, $C_{OH^-}^s$ should increase. Increase in surface pH and increase in solubility product have opposite effect on the rate of deposit formation. In order to find which one of the two is more significant, quantitative information on the rate of $Mg(OH)_2$ precipitation is necessary which is not available at present. However, as we discussed in Section 4.1, if an Arrhenius type relationship is the valid mechanism between deposition rate and temperature, exponentially decreasing deposition rate with decrease in temperature will be substantial to overwhelm any increase in surface pH.

CHAPTER 6 CONCLUSIONS

Within the range studied,

1. the influence of the parameters on inherent cathodic reactions decreases in the order of flow velocity, cathodic potential, temperature and pH;
2. the influence of the parameters on cathodic current requirement as deposit develops on surface, decreases in the order of pH, flow velocity, cathodic potential and temperature;
3. the influence of the parameters on the rate of calcareous deposit formation decreases in the order of pH, temperature, cathodic potential and flow velocity and all of these influences can be interpreted in terms of surface pH and degree of supersaturation except for temperature effect that may be explained by thermal activation kinetics;
4. deposits formed at low deposition rate, i.e., low pH and low temperature are found to be thin but dense whereas those formed at high deposition rate are found to be thick and porous;
5. formation of hydrogen gas bubbles is believed to damage the continuity of the deposit and its effect appears to be large with dense deposits;

6. initial deposit layer is mostly magnesium compounds whereas globular particles are rich in calcium;
7. transport of oxygen is effectively retarded by the deposits, however, hydrogen current decreases more slowly than oxygen current because of the presence of water in the deposits; and
8. a mathematical surface pH model was proposed--exact surface pH can not be calculated until all the kinetic parameters of $\text{Mg}(\text{OH})_2$ precipitation reaction are found. Calculated surface pH is below 10.

CHAPTER 7 RECOMMENDATIONS FOR FURTHER RESEARCH

For better understanding of influence of the parameters on formation of calcareous deposits and thereby for better utilization of the deposits in cathodic protection, the following suggestions are made:

1. Extension of level of each parameter, especially flow velocity and temperature, to represent actual conditions, will reveal the nature of deposit formation in the environment in which cathodic protection is applied.
2. When experimental periods are extended and thick deposits are obtained, possible changes in the order of influence among parameters will occur:
 - 2-1 Because of the development of unevenness of the deposit surface as deposit grows, solution flow near deposit surface will be turbulent and this may have significant effect on the growth of deposits.
 - 2-2 Evolution of hydrogen will be more significant as deposit grows in thickness and coverage of surface.
3. Biological aspects of marine environments in the formation of calcareous deposits should also be

studied. Organic carbonates, e.g., skeletal materials have a large content of carbonate and they may have significant effect on the development of calcareous deposits, especially where biological activities are high.

APPENDIX 1 CATHODIC PROTECTION

Formation of calcareous deposits is one of the characteristic features of cathodic protection applied to metals in marine environment. Cathodic protection is to prevent the dissolution of metals into surrounding environments: i.e., to stop the following anodic reaction, if the metal is iron:



The principle of cathodic protection can be viewed as supplying additional electrical energy to the chemical free energy of the metal so that the total energy level is below that of its ionic counterpart.

Figure 27 is a schematic diagram of cathodic protection: sacrificial anode method and impressed current method. Figure 28 is a schematic diagram of energy level before and after cathodic protection. Let us assume that reaction [1] is the reaction of the iron dissolution. Taking the free energy of pure solid metal for reference (zero), metal, in this case, iron is at zero energy level. The free energy of its ionic counterpart, ferrous ion is below that of iron. Therefore, the reaction [1] is accompanied by a negative change of free energy and is

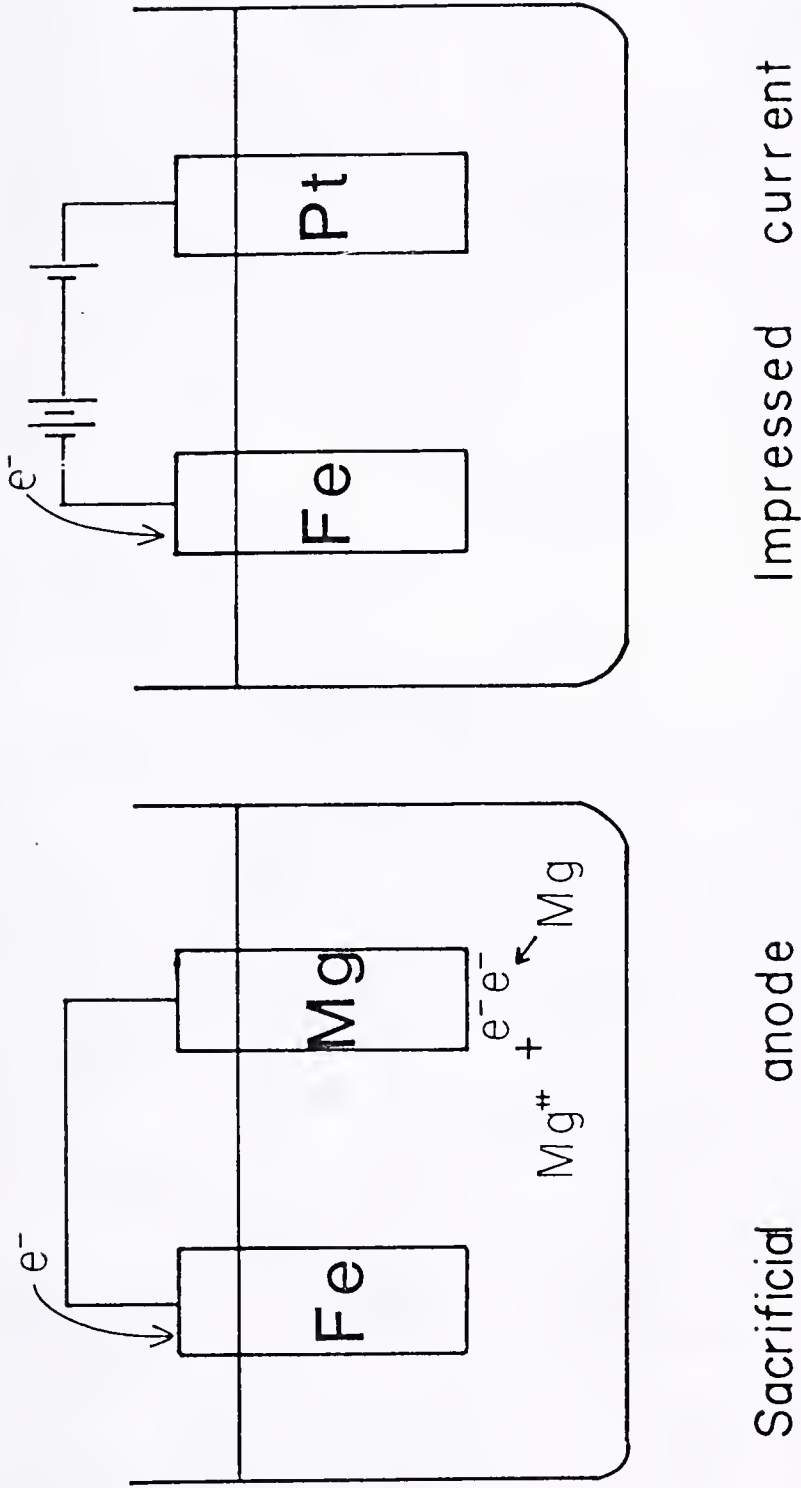


Figure 27 Schematic Layouts of Cathodic Protection System: Sacrificial Anode Method and Impressed Current Method

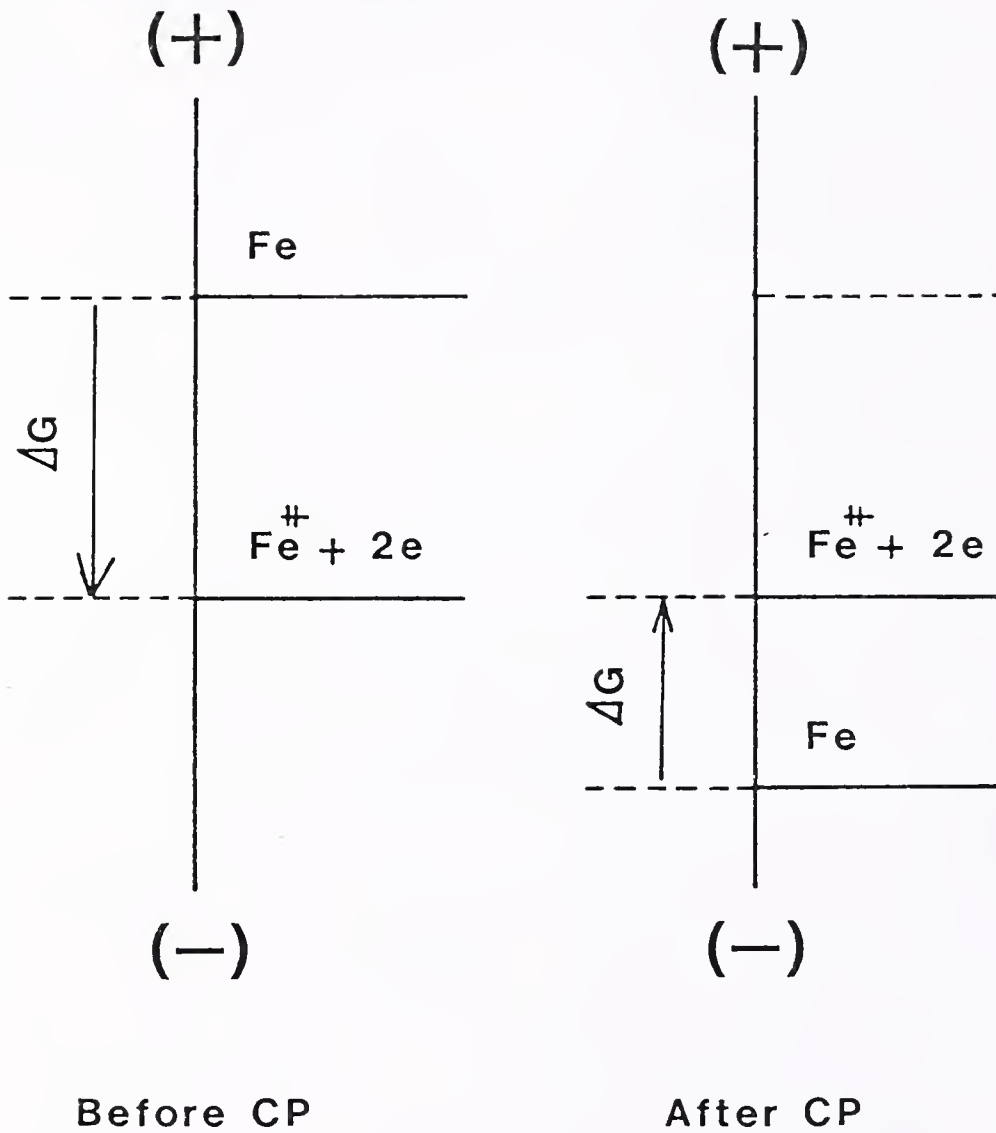


Figure 28 Diagram of Relative Energy Levels of Fe and Fe⁺⁺ (or Fe⁺⁺⁺) Before and After Cathodic Protection

spontaneous. Cathodic protection involves physically connecting a metal to the negative terminal of a power supply unit in order to provide a negative electrical energy. In case of sacrificial anode method, the power is supplied by a different metal which yields negative charges from its dissolution reaction,



Because electrical energy is one of the various forms of energy like chemical free energy, the former can be added to the latter with appropriate conversion factor. Finally, the level of the total energy of metal is lowered below that of its ionic counterpart and the corrosion reaction [1] becomes thermodynamically nonspontaneous.

APPENDIX 2

2⁴ FACTORIAL DESIGN

In exploring a functional relationship between parameters and result, it might appear reasonable at first sight to employ a comprehensive approach in which the entire range of every parameter is investigated. However, during the course of experiments, it may be found that this is an inefficient way to organize experimental programs if one or more of the parameters or certain subranges have little influence on the result. Factorial design technique is arbitrarily selecting two or more of the levels of the range of a parameter and combining the parameters in order to find which of the parameters and which subranges have significant influence on final result. Afterwards, another experimental schedule can be constructed for indepth analysis in critical ranges. Therefore, for the cases in which the relative importance of parameters and the ranges to be studied are not known, factorial technique becomes a good tool to design entire experiment at the outset. The advantages of factorial design are

- i) economy in experiment in time and number of runs
- ii) interaction effect which is difficult to study in a sequential "one-parameter-at-one-time" method
- iii) minimization of experimental error.

These advantages will become clear through this discussion. In a 2^4 factorial design, four parameters are selected and two levels are assigned to each parameter. Therefore, the number of experiments is $2 \times 2 \times 2 \times 2 = 16$. A, B, C and D will be used to represent the four parameters and 0 and 1 will be used for the two levels. The total 16 different combinations are shown in Table 13. Two groups of effects (influence on result) can be calculated; main effects and interaction effects. It can be seen from Table 13 that the difference of results, $(R_2 - R_1)$ is caused by changing the level of A from 0 to 1. The same relationship holds for $(R_4 - R_3)$, $(R_6 - R_5)$, $(R_8 - R_7)$, etc. Main effect of A is calculated by adding the differences and dividing the sum by 8. Main effect of C and D can be calculated in a similar way. Likewise, the difference in result between No. 1 and No. 3 observations, $(R_3 - R_1)$ is caused by changing the level of B from 0 to 1. The same relationship holds for $(R_4 - R_2)$, $(R_7 - R_5)$, $(R_8 - R_6)$, etc. Through the same procedure as for main effect of A, main effect of B can be calculated.

Against the main effect, an interaction effect is the influence observed when more than one parameter is varied. As was discussed, $(R_2 - R_1)$ is caused by changing the level of A from 0 to 1 when B is at level 0. $(R_4 - R_3)$ is also caused by changing the level of A from 0 to 1. But this time, the level of B is at level 1. Therefore, $[(R_4 - R_3) - (R_2 - R_1)]/2$ can be interpreted as the influence when both of A and B are changed from level 0 to level 1 at the same time. The same

Table 13 Arrangement of 2^4 factorial design experiment, duplicated

Observation number	A	B	C	D	Result		
					First run	Second run	Average
1	0	0	0	0	R _{1,1}	R _{1,2}	R ₁
2	1	0	0	0	R _{2,1}	R _{2,2}	R ₂
3	0	1	0	0	R _{3,1}	R _{3,2}	R ₃
4	1	1	0	0	R _{4,1}	R _{4,2}	R ₄
5	0	0	1	0	R _{5,1}	R _{5,2}	R ₅
6	1	0	1	0	R _{6,1}	R _{6,2}	R ₆
7	0	1	1	0	R _{7,1}	R _{7,2}	R ₇
8	1	1	1	0	R _{8,1}	R _{8,2}	R ₈
9	0	0	0	1	R _{9,1}	R _{9,2}	R ₉
10	1	0	0	1	R _{10,1}	R _{10,2}	R ₁₀
11	0	1	0	1	R _{11,1}	R _{11,2}	R ₁₁
12	1	1	0	1	R _{12,1}	R _{12,2}	R ₁₂
13	0	0	1	1	R _{13,1}	R _{13,2}	R ₁₃
14	1	0	1	1	R _{14,1}	R _{14,2}	R ₁₄
15	0	1	1	1	R _{15,1}	R _{15,2}	R ₁₅
16	1	1	1	1	R _{16,1}	R _{16,2}	R ₁₆

interpretation can be given to $[(R_8-R_7)-(R_6-R_5)]/2$, $[(R_{12}-R_{11})-(R_{10}-R_9)]/2$ and $[(R_{16}-R_{15})-(R_{14}-R_{13})]/2$. By adding these four figures and dividing the sum by four, the AB interaction effect can be calculated. There are higher order of interaction effects, three factor interaction effects and four factor interaction effects which can be calculated in a similar way. To facilitate such calculations, a table can be set up (Table 14). (-) sign indicates subtraction and (+) sign indicates addition of the corresponding result. The final figure is divided by 8. Standard error is calculated from

$$\text{standard error} = [\text{variance}]^{1/2} = \left[\frac{4}{N} \sigma^2\right]^{1/2}$$

where N: total number of runs

σ : standard deviation.

If σ is unknown, it can be replaced with s for estimation.

It can be noted that the procedure of calculating each effect includes the whole 16 experiments (actually 32 experiments because each experiment is duplicated) and the number of experiments for the calculation of one effect can be maintained large. Therefore, unless one-factor-at-one-time sequential approach is replicated as many times, factorial design experiment can reduce experimental error enhancing the reliability of data interpretation.

APPENDIX 3
COMPOSITION OF THE IRON USED FOR ELECTRODES

<u>Element</u>	<u>Concentration</u>
C	18 ppm
O	33
Si	50
Al	60
S	40
P	Not detected
Cr	30
Cu	30
Mo	30
Fe	Major

Note: Manufactured by Materials Research Corporation.

BIBLIOGRAPHY

1. W. Stumm and J.J. Morgan, Aquatic Chemistry, 2nd ed., Wiley Interscience, New York, 1981.
2. Handbook of Marine Science, Vol. 1, F.G.W. Walton, Ed., CRC Press, Cleveland, 1974.
3. R.M. Pytkowicz and R. Gates, Science, 161, 690 (1968).
4. C.H. Lu and B.M. Fabuss, Ind. Eng. Chem. Process. Des. Dev., 7, 206 (1968).
5. R.M. Pytkowicz, I.W. Duedall and D.N. Connors, Science, 152, 640 (1966).
6. H. Engell and P. Forchhammer, Corr. Sci., 5, 479 (1965).
7. S.L. Wolfson and W.H. Hartt, Corr., 37, 70 (1981).
8. M.A. Guillen and S. Feliu, Revista de Metallurgia, 2, 519 (1966).
9. H. Klas, Arch. Eisenhuetten, 29, 321 (1958).
10. M.K.V. Nair and B.M. Misra, Desalination, 27, 59 (1978).
11. M.M. Reddy and G.H. Nancollas, J. Colloid Interface Sci., 36, 166 (1971).
12. G.H. Nancollas, T.F. Kazmierczak and E. Schuttringer, Corr., 37, 76 (1981).
13. W.A. House and J.A. Tutton, J. Crystal Growth, 56, 699 (1982).
14. C.W. Davies and A.L. Jones, Trans. Faraday Soc., 51, 812 (1955).
15. G.H. Nancollas, Adv. Colloid Interface Sci., 10, 215 (1979).
16. R.M. Garrels and M. Thompson, Amer. J. Sci., 260, 57 (1962).

17. J.S. Hanor, *Geochim. Cosmochim. Acta*, 33, 894 (1969).
18. R.M. Pytkowicz and J.E. Hawley, *Limnol. Oceanogr.*, 19, 223 (1974).
19. R.M. Pytkowicz, *J. Geol.*, 73, 196 (1965).
20. K.E. Chave and E. Suess, *Limnol. Oceanogr.*, 15, 633 (1970).
21. R.A. Berner, *Geochim. Cosmochim. Acta*, 32, 477 (1968).
22. F.L. LaQue, *Corr.*, 13, May, 33 (1957).
23. R.M. Pytkowicz, *Amer. J. Sci.*, 273, 515 (1973).
24. R.A. Berner, *Geochim. Cosmochim. Acta*, 39, 489 (1975).
25. F. Lippman, *Fortschr. Mineralogie*, 38, 151 (1960).
26. M.M. Reddy and K.K. Wang, *J. Crystal Growth*, 50, 470 (1980).
27. J.L. Bischoff and W.S. Fyfe, *Amer. J. Sci.*, 266, 65 (1968).
28. J.R. Goldsmith, D.L. Graf and O.I. Joensuu, *Geochim. Cosmochim. Acta*, 7, 212 (1955).
29. K.E. Chave, K.S. Deffeyes, P.K. Weyl, R.M. Garrels and M.E. Thompson, *Science*, 137, 33 (1962).
30. L.N. Plummer and F.T. MacKenzie, *Amer. J. Sci.*, 274, 61 (1974).
31. D.C. Thorstenson and L.N. Plummer, *Amer. J. Sci.*, 277, 1203 (1977).
32. G.M. Lafon, *Amer. J. Sci.*, 278, 1455 (1978).
33. H.D. Winland, *J. Sediment. Petrol.*, 39, 1579 (1969).
34. J.W. Morse, A. Mucci and L.M. Walter, *Science*, 205, 904 (1979).
35. K.J. Hsu, *J. Hydrol.*, 1, 288 (1963).
36. J.W. Morse, A. Mucci and F.J. Millero, *Geochim. Cosmochim. Acta*, 44, 85 (1980).
37. R.B. de Boer, *Amer. J. Sci.*, 277, 38 (1977).
38. J.L. Bischoff, *Amer. J. Sci.*, 266, 80 (1968).

39. E. Suess, *Geochim. Cosmochim. Acta*, 34, 157 (1970).
40. K.E. Chave, *Science*, 48, 1723 (1965).
41. M.M. Reddy and G.H. Nancollas, *Desalination*, 12, 61 (1973).
42. G.C. Cox, U.S. Patent 2200469, 1940.
43. G.C. Cox, U.S. Patent 2417064, 1947.
44. E.P. Doremus and G.L. Doremus, *Corr.*, 6, July, 216 (1950).
45. R.A. Humble, *Corr.*, 4, 358 (1948).
46. I.A. Denison and M. Romanoff, *Corr.*, 9, 132 (1953).
47. F.L. La Que, *Corr.*, 6, 161 (1950).
48. H.S. Preiser and B.T. Silverstein, *J. Am. Soc. Naval Eng.*, 62, 881 (1950).
49. H.F. Harvey and O.J. Streever, *Trans. Soc. Naval Archit. Mar. Eng.*, 61, 431 (1953).
50. I.B. Ulanovskii, *Zavodskaiia Laboratoria*, 21, 209 (1955), English translation, Industrial Laboratory.
51. R.P. Kole, An Investigation of the Calcareous Scale Deposited on Steel, Aluminum and Galvanized Iron While Under Cathodic Protection, M.S. Thesis, Univ. of Miami, 1973.
52. C.A. Smith and J.S. Mattson, *Corr. Sci.*, 15, 173 (1975).
53. V.D. Pirogov, Yu.L. Kuz'min and A.P. Zhuk, *Zashchita Metallov*, 9, 311 (1973), English translation, Protection of Metals.
54. W.J. Schwerdtfeger and R.J. Manuelle, *Corr.*, 19, 59 (1963).
55. V.P. Grigorev and S.Ya. Popov, *Zhurnal Prikladnoi Khimi*, 35, 1621 (1962), English translation, Journal of Applied Chemistry of the USSR.
56. M.A.G. Rodrigo, *Afinidad*, 23, May-June, 217 (1966).
57. S. Glasstone, *Introduction to Electrochemistry*, van Nostrand, New York, 1942.

58. W.H. Hartt, C.H. Culberson and S.W. Smith, NACE Convention, Anaheim, California, April 18-22, 1983, Paper no. 59.
59. W.A. Strassberg, Naval Ship Engineering Center, D.C., cited by 58.
60. W.H. Hilbertz, Sea Grant Report No. 04-06-158-4111, U. of Texas, 1976, cited by 58.
61. J.R. Ambrose, A.E. Yaniv and U.R. Lee, Corr., in press.
62. S.C. Dexter and C. Culberson, Corr., 19, September, 16 (1980).
63. R.A. Horne, Advances in Hydrosience, 6, 107 (1970).
64. C.H. Culberson, Corr., in press.
65. D. Hasson, M. Avriel, W. Resnick, T. Rozeman and S. Windreich, Desalination, 5, 107 (1968).
66. M.N. Elliot, Desalination, 6, 87 (1969).
67. A.E. Austin, J.F. Miller, N.A. Richard and J.F. Kircher, Desalination, 16, 331 (1975).
68. A.E. Austin, J.F. Miller, D.A. Vaughan and J.F. Kircher, Desalination, 16, 345 (1975).
69. S. Sarig, F. Kahana and R. Leshem, Desalination, 17, 215 (1975).
70. J. Block and B.M. Watson, Desalination, 19, 359 (1976).
71. P.L. Kapur and B.M. Misra, Desalination, 27, 65 (1978).
72. M.K.V. Nair and B.M. Misra, Desalination, 25, 263 (1978).
73. Y.I. El-Akeel, Desalination, 23, 255 (1977).
74. G. Wilken, Desalination, 33, 201 (1980).
75. W.F. Langlier, D.H. Caldwell, W.B. Lawrence and C.H. Spaulding, Ind. Eng. Chem., 42, 126 (1950).
76. Handbook of Chemistry and Physics, 55th ed., CRC Press, Cleveland, 1974.
77. Water Quality and Treatment, 3rd ed., American Water Works Assoc., Mc-Graw Hill, New York, 1971.

78. Practical Scanning Electron Microscopy, J.I. Goldstein and H. Yakowitz, Eds., Plenum, New York, 1977.
79. G.E.P. Box, W.G. Hunter and J.S. Hunter, Statistics for Experimenters, Wiley, New York, 1978.
80. G.E.P. Box, L.R. Connor, W.R. Cousins, O.L. Davies, F.R. Himsworth and G.P. Sillitto, The Design and Analysis of Industrial Experiments, Oliver and Boyd, London, 1960.
81. Yu.V. Pleskov and V.Yu. Filinovskii, The Rotating Disc Electrode, Consultants Bureau, New York, 1976.
82. A.C. Riddiford, The Rotating Disk System, Advances in Electrochemistry and Electrochemical Engineering, P. Delahay, Ed., Wiley Interscience, New York, 1966.
83. G. Kortum and J.O.'M. Bockris, Textbook of Electrochemistry, Vol. 2, Elsevier, Amsterdam, 1951.
84. Standard Methods, 14th ed., American Public Health Assoc., Washington, D.C., 1976.
85. The Nalco Water Handbook, F.N. Kemmer and J. McCallion, Eds., McGraw-Hill, New York, 1979.
86. J.J. Predalt and J.M. Cases, J. Colloid Interface Sci., 45, 449 (1973).
87. P. Somasundaran and G.E. Agar, J. Colloid Interface Sci., 24, 433 (1967).
88. H.A. Laitinen and W.E. Harris, Chemical Analysis, 2nd ed., McGraw-Hill, New York, 1975.
89. R.A. Day, Jr. and A.L. Underwood, Quantitative Analysis, 4th ed., Prentice-Hall, Englewood Cliffs, 1980.
90. R.B. Fisher, Anal. Chim. Acta, 22, 501 (1960).
91. W.J. Blaedel and V.W. Meloche, Elementary Quantitative Analysis, Row-Peterson, Evanston, 1957.
92. Introduction to Analytical Electron Microscopy, J. Hren, J.I. Goldstein and D.C. Joy, Eds., Plenum, New York, 1979.
93. Handbook of X-ray Photoelectron Spectroscopy, C.D. Wagner, W.M. Riggs, L.E. Davis and J.F. Moulder, Eds., Perkin-Elmer, Eden Prairie, 1979.

94. Methods of Surface Analysis, A.W. Czanderna, Ed., Elsevier, New York, 1975.
95. Lange's Handbook of Chemistry, J.A. Dean, Ed., McGraw-Hill, New York, 1973.
96. B.E. Conway, Electrochemical Data, Elsevier, Amsterdam, 1952.

BIOGRAPHICAL SKETCH

Rupert Utak Lee was born March 1, 1951, at Seoul, Korea. He attended Kyung-gi High School, Korea, and was graduated from Seoul National University, Korea, in 1973, with the degree of Bachelor in metallurgical engineering. From 1973 to 1975, he served in the Korean Army. From 1975 to 1980, he was employed as an engineer by a metal casting and machining company and an oil refining company in Korea.

In January, 1981, he entered the University of Florida and has pursued the degree of Doctor of Philosophy in the Department of Materials Science and Engineering since that date.

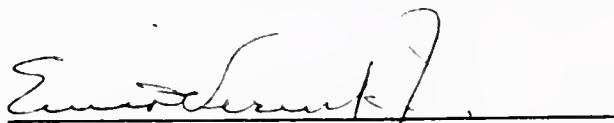
Rupert Utak Lee is a member of Alpha Sigma Mu, Tau Beta Pi, the Electrochemical Society, the National Association of Corrosion Engineers and the Korean Scientists and Engineers Association.

I certify that I have read this study and that in my opinion it conforms to acceptable standards of scholarly presentation and is fully adequate, in scope and quality, as a dissertation for the degree of Doctor of Philosophy.



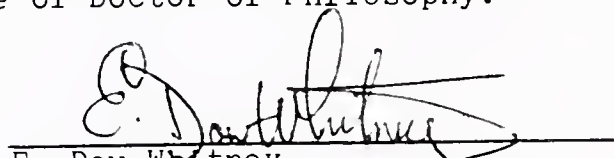
John R. Ambrose, Chairman
Associate Professor of
Materials Science
and Engineering

I certify that I have read this study and that in my opinion it conforms to acceptable standards of scholarly presentation and is fully adequate, in scope and quality, as a dissertation for the degree of Doctor of Philosophy.



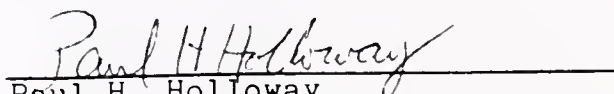
Ellis D. Verink, Jr.
Distinguished Service Professor
of Materials Science and
Engineering

I certify that I have read this study and that in my opinion it conforms to acceptable standards of scholarly presentation and is fully adequate, in scope and quality, as a dissertation for the degree of Doctor of Philosophy.



E. Dow Whitney
Professor of Materials Science
and Engineering

I certify that I have read this study and that in my opinion it conforms to acceptable standards of scholarly presentation and is fully adequate, in scope and quality, as a dissertation for the degree of Doctor of Philosophy.



Paul H. Holloway
Professor of Materials Science
and Engineering

808